Time-Domain Simulation of Sound Propagation in Frequency-Dependent Materials

By

Junjian Zhang

B.S., Shanghai University, 2007

Submitted to the graduate degree program in Department of Aerospace Engineering and the Graduate Faculty of the University of Kansas in partial fulfillment of the requirements for the degree of Doctor of Philosophy.

_____

Chair: Dr. Zhongquan Charlie Zheng

_____

Dr. Saeed Farokhi

_____

Dr. Ray Taghavi

_____

Dr. Z.J. Wang

_____

Dr. Xinmai Yang

Date Defended: December 3, 2018

The dissertation committee for Junjian Zhang certifies that this is the
approved version of the following dissertation:

Time-Domain Simulation of Sound Propagation in Frequency-Dependent Materials

_____

Chairperson: Dr. Zhongquan Charlie Zheng

Date Approved: December 3, 2018

Abstract

This dissertation investigates sound propagation in frequency-dependent materials. The study provides an improved understanding of how to numerically model the porous impedance materials more accurately under the conditions of complicated geometries. The finite difference time-domain (FDTD) method is implemented on the linearized Euler equation (LEE), along with the immersed boundary (IB) method and other numerical techniques to simulate the acoustic wave propagation in air, water, porous media and biological tissues.

When material properties vary in the frequency domain, their time-domain counterpart may contain either convolution operation or fractional derivative operation. Both operations have been studied in this dissertation. Recursive algorithm methods, piece-wise constant recursive methods (PCRC) and piece-wise linear recursive methods (PLRC) are used to numerically solve for convolution operations, and fractional central difference (FCD) methods are used to solve for fractional Laplacians. Both methods show good results in comparison with analytical solutions.

A variety of models have been implemented to simulate the acoustic wave propagation inside porous media. The techniques include: the Zwicker and Kosten (ZK) phenomenological model, the Delany and Bazley model, various porosity two-parameter models, the time-domain boundary condition (TDBC) models, and Wilson's relaxation model (WRX). A new method is also proposed that utilizes the ANSI/ASA-S1.18 measurements to construct a new relaxation function. The new relaxation function can improve the prediction from the TDBC and WRX models significantly.

The ZK and WRX models have also been used in predicting the noise reduction of a house. The noise due to transmission and vibration of the wall is modeled as a simple wave transmission through a porous material layer. A curve fitting method is used to match acoustic

properties of the wall material. By assembling all the materials together, the over-all acoustic response of a house can be simulated.

When acoustic wave propagating in biological tissues, wave propagation equations were previously solved either with convolutions, which consume a large amount of memory, or with pseudo-spectral methods, which cannot handle complicated geometries effectively. The approach described in this study employs FCD method, combined with the IB method for the FDTD simulation. It also works naturally with the IB method which enables a simple Cartesian-type grid mesh to be used to solve problems with complicated geometries.

This work also studies acoustic scattering effects caused by 2D or 3D vortices. The LEE is used to investigate sound wave propagation over subsonic vortices. Instead of traditional direct numerical simulation (DNS) methods, the new approach treats vortex flow field as a scattering background flow and solves the acoustic field with the LEE solver. The numerical method uses a high-order WENO scheme to accommodate the highly convective background flow at high Mach numbers. The study focuses on the acoustic field scaling laws scattered by the 2D and 3D vortices.

Acknowledgments

I would like to acknowledge Dr. Zhongquan Charlie Zheng for his years of patience, guidance and encouragement throughout my study at KU. His guidance gives me a solid foundation to accomplish all the work in this dissertation.

I would also like to thank my committee members Dr. Wang, Dr. Farokhi, Dr. Taghavi and Dr. Yang for their inspiring questions.

I would like to thank my family, my parents and my auntie Lichun Chang for their support. Most importantly, I would like to thank my wife Tina Pei, who has given me companionship, support, confidence through my rough time and, at the same time, given birth to our son Ryan.

Table of Contents

List of Figures

List of Tables

Chapter 1.   Introduction

Sound propagation problem has been a research topic for several decades because of its board applications. The traditional method for studying wave propagation problem is usually in the frequency domain. The research presented here uses a time-domain method to simulate the acoustic propagation phenomenon. When wave propagating inside air saturated porous media or water saturated biological tissues, the acoustic response of the material depends on the material properties. Usually material acoustic properties such as: flow resistivity σ, porosity Ω, and tortuosity q are functions of frequency. Hence, the corresponding model should also be frequency dependent. However, since the frequency-dependent material model is either difficult to implement or inaccurate in the time-domain simulation. Therefore, this topic becomes the goal that author intend to pursue.

1.1 Research Background

The history of acoustic propagation study can be traced back to the eighteenth century starting with the famous wave equation. A very detailed understanding of acoustics has developed from experiments and theories dating back to antiquity. The study of acoustics problems usually includes two proposes: from physical scientific point of view to understand the wave propagation phenomenon; from engineering point of view to control the sound propagation to benefit people's life.

The study of sound propagation over impedance surface can be dated back to the 1940s starting from the electromagnetic wave propagation theory [1]. With the development of the modern science, many approaches have been proposed. There are analytical methods that include the multiple-scattering theory (MST) method [2-4], plane wave expansion (PWE) analysis [5-8], and numerical methods that include the fast field program (FFP) [9-12] parabolic equation (PE)

method [9, 10, 13-15], boundary element methods (BEMs) and finite element methods (FEMs) [16-21].

Finite-difference time-domain (FDTD) methods, as a time-domain technique, can capture the evolution of the acoustic pressure. When wave is propagating over complicate geometries, the FDTD simulation can capture the development of reflection or diffraction waves, which is hard to be obtained by a frequency-domain technique. With the help of high performance computers, FDTD methods have evolved to be a powerful and effective way for simulating sound propagation around complex geometries, different media, and moving objects. By using parallel computation techniques, the time consumption for simulation can also be significantly reduced [22-26].

1.1.1 Porous media modeling

A porous medium is a material containing pores. The skeletal portion of the material is often called "frame". Based on different frame condition, the porous media model can be categorized into two types: rigid frame model and elastic frame model.

The wave propagation in a fluid saturated elastic frame porous material is well described by the Biot theory [27, 28]. The theory describes two classical waves (one "fast" compressional wave and one shear wave), in addition to a second "slow" compressional wave, which is highly dependent on the saturating fluids. Biot's theory addressed the coupling effects between the deformation of fluid saturated porous media and the transient pore fluid flow based on a linear stress-strain relation. The original equations have been reformulated by many others [29-34] which built the foundation of poroelasticity, recently its application can also be found in the

vibro-acoustics [35-38]. However, the research presented in this work will focus on the rigid frame porous medium.

When the frame of the porous material is rigid, there are two ways to model the wave propagation phenomenon happened inside it. The first approach utilized the surface impedance relationship to generate a boundary condition. This method has been widely used in the past. Many frequency domain models have been proposed such as: Delany-Bazley empirical equation [39], Miki model [40], Attenborough's microstructure model and variable porosity model [41, 42]. More recently, Ostashev [43] implemented a time-domain boundary condition (TDBC) which transformed the frequency domain impedance relation into the time domain. The TDBC method allows material properties to vary with frequency which provides a better prediction on the reflection effect and can be easily coupled with the FDTD method. The second approach explicitly models the porous material layer. Usually Zwikker-Kosten (ZK) phenomenological model is used [44-46]. The ZK model assumes porous material properties are constants or weak functions of frequency. Therefore, its prediction for low flow resistivity porous material in high frequency range shows large deviations from other sophisticated models [47]. Wilson's relaxation model (WRX) [48, 49] introduces the relaxation functions which allow the material properties to vary in frequency domain. Hence, the corresponding time-domain relaxation model can model the sound absorption process that happens inside porous material more accurately.

1.1.2 Lossy media modeling

The lossy medium is a medium in which a significant amount of acoustic energy is absorbed per unit distance traveled by sound wave. Most of the biological tissues can be considered as lossy media. Due to the effects caused by heterogeneous tissue media, thermal conduction, viscous dissipation, and chemical relaxation processes, ultrasound propagation processes inside human tissues are more complicated than those in a simple medium, such as air. Sound

attenuation is usually used to quantify energy loss in lossy media, which has also been found following the power law in the frequency domain as [50, 51]:

$$\alpha = \alpha_0 |\omega|^y \tag{1}$$

where α is the sound attenuation with a unit of Np/m, α_0 is absorption coefficient, ω is angular frequency, and y is power law exponent of the specific material with a value between 0 to 2. With this relation, Szabo derived a causal convolution operator that accounted for power law absorption with a non-integer frequency dependence [50]. This operator was later rewritten as a fractional derivative by both Chen and Holm [52] and Liebler and his colleagues [53], and then derived more formally by Kelly et al.[54]. With Szabo's analogy, Chen and Holm [55] and Wismer [56] derived fractional derivative operators based on Stokes' wave equation. While Caputo/Wismer used a fractional time domain operator, Chen and Holm utilized the idea of a fractional Laplacian.

1.1.3 Vortex induced acoustic scattering

Sound scattering caused by vortices has been studied over the past few decades to investigate the sound propagation through atmospheric turbulence [57-59], to understand the acoustic radiation in subsonic jets [60-62], or just to understand the scattering phenomenon in different flow conditions [63-66].

The relative scales of incident acoustic wave length and vortex size (i.e., the vortex core size) influence the scattering effects of vortices. The Born limit is when the acoustic wavelength is much longer than the vortex size. Most of the studies are within the Born limit because it is analytically tractable. Colonius et al. studied single vortex 2D scattering effect by directly solving compressible Navier-Stocks equations numerically. Ford and Smith [66, 67] separated the flow field into inner vortical region and outer wave region by using matched asymptotic

expansions and Lighthill's acoustic analogy approximation, and successfully derived the leading-order scattering amplitude for 2D and 3D vortices. Hattori and Smith [64] studied the scattering effect by Hill's spherical vortex (HSV) and Gaussian vortex rings with direct numerical simulation. The 3D scattering effects agree with their analytical solution very well. Cheinet et al. [68] used finite difference time-domain (FTDT) method simulated 2D scattering effects under larger and small scattering angles. Most of their studies focused on low Mach number and stationary single vortex. Recently, Clair [69, 70] used Linearized Euler equations (LEE) model studied influence of source frequency, velocity, vortex magnitude and their effects on scattering. They put the vortex motion into the simulation, the sound pressure level and its relation with Strouhal number are thus studied, but scaling law for the scattering effect is yet not mentioned.

1.2 Research Object and Motivation

1.2.1 Frequency-dependent porous media modelling

The ZK equation in the time domain is easy to implement with flow resistivity σ, porosity Ω, and tortuosity q, being constants. The model is easy to implement but usually not accurate especially when flow resistivity is low, and frequency is high, which motivated the study of frequency-dependent material model. When we apply the frequency-dependent material model in the time domain, the Fourier transform will introduce convolution operations. The calculation of convolution includes the integration over time, which requires to store the previous solutions in the porous medium at all previous time steps. For a three-dimensional (3D) geometry, a tremendous memory space is thus needed. Consequently, the use of these equations has been limited to one- or two-dimensional geometries (1D/2D). Therefore, an efficient numerical method is necessary to evaluate convolutions with a reduced computational cost.

This problem has been thoroughly studied in electromagnetic propagation as many real materials have frequency-dependent properties. Three main methods emerged; all are based on the approximation of frequency-dependent parameters by a rational function in the frequency domain. The time-domain counterpart corresponds to a sum of exponentially decaying functions which permits a simplified computation of the convolutions [71].

In the first method, a time discretization of the convolution is introduced. Assuming that the variables are constant over one timestep or vary linearly between two consecutive time steps, the evaluation of the convolution can be reduced to that of recursive expressions. Thus, the value of the convolution at the actual time step only depends on the one or two previous time steps. These methods are called recursive convolution methods [72, 73].The second method uses the Z-transform formalism to discretize in time the equations [71, 74]. As shown by Sullivan (1996), the expressions obtained are very close to those of the recursive convolution methods. In the third method, originated from the work of Joseph [75], a differentiation of the convolution is performed, yielding an additional a) set of first-order differential equations, which are solved using the same numerical techniques as employed for the propagation equations. This method is referred to as the auxiliary differential equations (ADE) method and can be seen as a generalized recursive method as no additional approximations on the time variations of the variables are introduced.

To implement WRX model [47] and Ostashev's TDBC model [43], we would like to address this issue by using the recursive algorithm which can solve the convolution operation numerically with only one or two steps of the previous solution [72, 73].

1.2.2 Frequency-dependent lossy media modelling

To simulate sound propagation inside lossy media, different numerical approaches have been proposed over the past few decades. Classical thermo-viscous theory predicted that the acoustic sound would attenuate inside lossy media due to thermal conduction effects and viscous dissipation [76]. However, the theory can only predict square-law attenuation ($y = 2$). Sparrow and Raspet implemented the finite-difference time-domain method (FDTD) in the 2D axisymmetric domain with nonlinear effects where the power attenuation law was not considered [77]. Szabo proposed a time-domain causal convolution operator that account for both power law absorption and dispersion($1 < y < 2$) [50]. However, the implementation of convolution integration consumes extremely large memory [78], especially when the computational domain is large. To improve the model, a fractional Laplacian model replaced the convolution model [52].

Treeby and Cox implemented Chen and Holm's model with the pseudo-spectral method [79], but theirs "k-space" method still needs to transform spatial derivatives back to the frequency domain which makes it difficult to deal with complicated geometries. Our approach here uses the fractional central difference (FCD) method and the FDTD method along with the immersed boundary (IB) method which can directly solve the model in the time domain along with the complicated geometry.

1.2.3 Vortex scattering effect study

From the low frequency theory, the scattering magnitude should scale with $r^{-\frac{1}{2}}$ [60] in 2D vortices, where r is the distance away from the vortex center, which it is only true for a compact vortex, e.g. zero-circulation vortex or vortex pair in 2D. When circulation is non-zero due to the slowly decaying mean flow field, the long-range refractive effect will affect the result [63, 65]. A

vortex pair composed of two opposite orientation of finite-circulation vortices, as another form of zero-circulation vortex, is then of interest to study. The refractive effect of a 3D vortex is similar to a 2D compact vortex, and therefore the scattering effect of a 3D vortex would be similar to that of a compact 2D vortex.

The method for studying scattering effect via direct numerical simulation (DNS) solves vortex induced flow field together with the acoustic field caused by that. Therefore, it is very expensive and not practical in studies with 3D big domains or complex geometries. In this study, we use the linearized acoustic propagation equation to study acoustic scattering. We use the analytical solutions for the background vortex flow for both 2D and 3D vortices. In this sense, the DNS result is a fully coupled flow and acoustic solution, and the linearized simulation result in this study is a one-way acoustic solution where the flow influences acoustic propagation, but not vice versa. We show, in this study, the one-way acoustic simulation compares very well with the full DNS results by Colonius et al (1994), demonstrating that the linearized simulation is a valid tool at least for studying vortex scattering effects.

If we treat the background vortex flow as the source of acoustic scattering, by following the concept of the Lighthill analogy, we can have:

$$\frac{1}{c_0^2}\frac{\partial^2 p}{\partial t^2} - \nabla^2 p = \frac{\nabla^2 T_{ij}}{\partial x_i \partial x_j} \tag{2}$$

where $T_{ij} = \rho_{av}\left(u_i^{av}u_j + u_i u_j^{av}\right)$ is the Lighthill stress tensor that behaves as the acoustic source in the acoustic propagation equation, p is the acoustic pressure, c_0 is the speed of sound, ρ_{av} is the background atmosphere density, and u_i^{av} and u_i are respectively background flow velocity and acoustic velocity. Therefore, the refraction effect of the background vortex flow can be considered as the source of acoustic scattering. The solution of Eq. (2) can be written as

$$p = \int G(x - \xi, t - \tau)T_{ij}(\xi, \tau)d^m\xi d\tau \tag{3}$$

where G is the 2D or 3D Green function and $m = 2$ or 3, if the problem considered is 2D or 3D, respectively. When the vortex flow is treated as the source in the Lighthill stress tensor, the velocity decay rate of the vortex versus the distance from the vortex center influences the distance scaling law of acoustic scattering. The Lighthill tensor in the vortex background flow follows the vortex velocity decay rate with $T_{ij} \sim 1/|\xi|^n$, where, e.g., $n = 1$ for a vortex with finite circulation, $n = 2$ for a vortex dipole, and $n = 3$ for a 3D Hill's vortex. If the source is compact, i.e., the source strength decays fast with the distance, the scaling law of acoustic scattering follows that of the Green function. The 2D acoustic pressure scattering scales with $1/r^{\frac{1}{2}}$, and the 3D scales with $1/r$. In this study, we investigate the distance scaling laws of a single vortex with a finite circulation, a single vortex with exponentially decaying circulation, a stationary or moving vortex dipole, and a stationary 3D Hill's vortex.

We consider the cases in which the wavelength of incident sound is a few times longer than the characteristic length scale of the vortex to align with the Born approximation. In this paper, a plane incident wave at a frequency of 85Hz is used to study the scattering effects through vortices.

For high-speed vortex flow, the velocity and its gradients are large, and numerical simulation without employing special numerical treatment for the convection terms can often suffer from numerical errors in the regions around the high-speed vortices. We address the problem by using a high order WENO scheme [80-89] to solve the convection-dominant background flow in the time-domain numerical simulation. This scheme not only achieves higher-order accuracy near the high gradient velocity regions, but also maintains a stable and non-oscillatory solution. On the other hand, to save the computational effort for the high-order scheme, the WENO scheme

does not need to be applied to the entire computational domain, but only to the regions with high velocity.

1.3 Dissertation Outline

This dissertation concentrates on the numerical modeling the acoustic wave propagation phenomena in frequency-dependent materials, improving the numerical model performance and apply the model to explain some physical phenomenon. Different models will be applied and reviewed. The numerical results are verified by the existing analytical solutions or measurement results.

Chapter two will compare time-domain ZK model simulation with ANSI (American National Standard Institution) model results. Chapter three will review the popular time-domain porous material models and discuss a new method of constructing relaxation function, which can improve the prediction of the original frequency-dependent material model. A fitting method will be presented in Chapter four to determine the material parameters of each component of a house. Then the corresponding parameters are applied to the model of a house near an airport. Chapter five investigates the ultrasound propagation in biological tissues. Chapter six studies the scattering law caused by wave propagation over 2D and 3D vortices. In the last chapter, a summarize is presented for the main conclusions and new contributions of this dissertation work.

Chapter 2.   A Time-Domain Simulation for Comparison with the ANSI Impedance Measurement

2.1 Introduction

In this chapter, we will study two problems: firstly, we would like to compare the prediction of time-domain ZK model simulation with the results from ANSI (American National Standard Institute) one- and two-parameter model. Second, we would like study the influence bought by ground roughness and each model's performance in roughness ground condition.

2.2 Numerical method

2.2.1 ANSI model

The ANSI standard [90], developed by Acoustical Society of America, contains procedures for obtaining the real and imaginary parts of normalized acoustic impedance of ground surfaces from measurements of the sound pressure levels at two separated microphones using specified geometries. ANSI provides two measurement setups, Geometry A and Geometry B. The design is given in Figure 1 with the parameters listed in Table 1.
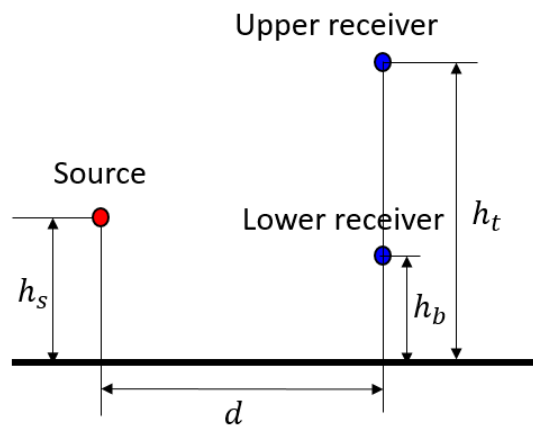
Figure 1. Geometrical definition: h_s=source height, h_t= top microphone height, h_b= bottom microphone height, d=source/receiver horizontal separation

Table 1 Parameters in ANSI's recommended geometry set up

	Geometry A	Geometry B
Source height (h_s)	0.325 m	0.20 m
Upper microphone height (h_t)	0.46 m	0.20 m
Lower microphone height (h_b)	0.23 m	0.05m
Horizontal separation (d)	1.75 m	1.0 m

Two frequency domain impedance models are provided in the ANSI's standard, one-parameter model and two-parameter model. The one-parameter model is the Delany and Bazley model [39], which is expressed as:

$$\frac{Z_s}{\rho_0 c_0} = 1 + 9.08 \left(\frac{1000f}{\sigma_0}\right)^{-0.75} + i\, 11.9 \left(\frac{1000f}{\sigma_0}\right)^{-0.73} \tag{4}$$

where σ_0 is the flow resistivity of the ground material, Z_c is the ground surface impedance, f is the frequency, ρ_0 is the density of the air, and c_0 is the speed of sound in air. The two-parameter model is also called variable porosity model [42], which is expressed as

$$Z = \frac{1+i}{\sqrt{\pi\gamma\rho_0}}\sqrt{\frac{\sigma_e}{f}} + i\,\frac{c_0\alpha_e}{4\pi\gamma f} \tag{5}$$

where $\sigma_e = \frac{\sigma_0}{q}$ is the effective flow resistivity [91], α_e represents an effective rate of change of porosity with depth, and q is the tortuosity of the porous media.

2.2.2 Linearized Euler Equation

The linearized Euler equation for acoustic propagation in the air and porous ground are:

$$\frac{\partial \boldsymbol{u}}{\partial t} + (\boldsymbol{u_{av}} \cdot \nabla)\boldsymbol{u} + (\boldsymbol{u} \cdot \nabla)\boldsymbol{u_{av}} = -\alpha_{av}\nabla p - \alpha\nabla p_{av} + f_u \tag{6}$$

$$\frac{\partial p}{\partial t} + (\boldsymbol{u_{av}} \cdot \nabla)p + (\boldsymbol{u} \cdot \nabla)p_{av} = -\gamma p \nabla \cdot \boldsymbol{u_{av}} - \gamma p_{av}(\nabla \cdot \boldsymbol{u}) + f_p \tag{7}$$

where f_u and f_p are fictitious body forces to enforce the velocity and pressure to accommodate

the governing equations in air and inside a porous medium, which are given by [2]:

$$f_u = \begin{cases} 0, & \textit{Outside the porous medium} \\ \alpha_{av}\nabla p + \alpha\nabla p_{av} + (\boldsymbol{u}_{av} \cdot \nabla)\boldsymbol{u} + (\boldsymbol{u} \cdot \nabla)\boldsymbol{u}_{av} - \dfrac{\Omega}{q^2}\alpha_{av}(\nabla p + \sigma_0\boldsymbol{u}), & \textit{Inside the porous medium} \end{cases} \quad (8)$$

$$f_p = \begin{cases} 0, & \textit{Outside the porous medium} \\ \gamma p\nabla \cdot \boldsymbol{u}_{av} + \gamma p_{av}(\nabla \cdot \boldsymbol{u}) + (\boldsymbol{u}_{av} \cdot \nabla)p + (\boldsymbol{u} \cdot \nabla)p_{av} - \dfrac{\gamma p_{av}}{\Omega}(\nabla \cdot \boldsymbol{u}), & \textit{Inside the porous medium} \end{cases} \quad (9)$$

where $\boldsymbol{u}_{av}$, p_{av} and α_{av} are the time averaged velocity, pressure, and specific volume,

respectively; $\boldsymbol{u}$, p and α are the corresponding acoustic fluctuations, with α given as:

$$\alpha = -\frac{p}{\gamma p_{av}\rho_{av}} \quad (10)$$

where γ is the specific-heat ratio. The coefficients, Ω, q, and σ_0 in Eqs. (8) and (9), are porous

medium porosity, tortuosity, and flow resistivity, respectively. A second-order finite difference

numerical scheme both in time and space [25] is applied for the simulations in this study.

For the cases in this paper, we use the values $p_{av} = 100kPa$, $\gamma = 1.4$, the density of

air $\rho_{av} = 1.225\ kg/m^{-3}$, the porosity $\Omega = 0.3$, and the tortuosity $q = \sqrt{3}$. The flow

resistivity σ_0 varies for the porous ground depending on the impedance.

2.3 Numerical simulation and results discussion

We will conduct two studies here. The first study is in flat smooth ground condition as

specified in the ANSI's standard. The second setup will introduce the ground roughness

condition to investigate the difference.

2.3.1 Smooth ground study

Figure 2 shows "Geometry A" setup of ANSI's standard [90]. The computational domain is

2.5 meters in both y-direction and z-direction. A uniform grid mesh is used in the simulation,

with the grid size set to be $dy = dz = 0.002m$, which ensures that there are at least 20 grid

points within one shortest wavelength for the interested frequency(4000Hz). The Courant–

Friedrichs–Lewy (CFL) number is set to be 0.3 to guarantee a stable and efficient simulation. The simulation time is 8 ms, which allows the wave-front and reflection wave can fully pass all the receivers. 0.2 m perfectly matched layer (PML) [92] is placed on the top and right boundary to prevent the reflections from the computation boundary. 0.5 m porous medium layer is placed at the bottom of the boundary.
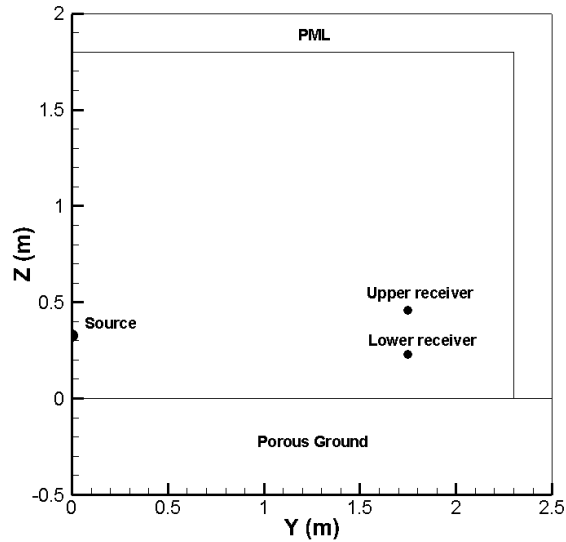
Figure 2. Simulation setup for ANSI Geometry A

A broadband point source in the form of Gaussian distribution is used as:

$$p = \exp(-300r^2) \tag{11}$$

where r is the distance between the sound source and any location in the domain. The source and receivers' location are specified according to ANSI's standard. The study of "Geometry B" uses the same computational domain. The details of each source and receiver setup can also be found in Table 1.

The level difference (LD) is the difference between the upper and lower receiver's sound pressure level (SPL), which is defined as:

$$LD(f) = SPL_{upper} - SPL_{lower} = 20\log_{10}\frac{psd_{upper}}{psd_{lower}} \tag{12}$$

where psd is the power spectrum density (PSD), which can be obtained by Fourier transform

acoustic pressure time history collected at each receiver location. The level differences

calculated at each one-third octave band center frequency between 250 and 4000Hz are given in

Figure 3 and Figure 4. It should be noticed, the Two-parameter model's effective flow resistivity

is calculated based on the relation of $\sigma_e = \frac{\sigma_0}{q}$, we also let $\alpha_e = 0$ for an infinite depth of ground.

The corresponding curves are generated according to the method provided in ANSI's Annex C

[90].

It can be found that the ZK model's results only matches with ANSI's prediction at low

frequency when flow resistivity is low in Figure 3 (a) and Figure 4 (a). By increasing the flow

resistivity, the frequency region that matches also increases as presented in Figure 3 (b) and

Figure 4 (b). When flow resistivity is very high, three curves match very well.

$$\frac{\partial \boldsymbol{u}}{\partial t} = -\frac{\Omega}{q^2} \alpha_{av} \left(\nabla p + \sigma_0 \boldsymbol{u}\right) \tag{13}$$

$$\frac{\partial p}{\partial t} = -\frac{\gamma p_{av}}{\Omega} \left(\nabla \cdot \boldsymbol{u}\right) \tag{14}$$

Let's take a close look at ZK equation in Eqs. (13) and (14). The velocity equation Eq.

(13) says if the flow resistivity σ_0 is low, the prediction of acoustic velocity and pressure also

depends on porosity Ω and tortuosity q. We are testing different flow resistivity conditions with

same Ω and q. Different flow resistivities implies different porous materials, which means the

porosity Ω and tortuosity q values should also be different in each simulation. Therefore, if we

keep the values same across all simulations, the result of course will deviate from the data

provide by ANSI model, especially when flow resistivity is low. On the other hand, when flow

resistivity is very high, the unsteady term on the left-hand side (LHS) of the equation comparing

with the term $\sigma_0 \boldsymbol{u}$, is a very small term. So, we can set LHS of Eq. (13) to 0. Therefore, we can

drop the constant term $\frac{\Omega}{q^2}\alpha_{av}$ on the right-hand side of Eq. (13), which leads to $\nabla p = -\sigma_0 u$. The

pressure velocity relation tells us at this moment, only flow resistivity will influence the results

regardless porosity and tortuosity. That explains when σ reaches $1\ MPa \cdot s \cdot m^{-2}$ or beyond, the

ZK model's results agree with the other two models' prediction pretty good in Figure 3 (d) and

Figure 4 (d). Therefore, to make a reasonable comparison we will focus on the high flow

resistivity material hereafter.

(a)

(b)

(c)

(d)
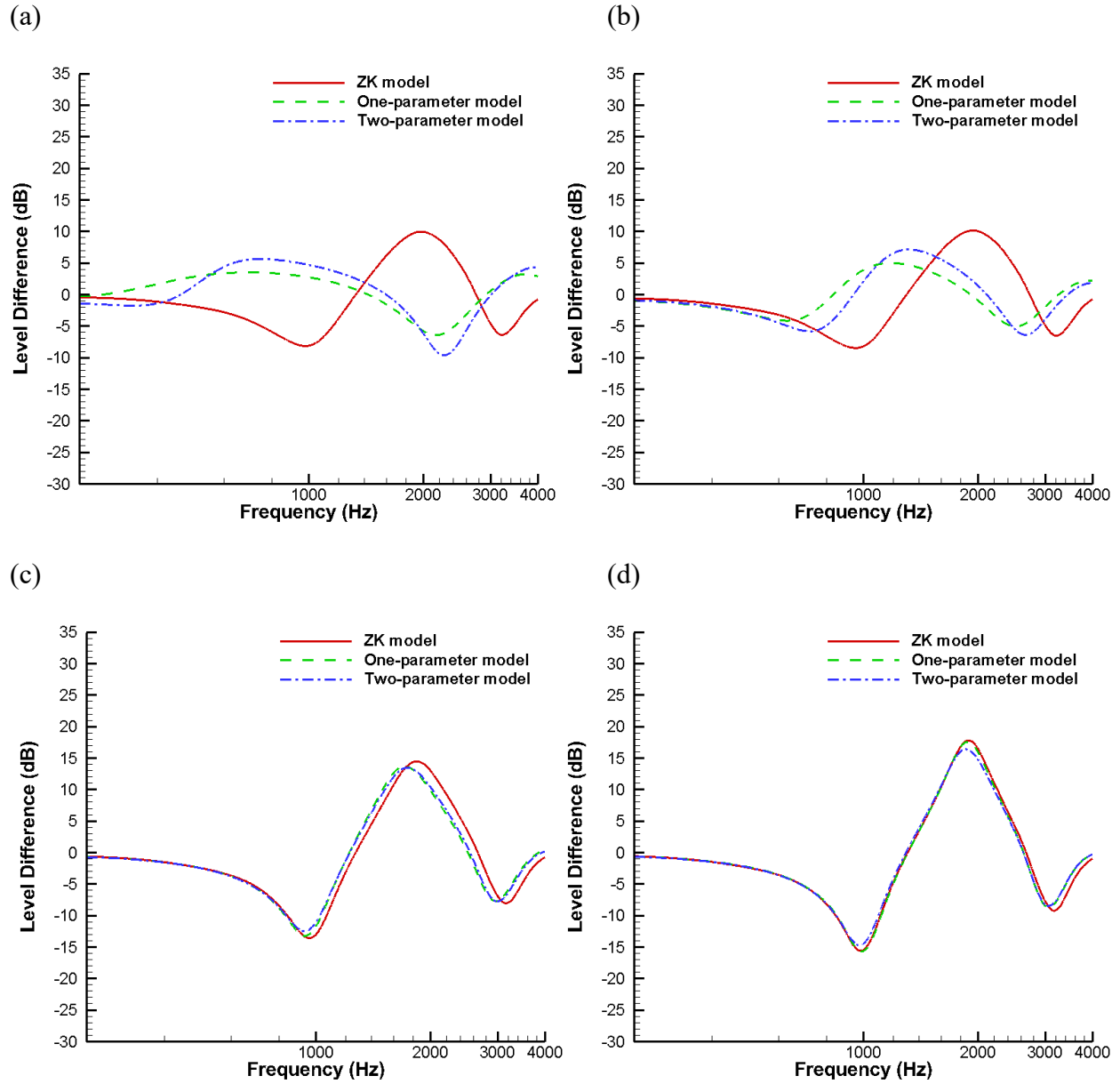
Figure 3. Comparison of the level difference between ZK model with One and Two-parameter model for ANSI Geometry A in different flow resistivity condition, a) $\sigma = 10000\ Pa \cdot s \cdot m^{-2}$; b) $\sigma = 100000\ Pa \cdot s \cdot m^{-2}$; c) $\sigma = 1000000\ Pa \cdot s \cdot m^{-2}$; d) $\sigma = 3200000\ Pa \cdot s \cdot m^{-2}$
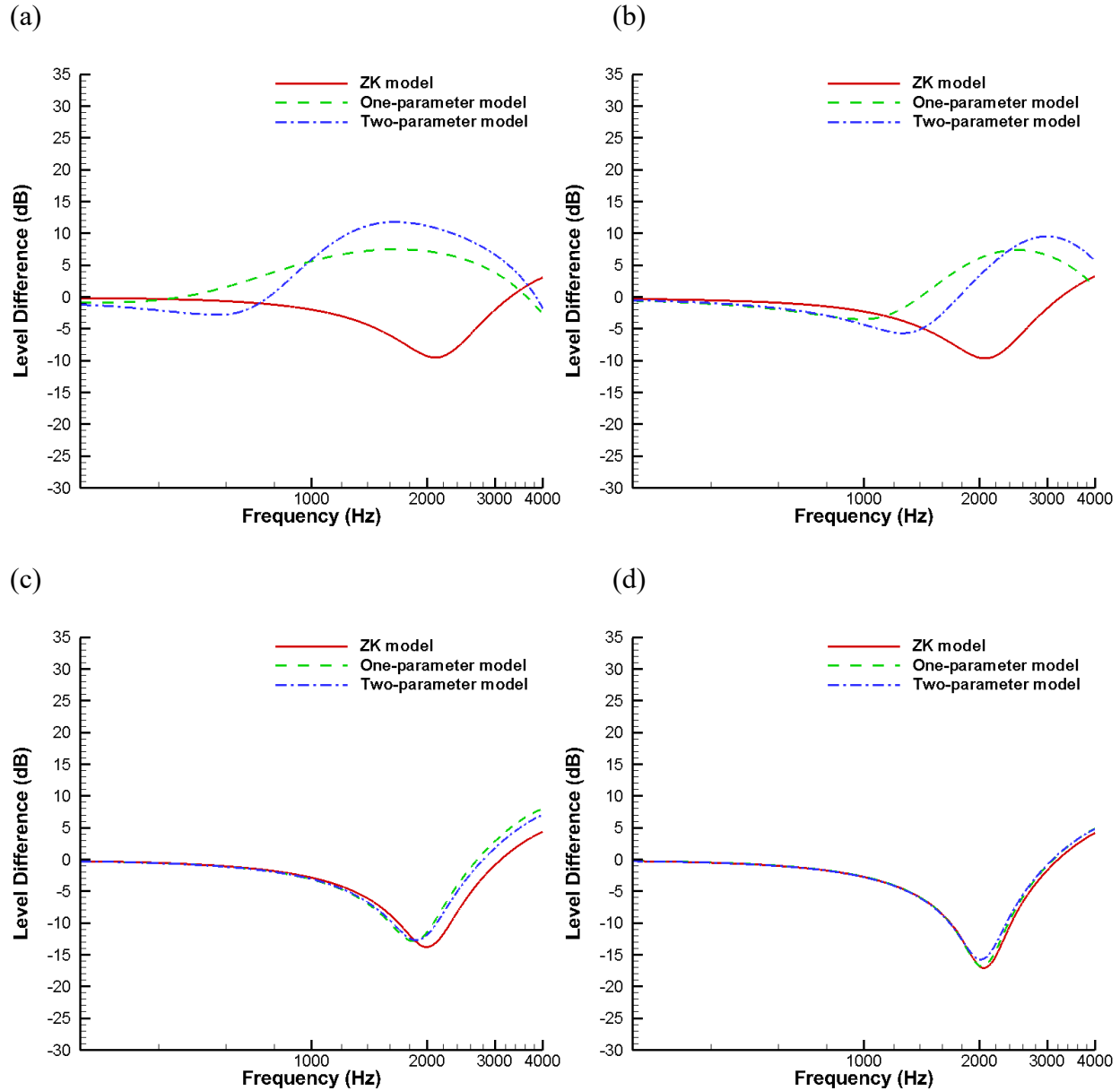
Figure 4. Comparison of the level difference between ZK model with One and Two-parameter model for ANSI Geometry B in different flow resistivity condition, a) $\sigma = 10000 \; Pa \cdot s \cdot m^{-2}$; b) $\sigma = 100000 \; Pa \cdot s \cdot m^{-2}$; c) $\sigma = 1000000 \; Pa \cdot s \cdot m^{-2}$; d) $\sigma = 3200000 \; Pa \cdot s \cdot m^{-2}$

2.3.2 Roughness ground study

Recently an interesting study conducted by Bashir and his colleague shows the ground roughness plays important role in sound propagation near ground [93]. Therefore, we would like to verify our simulation with theirs measurement results before we implement the roughness ground to the ANSI's setup.

Figure 5 gives the simulation set up, the simulation domain is 4 meters in the y-direction and 2 meters in the z-direction. PML thickness is 0.5 meters in left, top and right boundary to absorb the reflection waves. 15 Triangles are equally placed on the ground from y=0.555m to 1.145m with a center-to-center space of 0.04m. The width of each triangle is 0.03m and height is 0.015m. Grid size dy, dz is set to be $0.001m$, which will ensure each triangle has enough resolution. Meanwhile, this setup can also resolve an 8000Hz signal with 21grids. To capture high frequency signal, a gaussian plus in the form of Eq. (15) is used. This source is placed at (0.5, 0.07), a receiver is placed at (1.2, 0.07). We set simulation time to be 15ms, which allows wave front and ground reflection wave be able to propagate all the way to the right.

$$p = \exp(-1000r^2) \tag{15}$$

The triangles on the ground are modeled with porous medium with flow resistivity $\sigma_0 = 3.2 \, MPa \cdot s \cdot m^{-2}$. Two additional simulations are also conducted with the similar set up, one with 9 triangles (0.08m center-to-center space) and the other with smooth rigid ground.
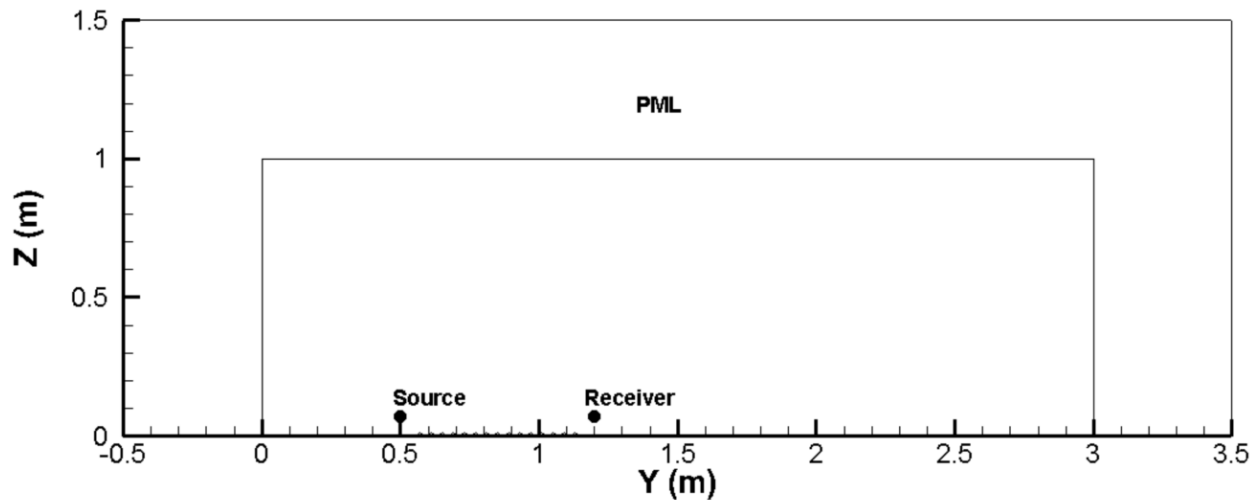
Figure 5. Roughness ground simulation set up

Contours at simulation time $t = 2.5ms$ are provided in Figure 6. Diffraction caused by the triangles can be clearly observed. When center-to-center space is set to be 0.08m in Figure 6 (b) the diffraction is much clear. The larger space will let diffraction wave generated by previous triangle have longer time to develop without being interrupted, which cause the Figure 6 (b) looks much busy than Figure 6 (a). On the other hand, if two triangles are very close, the diffraction wave may not have enough time to develop, and many local cancelations are likely to happen very soon, which lead to Figure 6 (a) looks more close to the smooth ground contours given in Figure 6 (c).

(a)

(b)

(c)
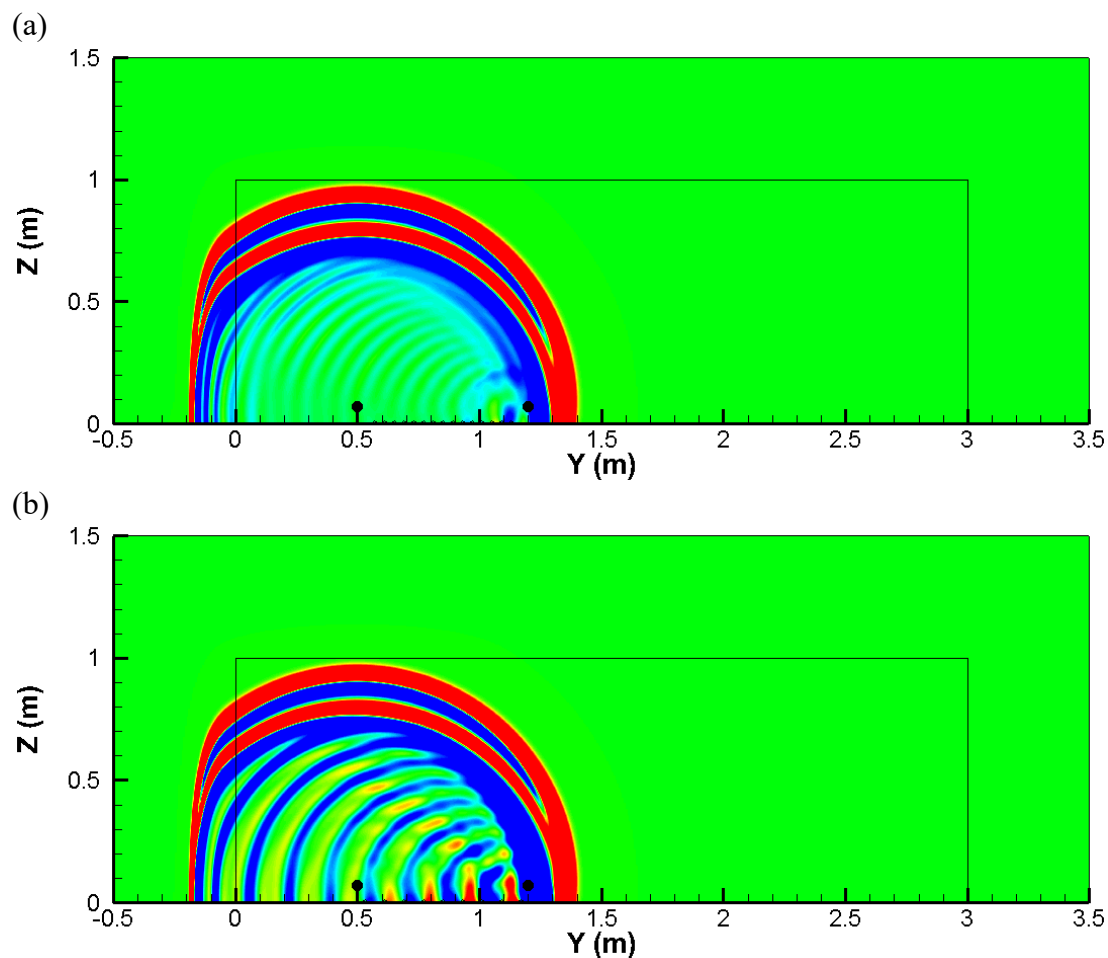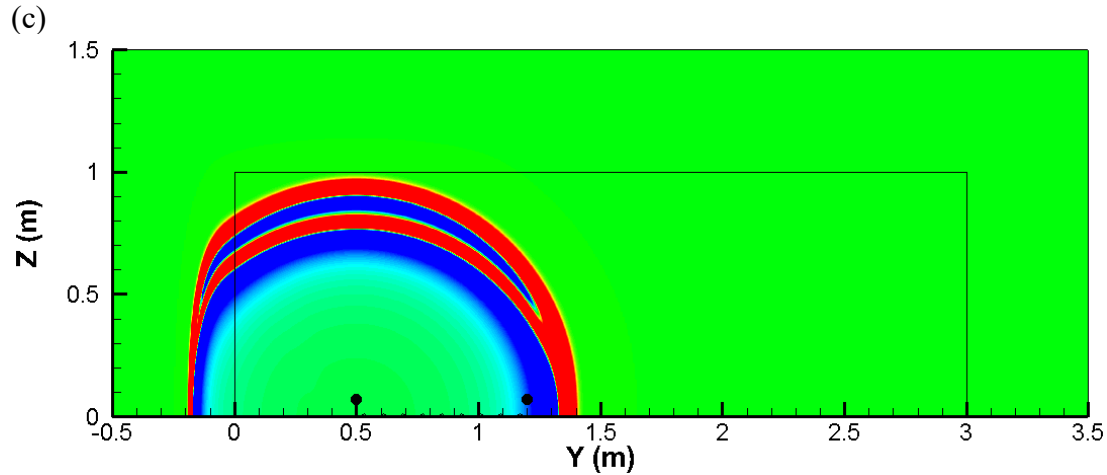
Figure 6. Pressure contours at simulation time t = 2.5ms with (a) center-to-center distance 0.04m, (b) center-to-center distance 0.08m; (c) smooth ground

Figure 7 compares relative sound pressure level between numerical simulation with measurements from Bashir et al.[93]. The relative sound pressure level is calculated with:

$$Rel.\,SPL = 20\log(psd_{ground}/psd_{free\,space}) \tag{16}$$

where psd_{ground} is the PSD from each roughness ground simulation, and $psd_{free\,space}$ is obtained from a free space simulation (no ground). Both roughness ground configurations simulation results agree with measurements data. The simulation validated our immersed boundary method.

On the other hand, it should be noticed that ANSI's measurements are normally done under smooth ground condition. However, the solid curve in Figure 7 shows the smooth ground performance would be very different from that of a roughness ground condition.
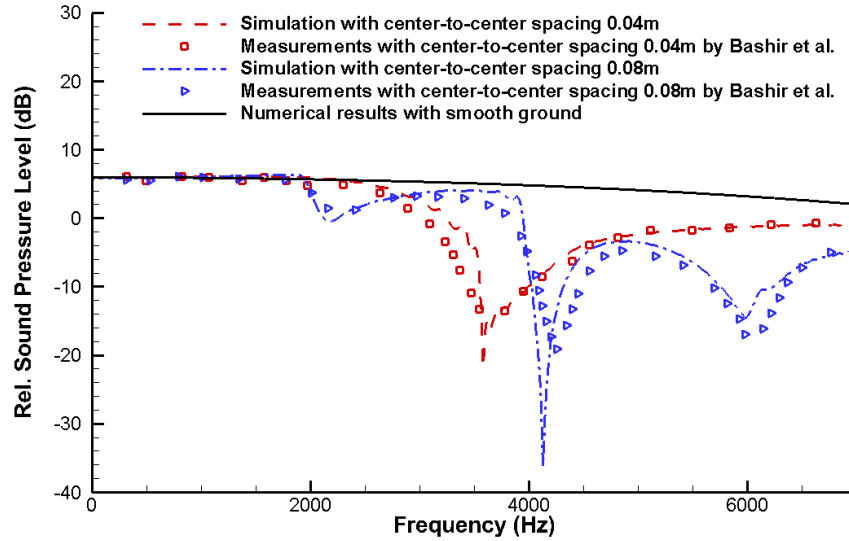
Figure 7. Relative sound pressure level comparison between simulations with measurement data from Bashir, et.al

Since implementation of immersed boundary method is verified, we are ready to bring these roughness ground features to our original ANSI's simulation. Both roughness ground configurations are tested with triangles equally placed from 0 to 2.3m. Porous ground flow resistivity are set to be $3.2 MPa \cdot s \cdot m^{-2}$ to remove the influence from porosity and tortuosity.

Figure 8 compares the level difference between roughness ground simulation results and ANSI models' prediction. It should be noticed that if roughness height is less than half of the shorted wavelength interested, according to ANSI, one and two-parameter model's prediction should still be valid. In our case, the highest frequency we interested is 4000Hz, which implies the height variation should be less than 5cm. However, even the triangle height we used is 1.5cm, which is much lower than the requirement, level difference curves in Figure 8 indicated the roughness ground prediction should be different from smooth ground. The peak frequency is found to shift towards low frequency region. When roughness spacing is bigger more oscillations can be observed at high frequency range.
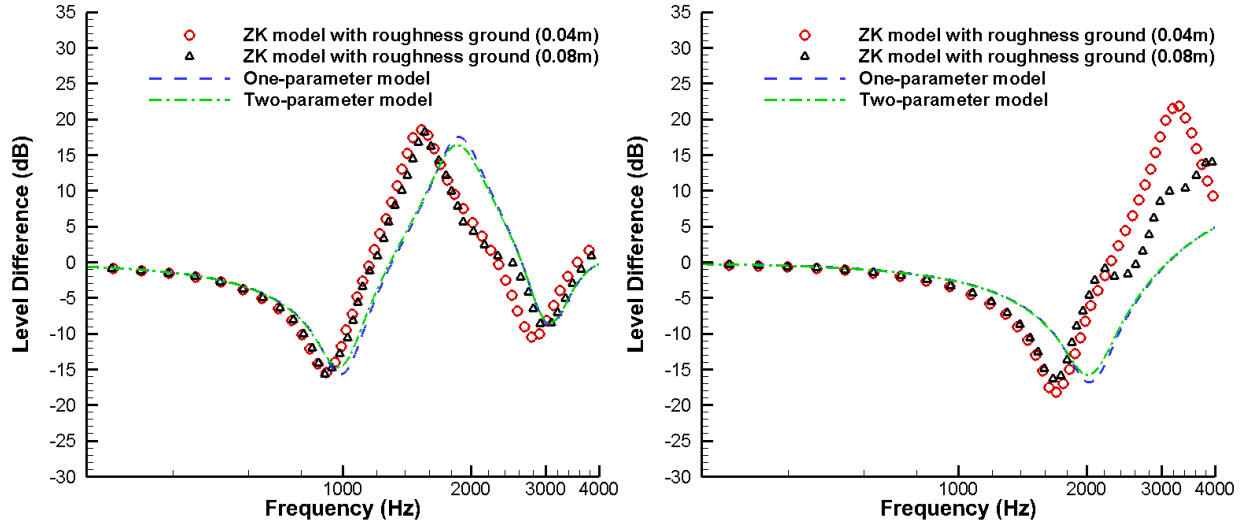
Figure 8. Comparison of the level difference between ZK model prediction in roughness ground with One and Two-parameter model for ANSI (a) Geometry A, (b) Geometry B.

2.4 Summary

Time domain simulations with immersed boundary method are used to predict the acoustic response from porous medium ground. ZK model shows very good agreement with ANSI's measurement data especially under the condition of high flow resistivity. The numerical method is also validated by good agreement with roughness ground measurement data provided by Bashir et al.[93]. Once roughness condition is brought to the original ANSI setup, mismatches can be found even ground height variations are still within the allowance of the ANSI's requirement, which indicate the necessarily of the numerical simulation.

Chapter 3.   Sound propagation simulation inside frequency-dependent porous material

3.1 Introduction

As we mentioned the inaccuracy in the low flow resistivity prediction in previous

chapter, so we will explore the solution in this chapter. We will start with reviewing the existing

popular time-domain porous media models and implement two frequency-dependent models.

After comparing our implementation of the frequency-dependent model with the analytical

solutions and the measurement results, we will propose a method based on ANSI/ASA-S.1.18

measurements and ANSI's two-parameter model. The method will construct a new relaxation

function based on physical measurement results, which can improve the existing model's

prediction significantly.

3.2 Outdoor acoustic propagation equations

3.2.1 Linearized Euler equations

Considering porous material is saturated with air, sound propagation in air can be

simulated by solving Euler equations, linearized around mean flow field with velocity u_0,

density ρ_0 and pressure P_0, the acoustic pressure p, and acoustic velocity u are obtained by

solving the resulting system in ideal gas as:

$$\frac{\partial p}{\partial t} + (u_0 \cdot \nabla)p + (u \cdot \nabla)P_0 = -\gamma p \nabla \cdot u_0 - \gamma P_0 (\nabla \cdot u) + f_p \tag{17}$$

$$\frac{\partial u}{\partial t} + (u_0 \cdot \nabla)u + (u \cdot \nabla)u_0 = -\frac{1}{\rho_0}\nabla p - \frac{1}{\rho}\nabla P_0 + f_u \tag{18}$$

where γ is specific gas constant of air, f_p and f_u are the possible fictitious body force terms used

in the immersed boundary method [88]. The equation system is solved with a second order finite

difference scheme in both time and space [25].

3.2.2   ANSI's two-parameter model

The American National Standard ANSI/ASA S1.18 [90] is a standard that determines the

ground surface acoustic impedance with physical sound pressure level measurement. Two

impedance models are adopted in the standard, one-parameter model and two-parameter model.

We will focus on the two-parameter model since the model is used in processing the

measurement data. The two-parameter model is also called Attenborough's variable porosity

model [42], which takes the form of:

$$\frac{Z}{\rho_0 c_0} = \frac{1}{\sqrt{\pi \gamma \rho_0}} \sqrt{\frac{\sigma_0}{f}} + i \left(\frac{1}{\sqrt{\pi \gamma \rho_0}} \sqrt{\frac{\sigma_0}{f}} + \frac{c_0 \alpha_e}{4 \pi \gamma f} \right) \tag{19}$$

where α_e is the effective rate of change of porosity, σ_0 is the flow resistivity, γ is the specific

heat ration of air, f is the frequency, c_0 is the speed of sound in air.

3.2.3   ZK model

The Zwikker-Kosten phenomenological model (ZK model) describes the wave

propagation phenomenon inside a porous media layer. It can be expressed as:

$$\sigma_0 u + \frac{\rho_0 q^2}{\Omega} \frac{\partial u}{\partial t} = -\nabla p \tag{20}$$

$$\frac{1}{K} \frac{\partial p}{\partial t} = -\nabla \cdot u \tag{21}$$

The model assumes a rigid porous frame. Therefore, ZK model works well for the air-saturated

condition. Zwikker and Kosten call Ω the material porosity, q tortuosity, K the compression

modulus. They indicate that those material parameters may be frequency dependent. However, in

the following text, we still consider those material parameters constants in order to build a

baseline for comparison.

3.2.4 Relaxation model

As mentioned in the previous section, material properties may not always present constant values in the frequency domain. The relaxation model proposed by Wilson (WRX) [48, 49] uses viscous and thermal diffusion to model the relaxation process that happened inside material pores. He calls τ_v vorticity relaxation time, τ_e entropy relaxation time. And he formed two relaxation functions by connecting high and low frequency limits of material properties with smooth functions $S(\omega\tau)$. As a result, the original ZK model can be modified as:

$$\sigma_0 u + \frac{\rho_0 q^2}{\Omega}\left\{\frac{\partial u}{\partial t} + \mathcal{F}^{-1}[S(\omega\tau_v)] * \frac{\partial u}{\partial t}\right\} = -\nabla p \tag{22}$$

$$\frac{\Omega}{\gamma P_0}\left\{\frac{\partial p}{\partial t} + (\gamma - 1)\mathcal{F}^{-1}[S(\omega\tau_e)] * \frac{\partial p}{\partial t}\right\} = -\nabla \cdot u \tag{23}$$

Here $\tau_v = \frac{2\rho q^2}{\sigma_0 \Omega}, \tau_e = N_{pr} s_B^2 \tau_v$, where N_{pr} is the Prandtl number and s_B is a pore shape factor. Comparing Eq. (22), (23) with Eq. (20) and Eq. (21), we can find the WRX model and the ZK model are very similar in shape except the WRX model carries additional convolution terms in the brackets. The introduced frequency-domain relaxation functions in the Eq. (22) and (23) take the form of:

$$S(\omega\tau) = \frac{1}{\sqrt{1 - i\omega\tau}} \tag{24}$$

The corresponding time-domain relaxation function is:

$$s(t) = \mathcal{F}^{-1}(S(\omega\tau)) = \frac{1}{\sqrt{\pi\tau t}}\exp\left(-\frac{t}{\tau}\right)H(t) \tag{25}$$

where $H(t)$ is the Heaviside function.

The WRX model can also be derived into a different format as [47]:

$$\frac{\partial u}{\partial t} = -\frac{\Omega}{\rho_0 q^2}\nabla p + \frac{\Omega}{2\rho_0 q^2}\left[\bar{s}\left(\frac{t}{\tau_v}, 1\right) * \nabla p\right] - \frac{1}{\tau_v}u \tag{26}$$

$$\frac{\partial p}{\partial t} = -\frac{\gamma P_0}{\Omega} \nabla \cdot u + \frac{(\gamma - 1)P_0}{\Omega} \left[\bar{s}\left(\frac{t}{\tau_e}, \gamma - 1\right) * (\nabla \cdot u) \right] \tag{27}$$

which is the so-called stats-equation (WRX-S). The relaxation functions used here are in

different forms. The corresponding relaxation functions in frequency and time domain are:

$$\bar{S}(\omega\tau, a) = \frac{1 + a}{\sqrt{1 - i\omega\tau} + a} \tag{28}$$

$$\bar{s}\left(\frac{t}{\tau}, a\right) = \mathcal{F}^{-1}(S(\omega\tau)) = (1 + a)e^{-\frac{t}{\tau}} \left[\frac{1}{\sqrt{\pi t \tau}} - \frac{a}{\tau} e^{\frac{a^2 t}{\tau}} \mathrm{erfc}\left(a\sqrt{\frac{t}{\tau}}\right) \right] \tag{29}$$

However, no matter in which format, the convolution operation in the relaxation model is

unavoidable. The direct implementation of convolution usually consumes large memory and

computation time, which is very inefficient. The methods implemented in this paper will avoid

these disadvantages. The details will be discussed and offered in Section 0.

3.2.5 Time domain boundary condition (TDBC) model

The TDBC model developed by Ostashev et al. [43] is based on the impedance relation in

frequency domain.

$$Z(\omega) = Z_\infty \sqrt{\frac{1 - i\omega\tau}{-i\omega\tau}}, \qquad Z_\infty = \frac{\rho c q}{\Omega}, \qquad \tau = \frac{\rho q^2 \gamma}{\sigma_0 \Omega} \tag{30}$$

When we transform Eq. (30) back to the time domain, the pressure at the porous surface is:

$$p(t_n) = Z_\infty[\delta(t_n) + g(t_n)] * u(t_n) \tag{31}$$

where $\delta(t)$ is the Dirac delta function and $g(t)$ is the relaxation function, which is also given by

Ostashev et al.:

$$g(t) = \frac{\exp\left(-\frac{t}{2\tau}\right)}{2\tau} \left[I_1\left(\frac{t}{2\tau}\right) + I_0\left(\frac{t}{2\tau}\right) \right] H(t). \tag{32}$$

Just like the relaxation functions used in the WRX, $g(t)$ also describes the decaying response of the porous medium. Again, the implementation of the TDBC model needs to evaluate a convolution operation.

It should be noticed that Eq. (31) describes the pressure and velocity relation at the boundary. If we use Eq. (31) as a pressure boundary condition, then the velocity boundary condition could be extrapolated as:

$$u(t_n, y_s) = \frac{15}{8} u(t_n, \ y_s + \Delta y) - \frac{5}{4} u(t_n, \ y_s + 2\Delta y) + \frac{3}{8} u(t_n, \ y_s + 3\Delta y) \tag{33}$$

3.3 Implementation of convolution

When evaluating the convolution terms in WRX model, Wilson's original approach requires one to save long solution histories inside the porous material layer [47]. As mentioned earlier, the method consumes large memory and computation time, which is not practical especially for a big 3D simulation case. Ostashev improved the method by implementing a piecewise constant recursive method (PCRC) [43].

The PCRC method includes two steps. Firstly, it approximates the time-domain relaxation function $r(t)$, e.g. Eq. (25) in the WRC model, Eq. (29), in the WRX-S model and Eq. (32) in the TDBC model, with an exponential series as:

$$r(t) \approx \sum_{k}^{N} a_k e^{-\gamma_k t} H(t) \tag{34}$$

The approximation process can be completed in the fashion of curve fitting by using a Matlab 'fminsearch' function, which uses the Nelder-Mead simplex direct search algorithm [94]. In the case of the convolution operation where $\Psi = r(t) * f(t) = \sum_{k}^{N} a_k e^{-\gamma_k t} H(t) * f(t) = \sum_{k}^{N} \Psi_k$, each term of the accumulator Ψ can be expressed as:

$$\Psi_k = \int_0^\infty a_k e^{-\gamma_k t'} f(t - t') dt' \tag{35}$$

Secondly, we assume variable $f(t)$ is a constant within one time-step, $f(t_{n-1}) = f(t_n)$.

Therefore, Eq. (35) in each discrete time step can be integrated out as:

$$\Psi_k^n = e^{-\gamma_k \Delta t} \Psi_k^{n-1} + \frac{a_k}{\gamma_k} f(t_n)(1 - e^{-\gamma_k \Delta t}) \tag{36}$$

Eq. (36) only uses one previous time step information, which greatly reduced memory

consumption. But PCRC is only first order accurate [95]. We can raise the accuracy to second

order by using the piecewise linear recursive method (PLRC), which assumes $f(t)$ changes

linearly between one timestep [73]. The PLRC needs two time steps information in calculation,

its expression can be found as:

$$\Psi_k^n = e^{-\gamma_k \Delta t} \Psi_k^{n-1} + A_k f(t_n) + B_k f(t_{n-1}),$$

$$\text{where } A_k = \frac{a_k}{\gamma_k}\left(1 - \frac{1 - e^{-\gamma_k \Delta t}}{\gamma_k \Delta t}\right), \qquad B_k = -\frac{a_k}{\gamma_k}\left(e^{-\gamma_k \Delta t} - \frac{1 - e^{-\gamma_k \Delta t}}{\gamma_k \Delta t}\right) \tag{37}$$

Therefore, the original WRX, WRX-S and TDBC model can be written as:

WRX:

$$\sigma_0 u + \frac{\rho_0 q^2}{\Omega}\left(\frac{\partial u}{\partial t} + \sum_k^N \Psi_k\right) = -\nabla p, \tag{38}$$

$$\frac{\Omega}{\gamma P_{av}}\left(\frac{\partial p}{\partial t} + (\gamma - 1)\sum_k^N \Phi_k\right) = -\nabla \cdot u \tag{39}$$

WRX-S:

$$\frac{\partial w}{\partial t} = -\frac{\Omega}{\rho_0 q^2}\nabla p + \frac{\Omega}{2\rho_0 q^2}\sum_k^N \overline{\Psi}_k - \frac{1}{\tau_v}w \tag{40}$$

$$\frac{\partial p}{\partial t} = -\frac{\gamma P_0}{\Omega} \nabla \cdot w + \frac{(\gamma - 1)P_0}{\Omega} \sum_{k}^{N} \bar{\Phi}_k \tag{41}$$

TDBC:

$$p(t_n) = Z_\infty \left(w(t_n) + \sum_{k}^{N} \Lambda_k \right) \tag{42}$$

where $\Psi, \Phi, \bar{\Psi}, \bar{\Phi}$, and Λ can be calculated with the PCRC or PLRC method described in Eq. (36) and Eq. (37).

Another approach implemented by Dragna et al. (2015) is the auxiliary differential equation method (ADE). By differentiating Equation (35), auxiliary functions yield:

$$\frac{\partial \Psi_k}{\partial t} + \gamma_k \Psi_k = a_k f(t_n) \tag{43}$$

Eq. (43) is a series of first order ordinary differential equations (ODE). The amount the equations depends on the number of terms (N) that we picked to approximate the relaxation function. With the solutions at the previous time step used as initial conditions, we can solve Eq. (43) along with the original porous medium model. The ADE method does not introduce additional approximations. Therefore, the order of accuracy of the original solver is preserved.

3.4 Validation of method

Before comparing simulation results with experiment results, we would like to verify our implementations first. Some 1D simulations are conducted to compare with the analytical solutions. Then the 2D and 3D simulations, which follow ANSI experiment set up, are performed.

3.4.1 1D wave propagation problem

In a one-dimensional test, the source signal is:

$$Q(t) = (1 - (t - t_0)^2 \omega_0^2) \exp\left(-\frac{(t - t_0)^2 \omega_0^2}{2}\right) \tag{44}$$

where source frequency $\omega_0 = 2\pi f_0$, $f_0 = 800\text{Hz}$, initial time $t_0 = \frac{1}{f_0}$. We set the domain size to

30λ, where λ is the wavelength defined as $\lambda = c_0/f$. The line at $x = 0$ represents the wall,

which separate the computational domain into two parts, air and porous material. As illustrated

in Figure 9 and Figure 10, we let the wave travels from left (air) to right (porous material). The

source location is at 20λ away from the porous surface. The thickness of the porous material is

10λ. The porous material is acoustically soft with $\sigma_0 = 10^3 \text{ Pa·s·m}^{-2}$, $\Omega = 0.5$, $q = 1.8$. This low

flow resistivity material is specially selected to demonstrate the performance of the porous

medium models. The grid space is set to be $\lambda/40$ in air. To ensure a stable and efficient

simulation we set the Courant-Friedrichs-Lewy (CFL) number to 0.3.

Figure 9 captures a moment when the wave-front just reflected from the porous material.

The wavelet on the left represents the strength and the shape of the source. When wall material is

rigid, the reflection wave has the same magnitude and shape as the source. Once we introduced

the porous medium, the strength of the reflection wave became much weaker compared with the

rigid wall due to the energy absorbed by the porous material. The reflection waves calculated by

the ZK model, the TDBC model, and WRX model are almost indistinguishable in Figure 9.

When the wave propagates inside the porous material, the ZK model's results show much higher

magnitude than that from the WRX model. Moreover, if we let the wave keep travelling inside

the porous material as shown in Figure 10, the transmission wave amplitude of the WRX model

drops much quicker than that of the ZK model.
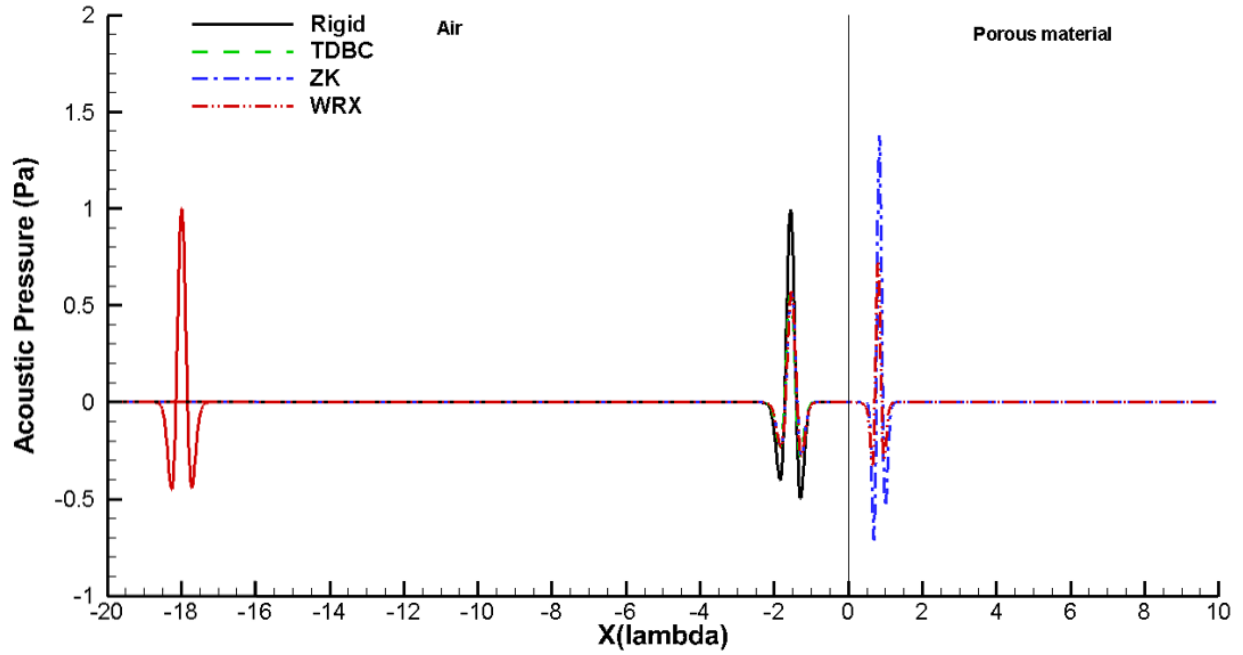
Figure 9. Incident of a wavelet on the porous material in at t = 22.5t_0 with rigid boundary condition, TDBC, ZK, and WRX model.
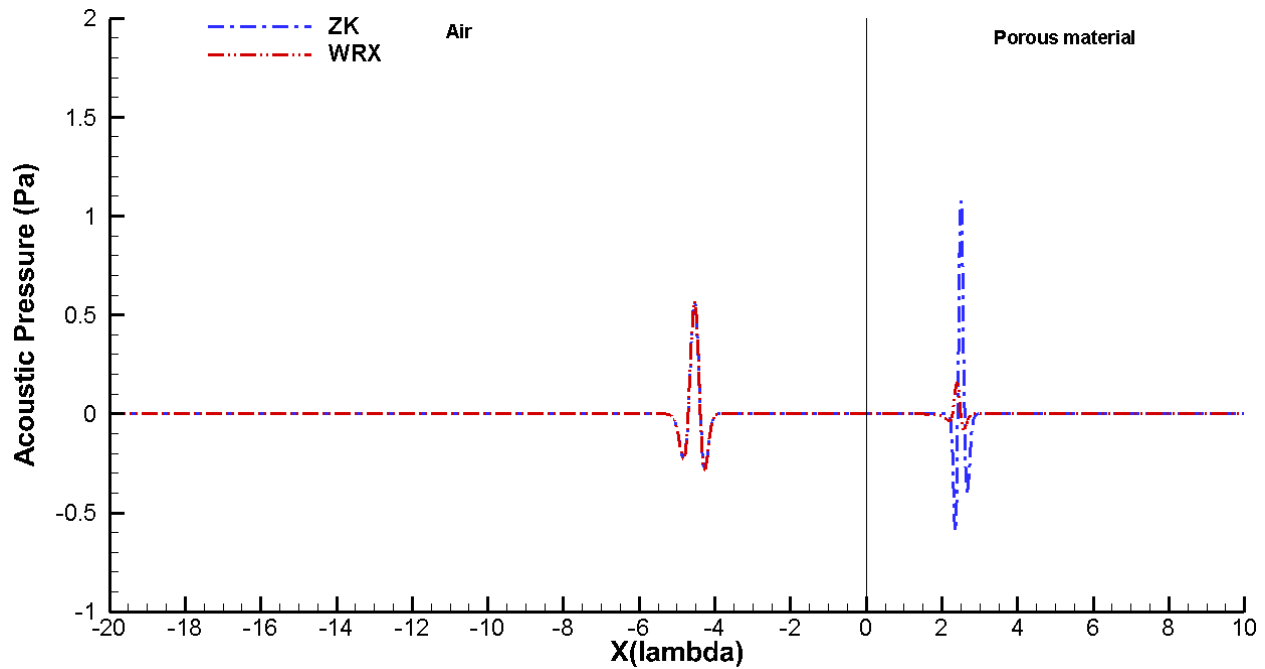
Figure 10. Incident of a wavelet on the porous material in at t = 25.5t_0 with ZK and WRX model

To further understand the results, we compare the numerical computation results to the Wilson's analytical solutions [47]. The analytical solutions for acoustic impedance Z and sound attenuation coefficient α are given as:

$$Z(\omega) = \frac{q\rho_0 c_0}{\Omega}\left[\left(1 + \frac{\gamma - 1}{\sqrt{1 - i\omega\tau_e}}\right)\left(1 - \frac{1}{\sqrt{1 - i\omega\tau_v}}\right)\right]^{-\frac{1}{2}} \tag{45}$$

$$\alpha(\omega) = Imag\left(\frac{q\omega}{c_0}\left[\left(1 + \frac{\gamma - 1}{\sqrt{1 - i\omega\tau_e}}\right) \middle/ \left(1 - \frac{1}{\sqrt{1 - i\omega\tau_v}}\right)\right]^{\frac{1}{2}}\right) \tag{46}$$

With the flow parameters given, we can plot out Z and α easily in Figure 11 and Figure 12. On

the other hand, if we pick a point inside the porous material layer and monitor its pressure and

velocity history, the acoustic impedance and the attenuation coefficient can also be calculated

theirs definition as:

$$Z(\omega, y) = \frac{\hat{P}(\omega, y)}{\hat{U}(\omega, y)}, \qquad where \; \hat{P}(\omega, y) = \mathcal{F}\big(p(t, y)\big),$$

$$\hat{U}(\omega, y) = \mathcal{F}\big(u(t, y)\big) \tag{47}$$

$$\alpha(\omega, y) = \log\big(|\hat{P}(\omega, y)|\big) / \log\big(|\hat{P}(\omega, y + \Delta y)|\big) / \Delta y \tag{48}$$

It should be noticed that since the TDBC method does not calculate the acoustic filed

inside porous material layer, the nodal valued at the boundary was monitored. The frequency

domain pressure and velocity $\hat{P}, \hat{U}$ in Eq. (47) are obtained with fast Fourier transformation

(FFT) of the recorded time histories at the monitor point.
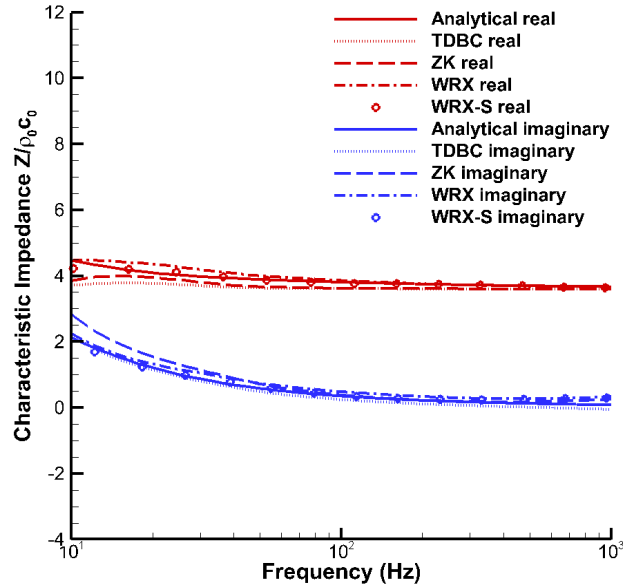
Figure 11. Characteristic impedance comparison between analytical and numerical solutions.
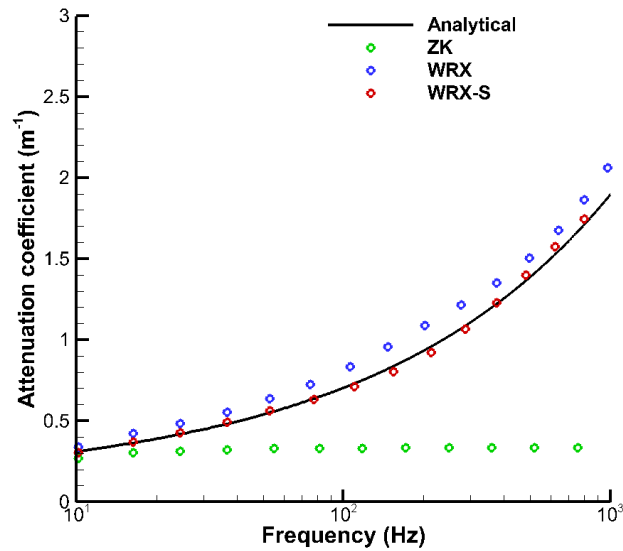
Figure 12. Attenuation coefficient comparison between analytical and numerical solutions.

Characteristic impedance curves given in Figure 11 show all models agree with analytical solutions well, except at very low frequency. The sound attenuation coefficient comparison is illustrated in Figure 12. The α from the ZK model presents an almost constant value, which only matches the analytical solution at the low frequency. Since ZK model's assumption is constant material properties, flat attenuation curve is within our expectation. The WRX model, as a

frequency-dependent material model, appears to match the analytical solution better, especially the WRX-S model.

3.4.2 2D/3D wave propagation problem

In this section, we will compare two-dimensional / three-dimensional simulation results with the available measurement data.

Alberts and Sanchez measured sound pressure level difference (LD) under different ground conditions. Their measurement setup follows the ANSI S1.18 requirement [96]. Therefore, we also set up our simulations accordingly. The 3D simulation domain is 2m in the x-direction, 2.5m in the y-direction, and 2m in the z-direction. To model the wave propagation inside the porous ground, we set the ground thickness to 0.2m. The perfectly-matched-layer (PML) boundary conditions are specified at front, back, right and top of the domain with a thickness of 0.2m to prevent the additional reflections. The source signal is a Gaussian pulse which can be described as:

$$Q(x, y, z) = \exp(-300r^2), \qquad r^2 = (x - x_0)^2 + (y - y_0)^2 + (z - z_0)^2 \qquad (49)$$

The source is located at $(0, 0, 0.325)$. The upper and lower receivers are set at $(0, 1.75, 0.23)$ and $(0, 1.75, 0.46)$, respectively. The 2D simulation is carried out with the size in the x-direction being set to 0m as presented in Figure 13.
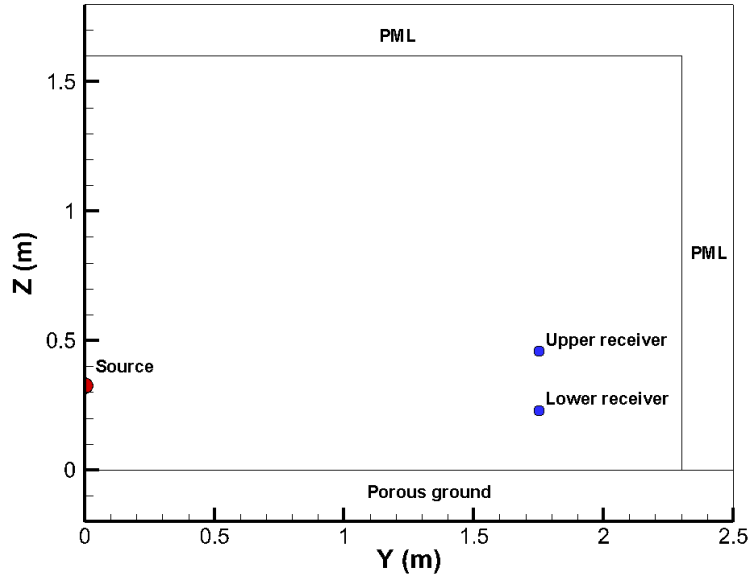
Figure 13. Front view of ANSI S1.18 test set up (2D setup)

By curve fitting the spherical wave reflection coefficient, Alberts and Sanchez were able to find out the flow resistivity σ_0 and the porosity gradient α_e used in ANSI's two-parameter model from measured SPL difference. Readers can find details in ANSI/ASA, 2010 and Alberts and Sanchez, 2013. In the simulation below, we will use $\sigma_0 = 51375.65$ Pa·s·m^{-2}, $\alpha_e = 53.3$ m^{-1}. It should be noticed that tortuosity q and porosity Ω are still undefined. These two parameters can be measured non-acoustically, but here we still use the curve fitting method which suggests $q = 1.79$, $\Omega = 0.87$. The detail of the curve fitting process will be given in Section 3.5.
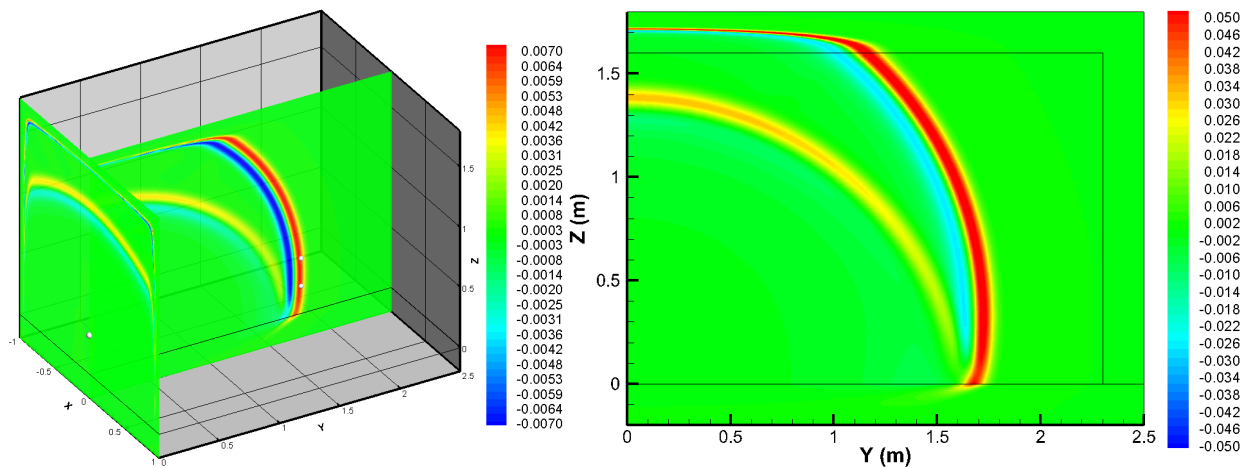
Figure 14. 3D and 2D simulated pressure contour when simulation time t = 5ms.

Figure 14 gives the 3D and 2D simulated pressure contour at $t = 5$ms. The porous medium is modeled with the WRX model. A strong waver-front, a weaker reflection wave and an even weaker transmission wave inside porous ground can be clearly observed. We can also observe the contour level's difference between 2D and 3D simulation. This is due to the distance effect. To compare simulation results with the measurement results, the LD between upper and lower receiver is calculated as:

$$LD = 20 \log_{10} \frac{\hat{p}_{upper}}{\hat{p}_{lower}} \tag{50}$$

where $\hat{p}_{upper}$ and $\hat{p}_{lower}$ are calculated by Fourier transform of receiver's pressure time history to frequency domain. Figure 15 gives LD comparison between the 2D and the 3D simulation. Two curves are almost indistinguishable. Therefore, we will use 2D simulation results in the following text considering cost and efficiency.
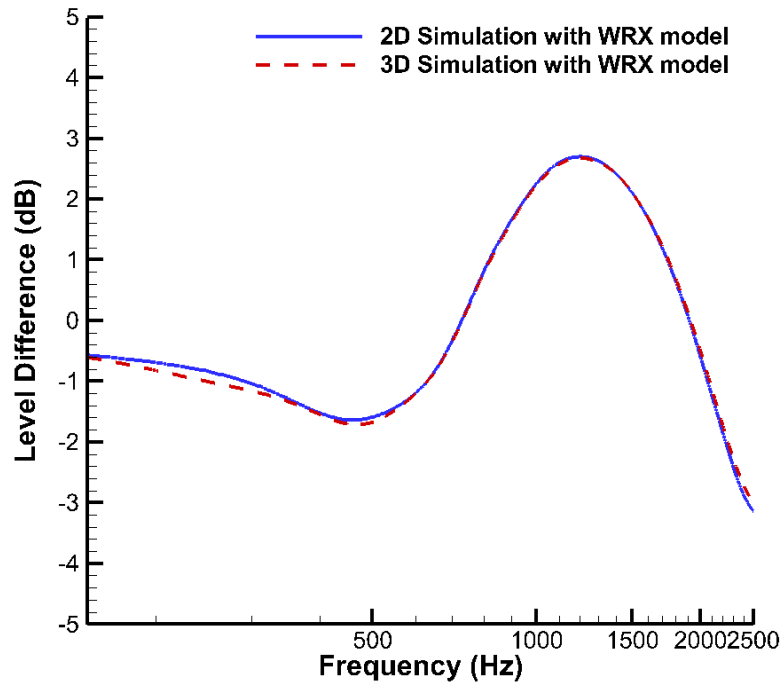
Figure 15. Comparison between 2D and 3D simulation results

To compare the numerical prediction results with measurement results, we also conducted simulations with other porous material models. The corresponding LD curves are given in Figure 16. The numerical predictions, no matter from which model, all present lower magnitudes and shifted phases comparing with physical measurements. It should be noticed that the relaxation functions used in the WRX model or the TDBC model are constructed artificially by connecting high and low frequency limit with a smooth function. However, this smooth function might not reflect the physical condition.
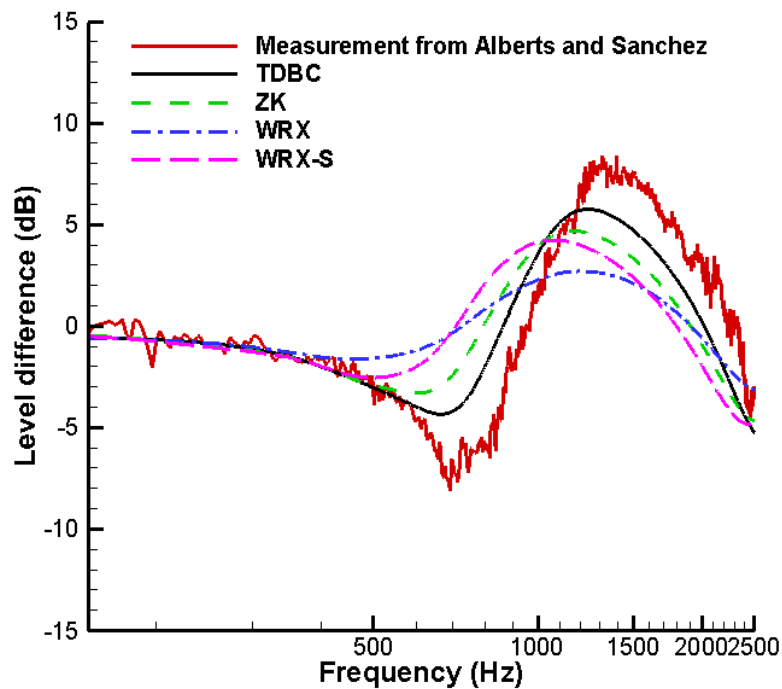
Figure 16. Sound pressure level difference between upper and lower receiver from measurements and different porous material models.

3.5 Improvement of the relaxation function in TDBC model

The method provided in ANSI/ASA S 1.18 offered an approach that connect the LD measurements with the frequency domain impedance [90]. On the other hand, with the existing pressure and velocity equations, we can analytically derive impedance equation in frequency domain from our original models. The ideal is once we can match our analytical frequency

domain impedance with ANSI's impedance model, our frequency domain model should also match the physical measurement results. Therefore, when we transform this 'matched model' back to the time domain, the corresponding time-domain simulation results would be corrected. If we take TDBC model as an example, the acoustic impedance in TDBC model can be found as [43]:

$$Z(\omega) = Z_\infty \left(1 + \frac{\hat{f}(\omega)}{\tau} \right). \tag{51}$$

Here $\hat{f}(\omega)$ is the relaxation function in frequency domain. We also approximated the time-domain relaxation function with an exponential series as mentioned in Section III:

$$f\left(\frac{t}{\tau}\right) \approx \sum_k^K a_k e^{-\frac{\gamma_k t}{\tau}} \tag{52}$$

Transform the above time-domain approximation function to frequency domain yield:

$$\hat{f}(\omega) = \mathcal{F}\left(f\left(\frac{t}{\tau}\right) \right) \approx \mathcal{F}\left(\sum_k^K a_k e^{-\frac{\gamma_k t}{\tau}} \right) = \sum_k^K \frac{a_k \tau}{\gamma_k - i\omega\tau} \tag{53}$$

Therefore, the impedance relation in Eq. (51) yields:

$$Z(\omega) \approx Z_\infty \left[1 + \sum_k^K \frac{a_k}{\gamma_k - i\omega\tau} \right] \tag{54}$$

When we plug the original parameters that we found by fitting the relaxation function Eq. (34) into Eq. (54) the impedance curves in Figure 17 appear to deviate from ANSI's impedance results a lot. The fact supports our hypothesis that the modeled relaxation function may cause mismatches between simulation results and physical measurements. Hence, instead of using the exponential serial to approximate the modeled time-domain relaxation function in Eq. (32), we would like to use Eq. (54) to approximate the ANSI's two-parameter impedance model in Eq. (19). It should be noticed that since relaxation time τ is a function of tortuosity q and

porosity Ω, q and Ω can be found out by using a Matlab 'fminsearch' function which match Eq. (54) to Eq. (19). Additionally, the Eq. (54) is in the form of a rational function. Therefore, when q and Ω values are found, we can use vector fitting method to quickly refine the pole values [97-99].
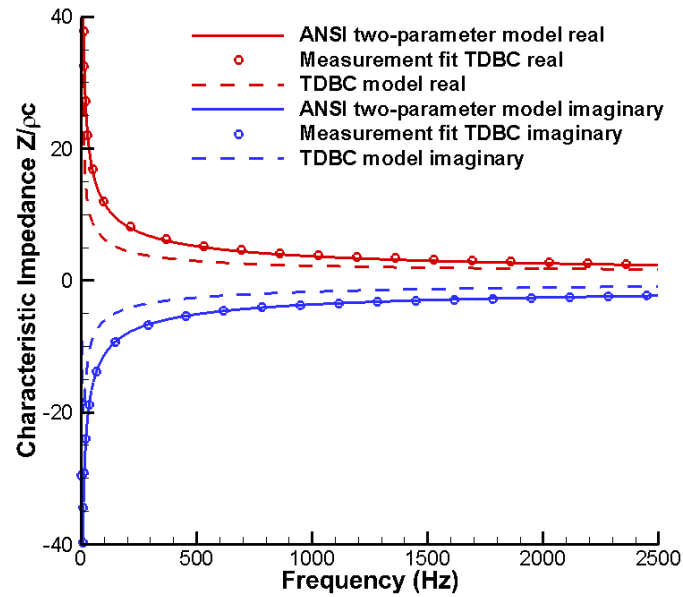
Figure 17. Comparsion of characteristic impedance between ANSI two-parameter model and TDBC model

The parameters $a_k, and\ \gamma_k$ found by fitting impedance curves are exactly the parameters that we need to construct a new time-domain relaxation function. Figure 18 shows the new time-domain relaxation function along with the old function. The new function is still a decaying curve but presents higher magnitude at the same moment.
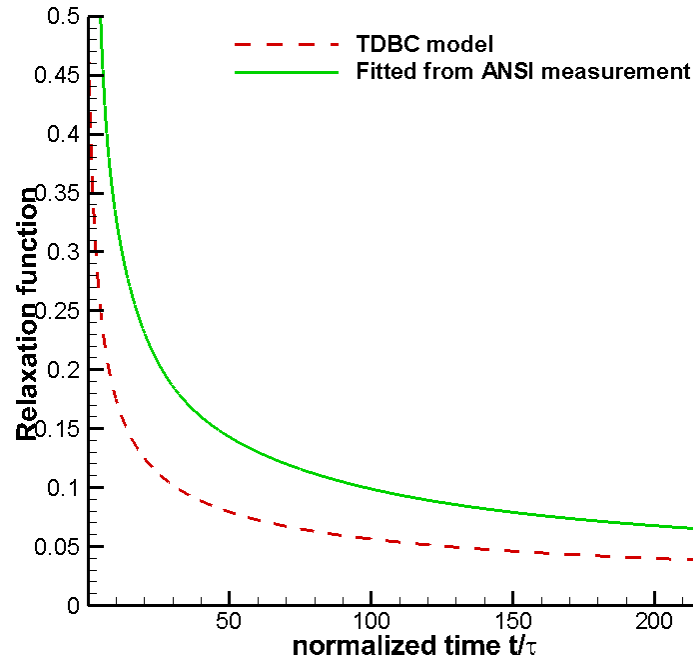
Figure 18. Comparison of modeled relaxation fucntion and measurement fitted relaxation function.

By using this new measurement fitted relaxation function, the SPL difference predicted by the TDBC model are improved significantly. Figure 19 gives the SPL difference plot for four tests, which flow resistivities are in different range. All simulation results the measurements.

(a)   (b)

(c)

(d)
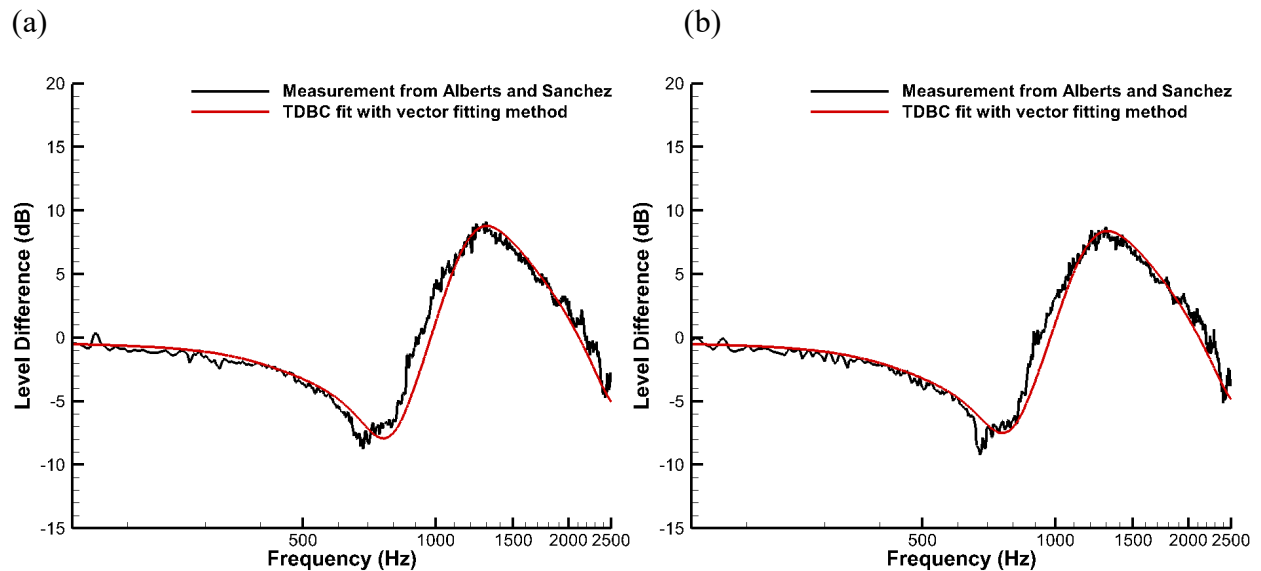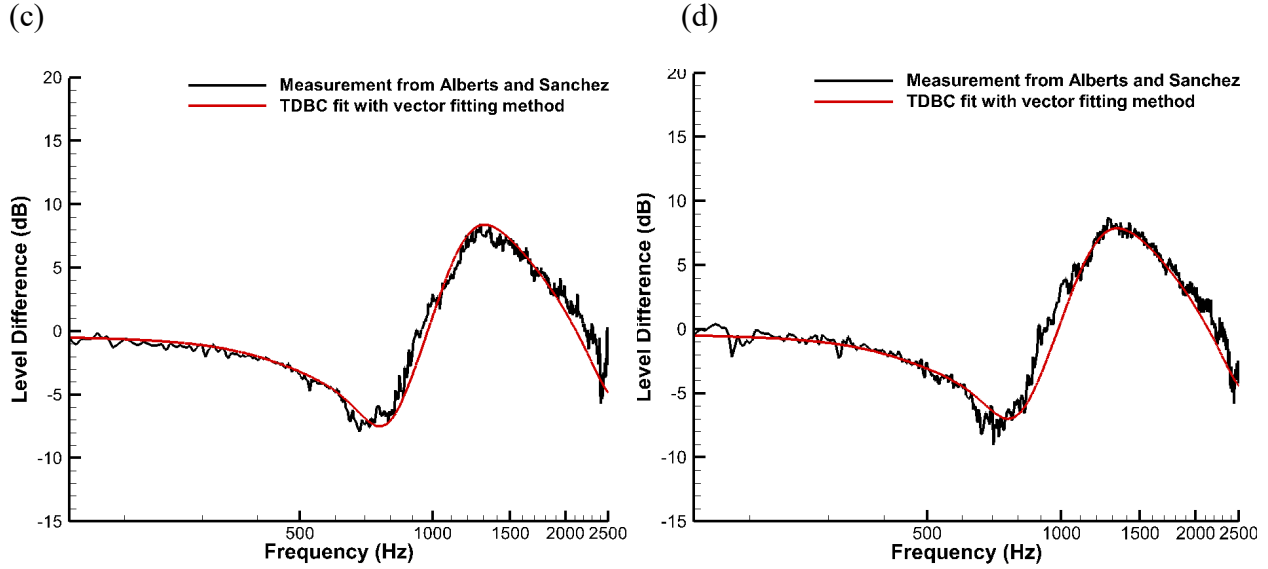
Figure 19. Sound pressue level difference comparsion between measurement and the fitted TDBC model, (a) σ = 51375.65 Pa·s·m^{-2},α_e =53.3 m^{-1}; (b) σ = 54350.37 Pa·s·m^{-2},α_e =41.6 m^{-1}; (c) σ = 66107.51 Pa·s·m^{-2},α_e =9.97 m^{-1}; (d) σ = 62097.75 Pa·s·m^{-2},α_e =23.5 m^{-1};

3.6 Improvement of the relaxation function in WRX model

The TDBC method only describes a boundary condition. When porous material layer is thin, the penetration of the wave needs to be considered. In this case, we would like to use the WRX model to explicitly model the porous medium layer. We also want to apply the same matching method described in Section 3.5 to the WRX model. The frequency domain impedance in the WRX model is:

$$Z(\omega) = Z_\infty \sqrt{\frac{\dfrac{i\sigma_0\Omega}{\omega\rho_0 q^2} + 1 + S(\omega\tau_v)}{1 + (\gamma - 1)S(\omega\tau_e)}}, \tag{55}$$

When fitting Eq. (55) to Eq. (19), the resultant relaxation functions not always showing a decaying performance, which also lead to a bigger mismatch between measurement results and simulation results demonstrated in Figure 20 (c) and Figure 20 (d). Since Eq. (55) describes the

ratio of two relaxation functions, the matching of the two functions' ratio does not necessarily

ensure each relaxation function will follow the realistic condition.

The Critical frequency f_c of porous material can be found as [100]:

$$f_c = \frac{\sigma_0^2 \Omega^2 \Lambda'^2}{8\pi v q^2}$$

(56)

where Λ' is the characteristic viscous length of the ground and v is the kinematic viscosity of the

air. Here, when we plug in the porous ground material properties, f_c value can be found around

1.68×10^4Hz. Since the frequency, f, we studied is from 150Hz to 2500Hz, which means $f \ll$

f_c, our study can be considered as a low frequency study. In the low frequency region, the

viscous effects dominate [101]. Therefore, we only consider the vorticity relaxation process in

the original WRX model, which leads to a new system:

$$\sigma_0 u + \frac{\rho_0 q^2}{\Omega} \left\{ \frac{\partial u}{\partial t} + \mathcal{F}^{-1}[S(\omega \tau_v)] * \frac{\partial u}{\partial t} \right\} = -\nabla p$$

(57)

$$\frac{\Omega}{\gamma P_0} \frac{\partial p}{\partial t} = -\nabla \cdot u$$

(58)

We call Eq. (57) and Eq. (58) vorticity relaxation model (WRX-V). The corresponding

analytical impedance and sound attenuation coefficient can be found as:

$$Z = \frac{q\rho_0 c_0}{\Omega} \left[\gamma \left(1 - \frac{1}{\sqrt{1 - i\omega\tau_v}} \right) \right]^{-1/2}$$

(59)

$$\alpha = Imag \left(\frac{q\omega}{c_0} \left[\frac{\gamma}{\left(1 - \frac{1}{\sqrt{1 - i\omega\tau_v}} \right)} \right]^{\frac{1}{2}} \right)$$

(60)

Following the same fitting process, we can find out corresponding a_k and γ_k to construct a new

relaxation function. With the new relaxation function, the simulation results are given in Figure

20. The SPL difference in Figure 20 tends to shift towards the high frequency. But when we compare them with the original WRX model's predictions, the WRX-V's results are much better.

(a)

(b)

(c)

(d)
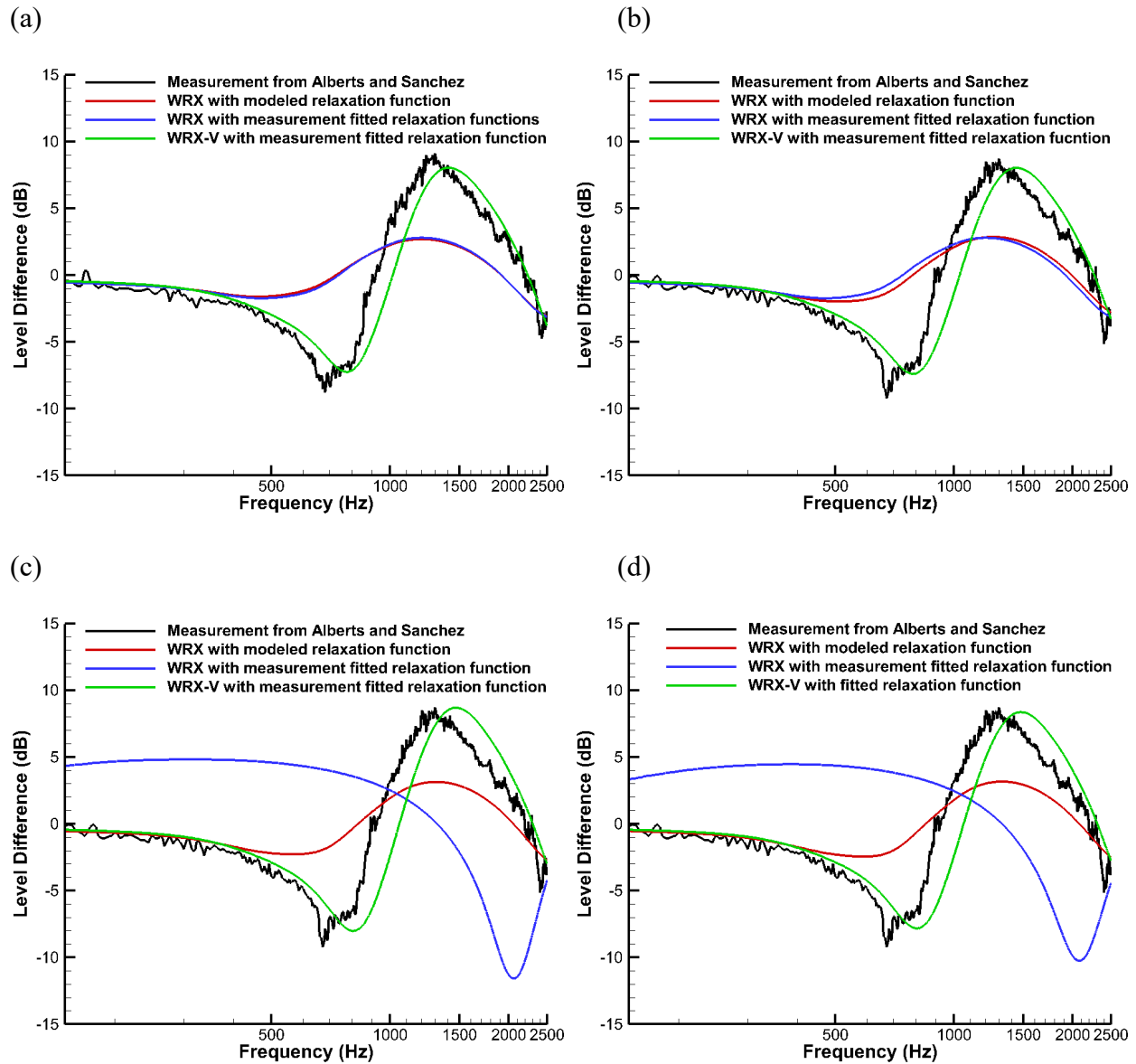
Figure 20. Sound pressue level difference comparsion between measurement, WRX model, fitted WRX model, and fitted WRX-V model, (a) σ = 51375.65 Pa·s·m^{-2},α_e =53.3 m^{-1}; (b) σ = 54350.37 Pa·s·m^{-2},α_e =41.6 m^{-1}; (c) σ = 66107.51 Pa·s·m^{-2},α_e =9.97 m^{-1}; (d) σ = 62097.75 Pa·s·m^{-2},α_e =23.5 m^{-1};

3.7 Summary

The time-domain porous medium model simulation results match the analytical solutions well. The frequency-dependent material models (WRX and TDBC) present better acoustic attenuation prediction comparing with the ZK model. However, the WRX model and the TDBC model's predictions still show deviations comparing with physical measurements. The mismatches are caused by the difference between the modeled relaxation function and the physical relaxation process.

To improve the TDBC model's prediction, we proposed a new approach that constructed a relaxation function by fitting the original model's frequency domain impedance performance with ANSI's two-parameter impedance model. The new relaxation function shows a very good performance in the TDBC model. The predicted LD curves match measurements well. A vorticity relaxation function model is also proposed for simulate wave propagation in porous media at low frequency. With the same fitting process, the WRX-V's predictions significantly improved the results from the original WRX model.

This study proposed a new approach where, with a simple sound pressure level measurement or impedance measurement which following ANSI's set up, one can define the relaxation function of a specific porous ground. With this new relaxation function, the original frequency-dependent porous material model's prediction can be significantly improved.

Chapter 4.   Numerical modeling of the exterior-to-interior sound transmission through building materials

4.1 Introduction:

Usually in outdoor acoustics we treat the wall of a building as a rigid material, which will reflect most of the acoustic waves. In this manner, transmission wave would be so weak that we can hardly receive sound signals inside the room. However, due to the vibration of the wall or windows caused by the outdoor noise source, people usually hear some level of noise inside the room. The vibration of the wall will generate pressure distributions, which will act as an additional source and influence the indoor object. In the vibro-acoustic field, scholars and engineers usually split this kind of problem into three parts: (1) exterior sound propagation and induced structural loading; (2) structural response; and (3) interior acoustic response [102, 103]. There are two approaches to simulate this phenomenon. The first approach couples the governing equations in both fluid and solid mechanics to solve the problem [103-106]. The other approach considers that the walls are deformable poroelastic material. Therefore, Biot theory is used to model the structural response [35, 107-109].

Inspired by the poromechanics approach, we would like to test a new method by simplifying the whole solid wall to be a porous medium layer. The idea is: since the sound will reach the receiver room regardless the path, if we can match the SPL of the measurements with our simulation, we will be able to simplify the complicated structure response with a porous medium layer.

Two wall configurations will be considered in this study. For exterior walls we will use one layer of gypsum board as presented in Figure 21 (a) since Thomas and his colleagues tested

a similar design [110]. For interior walls, we will use double leaf wall as given in Figure 21 (b) which is also measured by Arjunan and his colleagues [103, 104, 106].

(a)   (b)
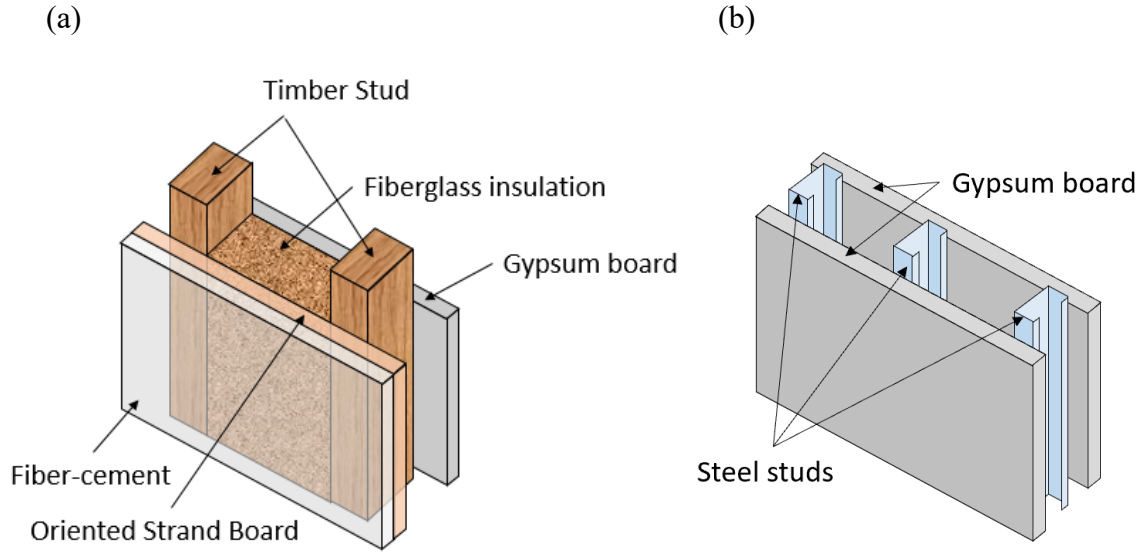
Figure 21.a) Exterior and b) Interior wall layer configuration

4.2 Numerical method:

Combining the linearized Euler sound propagation equations in air with those equations in a porous medium in the form of the Zwikker-Kosten (Z-K) equation, yields

$$\frac{\partial \boldsymbol{u}}{\partial t} + (\boldsymbol{u}_{av} \cdot \nabla)\boldsymbol{u} + (\boldsymbol{u} \cdot \nabla)\boldsymbol{u}_{av} = -\alpha_{av}\nabla p - \alpha\nabla p_{av} + f_u \tag{61}$$

$$\frac{\partial p}{\partial t} + (\boldsymbol{u}_{av} \cdot \nabla)p + (\boldsymbol{u} \cdot \nabla)p_{av} = -\gamma p \nabla \cdot \boldsymbol{u}_{av} - \gamma p_{av}(\nabla \cdot \boldsymbol{u}) + f_p \tag{62}$$

where f_u and f_p are fictitious body forces to enforce the velocity and pressure to accommodate the governing equations in air and inside a rigid or porous object, which are given by:

$$f_u = \begin{cases} 0, & Outside\ the\ porous\ medium \\ \alpha_{av}\nabla p + \alpha\nabla p_{av} + (\boldsymbol{u}_{av} \cdot \nabla)\boldsymbol{u} + (\boldsymbol{u} \cdot \nabla)\boldsymbol{u}_{av} - \frac{\Omega}{q^2}\alpha_{av}\ (\nabla p + \sigma\boldsymbol{u}), & Inside\ the\ porous\ medium \end{cases} \tag{63}$$

f_p

$$= \begin{cases} 0, & \textit{Outside the porous medium} \\ \gamma p \nabla \cdot \boldsymbol{u}_{av} + \gamma p_{av}(\nabla \cdot \boldsymbol{u}) + (\boldsymbol{u}_{av} \cdot \nabla)p + (\boldsymbol{u} \cdot \nabla)p_{av} - \dfrac{\gamma p_{av}}{\Omega}(\nabla \cdot \boldsymbol{u}), & \textit{Inside the porous medium} \end{cases} \qquad (64)$$

where $\boldsymbol{u}_{av}$, p_{av} and α_{av} are the time averaged velocity, pressure, and specific volume, respectively; $\boldsymbol{u}$, p and α are the corresponding acoustic fluctuations, with α given as:

$$\alpha = -\frac{p}{\gamma p_{av}\rho_{av}}, \qquad (65)$$

where γ is the specific-heat ratio. The coefficients, Ω, q, and σ in Eqs. (63) and (64), are porous medium porosity, tortuosity, and flow resistivity, respectively.

If we use Wilson's relaxation model (WRX). The fictitious body forces are

f_u

$$= \begin{cases} 0, & \textit{Outside the porous medium} \\ \alpha_{av}\nabla p + \alpha\nabla p_{av} + (\boldsymbol{u}_{av} \cdot \nabla)\boldsymbol{u} + (\boldsymbol{u} \cdot \nabla)\boldsymbol{u}_{av} - \dfrac{\Omega}{\rho_0 q^2}\alpha_{av}(\nabla p + \sigma\boldsymbol{u}) - \displaystyle\sum_{k}^{N}\Psi_k, & \textit{Inside the porous medium} \end{cases} \qquad (66)$$

f_p

$$= \begin{cases} 0, & \textit{Outside the porous medium} \\ \gamma p \nabla \cdot \boldsymbol{u}_{av} + \gamma p_{av}(\nabla \cdot \boldsymbol{u}) + (\boldsymbol{u}_{av} \cdot \nabla)p + (\boldsymbol{u} \cdot \nabla)p_{av} - \dfrac{\gamma p_{av}}{\Omega}(\nabla \cdot \boldsymbol{u}) - \displaystyle\sum_{k}^{N}\Phi_k, & \textit{Inside the porous medium} \end{cases} \qquad (67)$$

The accumulator in Eq (6) and (7) are calculated with PCRC method as:

$$\Psi_k^n = e^{-\gamma_{v_k}\Delta t}\Psi_k^{n-1} + \frac{a_{v_k}}{\gamma_{v_k}}p(t_n)\left(1 - e^{-\gamma_{v_k}\Delta t}\right) \qquad (68)$$

$$\Phi_k^n = e^{-\gamma_{e_k}\Delta t}\Phi_k^{n-1} + \frac{a_{e_k}}{\gamma_{e_k}}u(t_n)\left(1 - e^{-\gamma_{e_k}\Delta t}\right) \qquad (69)$$

where $a_{v_k}, \gamma_{v_k}, a_{e_k}, \gamma_{e_k}$ are found by curve fitting exponential series with the approximated relaxation function as:

$$\sum_{k}^{N} a_k e^{-\gamma_k t} \approx \frac{1}{\sqrt{\pi\tau t}}\exp\left(-\frac{t}{\tau}\right)H(t) \qquad (70)$$

4.3 Numerical simulation:

We will test two wall materials and a window glass material in several 2D simulations. After simulation results match with the measurement results, we will apply the corresponding material parameters which found in the 2D simulation to the final 3D simulations.

4.3.1 Component level test

The measurement results present in Arjunan and his colleagues' work [104] present noise reduction performance of a double leaf wall, which is a noise insulation wall configuration usually used in indoor. To study the wall material properties, we set up our simulation domain according to the measurement layout noted in his research as showing in . The source room on the left is 4.9m long in the y-direction; the double leaf wall sample with thickness of 0.1m is located in the middle of the domain; the receiver room on the right is 4.5m long. The total width of the room is 3.9 m. The detail set up can be A source is located in the middle of the left wall of the source room at (0, 1.95). The source is in the form of Gaussian pulse as:

$$p = \exp(-40r^2) \tag{71}$$

Two receivers are places at source room and receiver room with location of (2.45, 1.95), (7.20, 1.95). Total simulation time is 0.24s, grid size is 0.0025m, and CFL number is set to be 0.3 to ensure a stable and efficient computation.
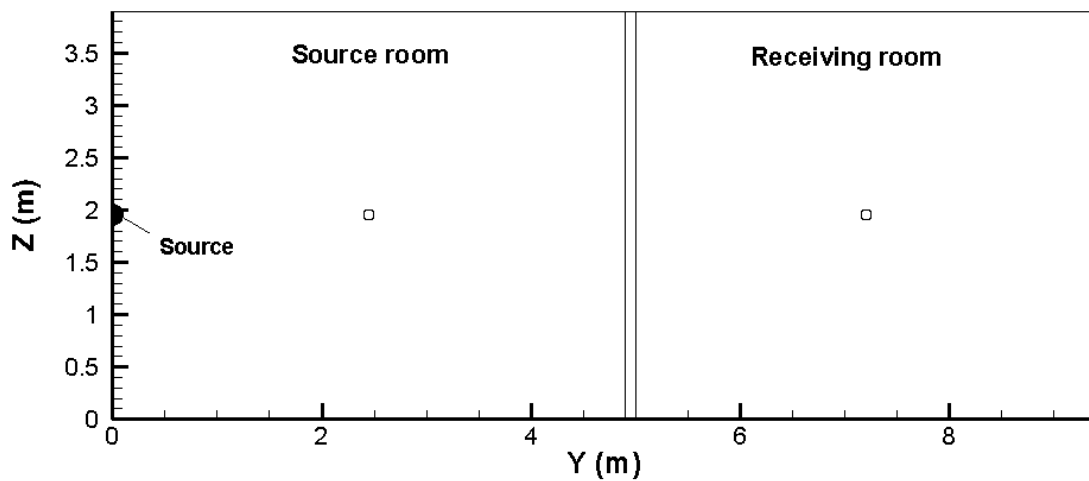
Figure 22. 2D simulation set up according to measurement layout in Arjunan et,al. [104]

We start the investigation from different value of flow resistivity σ. Four σ values are tested with porosity Ω and tortuosity q being set to the same value. It can be found in Figure 23 that the indoor and outdoor noise reduction index varies with flow resistivity, lower flow resistivity tend to lead to lower sound reduction effect. After comparison between four tests, flow resistivity of $\sigma = 5 \times 10^4 \, Pa \cdot s \cdot m^{-2}$ is picked.
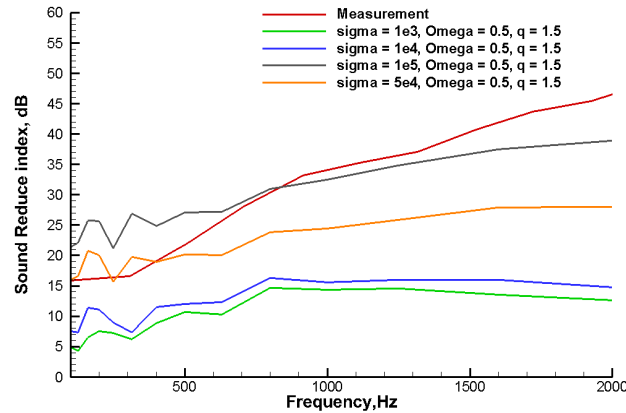
Figure 23. Sound reduction index of different flow resistivity σ values

Different porosity values are given in Figure 24. When porosity increase, the noise reduction index value at low frequency region still remains same, but in high frequency region, the value starts to increase and approaching the measurement results. Similar phenomenon can be observed with different tortuosity value in Figure 25.
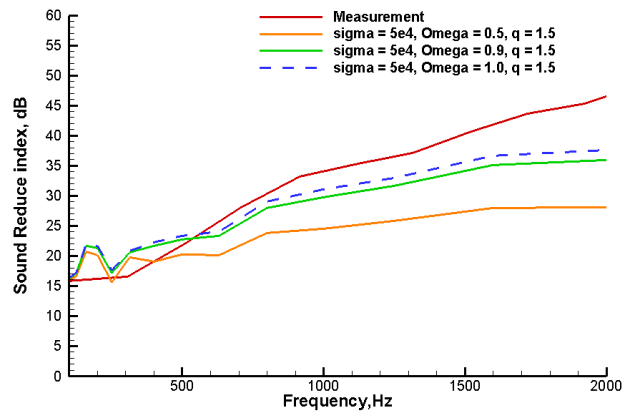
Figure 24. Sound reduction index of different porosity Ω values

Figure 25. Sound reduction index of different tortuosity q values

With the simulation results from the three studies, we picked the flow resistivity $\sigma = 5 \times 10^4 \; Pa \cdot s \cdot m^{-2}$, porosity $\Omega = 0.9$ and tortuosity $q = 1.0$. Since the picked flow resistivity is relatively low, we tested the case with the WRX model. The results in Figure 26 shows the simulation results from WRX match measurements better especially in the high frequency range.
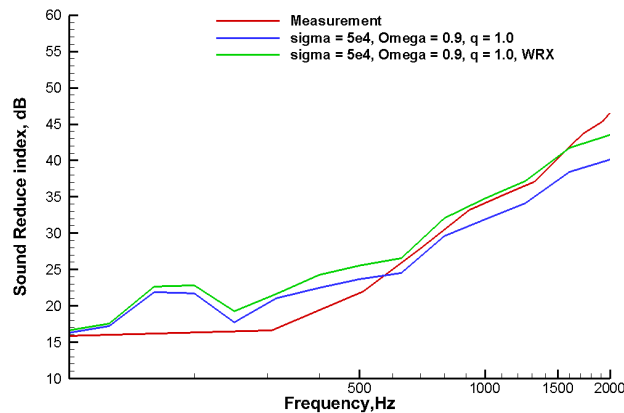
Figure 26. Sound reduction index curve from ZK model and WRX model comparing with measurements

If we take a close look at the material properties picked above, $\Omega = 0.9$ tells us the 90% of the material is void; $q = 1.0$ means the speed of sound inside the porous material layer is almost same as speed of sound in the air. Actually, this matches the physical structure of the interior double leaf wall.

We can apply the same method to fit the exterior wall and windows material noise reduction curve with physical measurements.
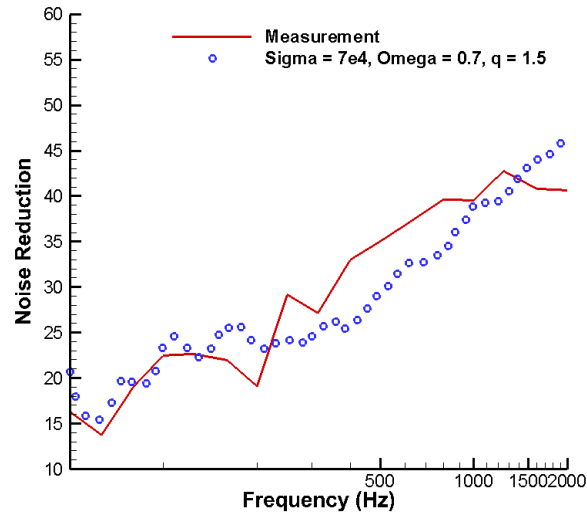
Figure 27 Noise reduction comparison between simulation results and measurement results
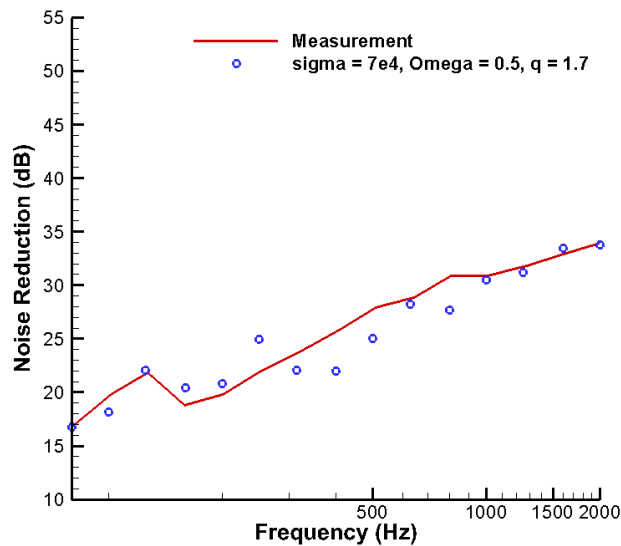
Figure 28. Sound pressure level difference comparison between ZK model, WRC model along with measurement results.

4.3.2 Assemble level 3D simulation

After match each part of the building's material acoustic response to the measurement results, we can get all material parameters summary in the Table 2.

Table 2 Material properties of building's exterior wall, interior wall, and glass window.

Material	Flow resistivity σ (Pa· s· m^{-2})	Porosity Ω	Tortuosity q	Model
1. Interior Wall	3×10^4	0.9	1.0	WRX
2. Exterior Wall	7×10^4	0.7	1.5	ZK
3. Glass Window	7×10^4	0.5	1.7	ZK

The building given in Figure 29 is firstly built up in CAD package based on floor plan and measurements. The full geometry is then imported into the numerical simulation solver. All exterior walls including roof are modelled with material #2, all interior walls are modelled with material #1, windows with material #3, ground with rigid material.

Computational domain is 17.43m in the x-direction, 21.72m in the y-direction, 7.95m in the z-direction. The origin of the coordinate is set at south east lower corner of the first floor at exterior side. Grid size is 0.015m, time step is 1.5e-5s, and total simulation time is 0.225s. Source is located at (-5.39, 3.21, 0.83). Five receivers are randomly placed at surface of the south side exterior wall of the living room. And anther fiver receivers are placed inside the living room. To accommodate the complicated geometries, immersed boundary method is used.

(a)   (b)

(c)

(d)
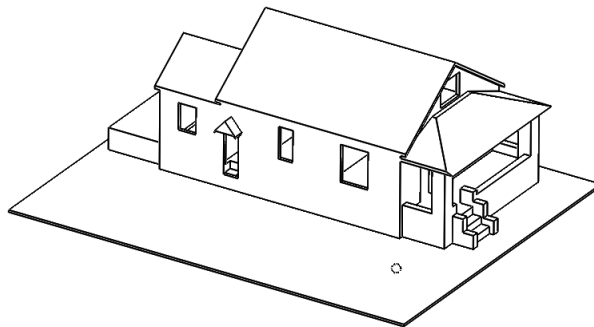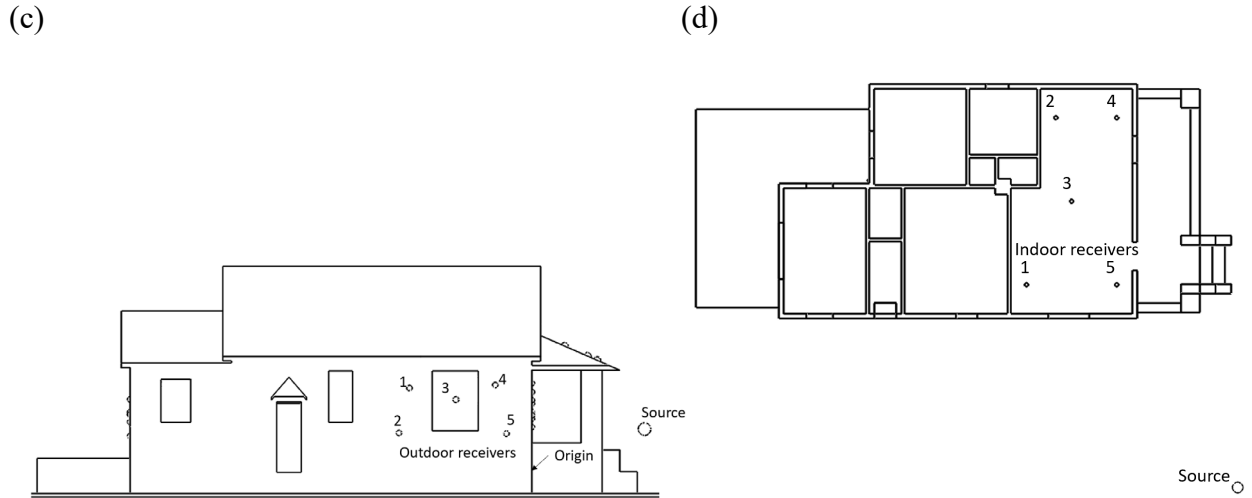
Figure 29. House used in simulation a) ISO view of the physical house, b) ISO view of the CAD model, c) Front view of the house, d) Top view of the first-floor section
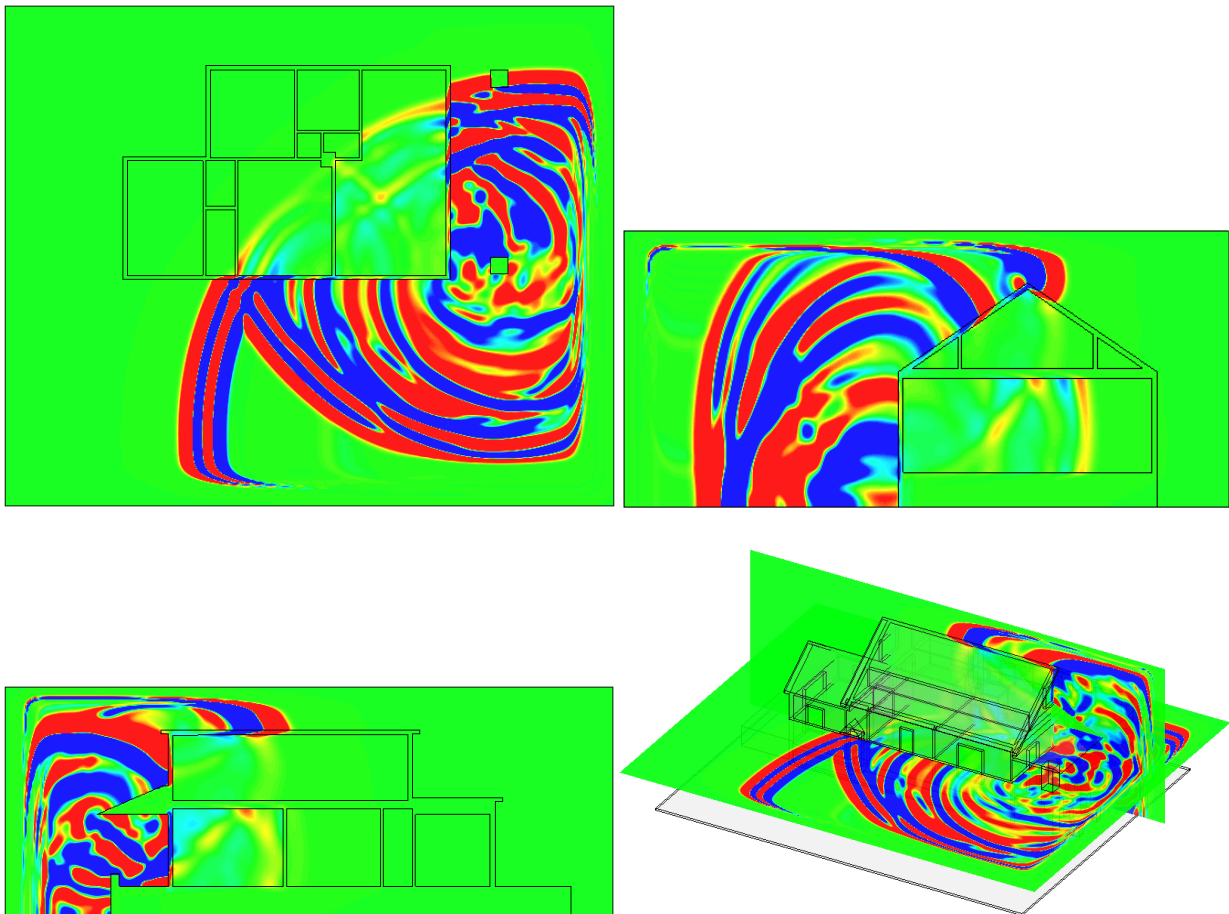
Figure 30. Simulation contours of a) top view, b) side view, c) front view, d) ISO view

The acoustic pressure contours at simulation time 36ms are given in Figure 30, it can be found the geometry details of the buildings are captured. Reflections from the wall and diffractions by the roof can be observed in Figure 30. The transmission waves are also captured inside room with much lower magnitude due to the absorption of the porous wall.

The Noise level difference between outdoor and indoor are given in Figure 31. Two curves compare the noise level difference between open window and closed window simulation. It can be found:

- With all windows opened, the geometry and wall of the house can provide around 15dB reduction of the noise across a wide frequency range.
- When windows are closed the noise are more likely to be attenuated, especially at high frequency range.
- The low frequency signals can penetrate the room even when windows are closed.
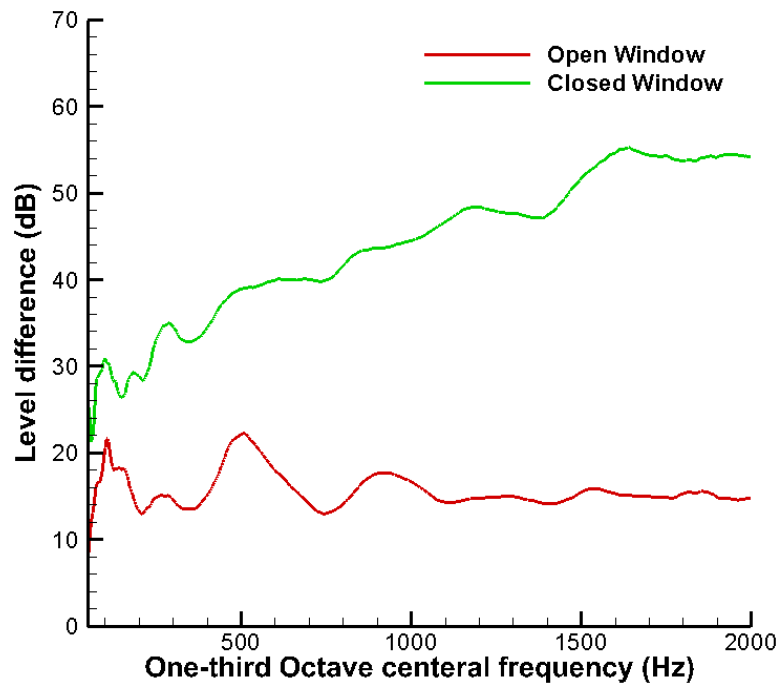
Figure 31. Noise reduction at living room when all windows are open/closed

4.4 Summary

In this study the porous media model is coupled with immersed boundary method to solve for a noise reduction problem for a two-story house. The rigid wall is acoustically modelled with porous material layers. Therefore, the noise caused by vibration of the building wall is simplified by the penetration wave from the porous media. By matching the measurement response of each part of the building material to the simulation results. The acoustics properties of each part of the building can be found. After assembling all the materials into a 3D simulation, the acoustic response of a house can be found. The study presented a method that single components measurement can be used to back out the acoustic properties of each component of a building. Then, the whole acoustic response of a house can be achieved by assembling acoustic properties of each part into an over-all simulation.

Chapter 5. Time-Domain Simulation of Ultrasound Propagation with Fractional Laplacians for Lossy-Medium Biological Tissues with Complicated Geometries

5.1 Introduction

Ultrasound has been widely used as a diagnostic tool in medical imaging for over 50 years. Its applications have been extended to destroy kidney stones, kill malignant tissues and cosmetic surgery [111, 112]. Focused ultrasound beam can also be used to remove the brain tumors [113]. A recent study shows that ultrasound techniques in conjunction with microbubbles can be used to safely open the blood–brain barrier (BBB) for brain drug delivery, which is a new treatment in instance of stroke or Alzheimer's disease [114, 115]. Therefore, using ultrasound safely requires accurate planning, which motivates accurate ultrasound simulation techniques.

A lossy medium is a medium in which a significant amount of acoustic energy is absorbed per unit distance traveled by sound wave. Most of the biological tissues can be considered as lossy media. Sound attenuation is usually used to quantify energy loss in lossy media, which has also been found following the power law in the frequency domain as [50, 51]:

$$\alpha = \alpha_0 |\omega|^y \tag{72}$$

where α is sound attenuation with a unit of Np/m, α_0 is absorption coefficient, ω is angular frequency, and y is power law exponent of the specific material with a value between 0 to 2.

This study presents an approach in which a simple structured Cartesian grid mesh can be used to solve ultrasound propagation problem with any irregular geometry of lossy media. And the frequency power attenuation law, Eq. (72), can be satisfied. The finite-difference time-domain (FDTD) method is coupled with the IB method to accommodate complicated geometries [2, 89, 116]. The lossy medium is modeled with the Chen and Holm's equation [52]. In order to calculate the fractional Laplacian terms in the model, the fractional central difference method

(FCD) [117] is used. The perfectly matched layer (PML) boundary is used to mimic a free space condition [92]. This new approach, different from the "k-space" method, does not need additional correction factors or integral transforms and can accommodate complicated geometries with a simple structured mesh.

The governing equations will be presented in Section 5.2, along with the detailed numerical method. Simulation examples of sound propagation inside the lossy medium are given in Section 5.3. After comparing the numerical simulation results with the analytical power attenuation law, we will discuss the results and offer the conclusion in Section 5.4. The order of accuracy of the scheme is also evaluated and presented in Appendix.

5.2 Numerical method

5.2.1 Governing equations in lossy media

Two media are considered in this study: water and the lossy-medium biological tissue. The linearized Euler equations for wave propagation in water are:

$$\frac{\partial \boldsymbol{u}}{\partial t} + (\boldsymbol{u_0} \cdot \nabla)\boldsymbol{u} + (\boldsymbol{u} \cdot \nabla)\boldsymbol{u_0} = -\frac{1}{\rho_0}\nabla p + \frac{p}{\rho_0^2 c_0^2}\nabla p_0, \tag{73}$$

$$\frac{\partial p}{\partial t} + (\boldsymbol{u_0} \cdot \nabla)p + (\boldsymbol{u} \cdot \nabla)p_0 = -\rho_0 c_0^2(\nabla \cdot \boldsymbol{u}) + f_p, \tag{74}$$

where, $\boldsymbol{u_0}, p_0$ and ρ_0 are time averaged velocity, pressure, and density of water. $\boldsymbol{u}, p$ and ρ are their corresponding acoustic fluctuations, c_0 is the speed of sound in water, and f_p is the fictitious term for implementing the immersed-boundary method, which will be explained later. In water, if there is no back ground flow and the background pressure is a constant value, Eqs. (73) and (74) become:

$$\frac{\partial \boldsymbol{u}}{\partial t} = -\frac{1}{\rho_0}\nabla p, \tag{75}$$

$$\frac{\partial p}{\partial t} = -\rho_o c_0^2 \nabla \cdot \boldsymbol{u}, \tag{76}$$

In lossy media, conservation of mass is expressed as:

$$\frac{\partial \rho}{\partial t} = -\rho_1 \nabla \cdot \boldsymbol{u}, \tag{77}$$

where ρ_1 is the density of the lossy medium. Conservation of momentum is still in the form of Eq. (75). The relation between acoustic pressure and acoustic density in the lossy medium is derived by Treeby and Cox (2010) based on Chen and Holm's equation as:

$$p = c_1^2 \left\{ 1 - \tau \frac{\partial}{\partial t} (-\nabla^2)^{\left(\frac{y}{2}-1\right)} - \eta(-\nabla^2)^{\frac{y+1}{2}-1} \right\} \rho, \tag{78}$$

where c_1 is the speed of sound in the lossy medium, and τ and η are proportionality coefficients. Substituting Eq. (77) into Eq. (78) gives the acoustic pressure propagation equation in the lossy medium as:

$$\frac{\partial p}{\partial t} = -\rho_1 c_1^2 \nabla \cdot \boldsymbol{u} + \tau c_1^2 (-\nabla^2)^{\frac{y}{2}} p + \eta \rho_1 c_1^2 (-\nabla^2)^{\frac{y+1}{2}-1} (\nabla \cdot \boldsymbol{u}). \tag{79}$$

The proportionality coefficients, τ and η, follow the relations:

$$\tau = -2\alpha_0 c_1^{y-1}, \tag{80}$$

$$\eta = 2\alpha_0 c_1^{y} \tan(\pi y / 2), \tag{81}$$

where the coefficients are chosen as: $y = 1.9$, $\alpha_0 = 2.9858 \times 10^{-10}$ dB· Hz^{-y}·m^{-1}, $c_1 = 2000$ m/s, $\rho_1 = 1500$kg/m^3 to simulate a relatively hard tissue. The corresponding proportionality coefficients based on Eqs. (80) and (81) are:

$\tau = -5.58494 \times 10^{-7}$dB·s·m^{y-2}, $\eta = -0.00018$ dB·m^{y-1}.

5.2.2 Computation of fractional derivatives

Consider the Riesz fractional derivatives equal to the fractional Laplacian operator [118] given below:

$$-(-\nabla^2)^{\frac{y}{2}}f = \frac{\partial^y f}{\partial |x|^y} + \frac{\partial^y f}{\partial |z|^y}. \tag{82}$$

The fractional central difference (FCD) method [117, 119] can be used to numerically approximate the Riesz fractional derivatives in Eq. (82). For a continuous function $f(x, z)$, each term in Eq. (82) can be expressed as:

$$\frac{\partial^y f_{i,j}}{\partial |x|^y} = -\frac{1}{\Delta x^y} \sum_{q=i-e(j)}^{i-w(j)} \omega_q f_{i-q,j}, \qquad \frac{\partial^y f_{i,j}}{\partial |z|^y} = -\frac{1}{\Delta z^y} \sum_{q=j-n(i)}^{j-s(i)} \omega_q f_{i,j-q}, \tag{83}$$

where the weight function ω_q is:

$$\omega_q = \frac{(-1)^q \Gamma(y+1)}{\Gamma\left(\frac{y}{2}-q+1\right)\Gamma\left(\frac{y}{2}+q+1\right)}, q = 0, \mp 1, \mp 2, \dots \tag{84}$$

The fractional derivative terms in Eq. (79) are approximated with the summation of the weighted pressure or velocity gradients in space using Eq. (83). Comparing this method with the convolution method used in Norton and Novarini (2003), the memory requirement is reduced significantly.

For an irregular shape lossy medium, the grid number required in computation are different in the x- and z-directions. Therefore, it is necessary to identify the range of the lossy medium in each direction. A horizontal line crosses the boundaries in Figure 32 can have two intersections at the east and west boundaries of the geometry. Those intersection points are not necessarily located on the boundaries because of the Cartesian grid mesh used in the simulation. Therefore, they are approximated with the closest grids, $e(j)$ and $w(j)$, near the boundaries. Similar approximation is needed along a vertical line as shown in Figure 32. When the IB method is implemented, those boundary grids, $e(j), w(j), n(i),$ and $s(i)$, are flagged and stored at the beginning of the computation, as demonstrated in Figure 32. This makes the implementation of FCD method very simple and efficient.
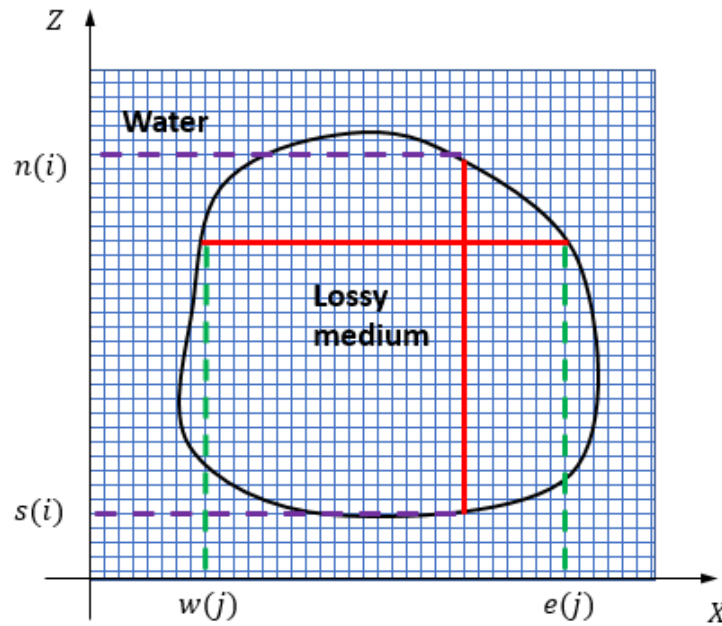
Figure 32. Grid mesh around an irregular-shaped lossy medium in the Cartesian coordinates surrounded by water

5.2.3 *Immersed-boundary method*

The f_p in Eq. (74) is the fictitious term in the immersed-boundary method, which is used to represent the material change between water and the lossy medium. The existence of the boundaries of the lossy medium is represented by switching the fictitious force in the equation. The computation can be performed as if there are no boundaries. In Eq. (74), the fictitious force term for the immersed-boundary method implementation is expressed as:

$$f_p = \begin{cases} 0, & \\ \quad\quad Outside\ the\ lossy\ meidum & \\ \rho_o c_0^2 \nabla \cdot \boldsymbol{u} - \rho_1 c_1^2 \nabla \cdot \boldsymbol{u} + \tau c_1^2 (-\nabla^2)^{\frac{y}{2}} p + \eta \rho_1 c_1^2 (-\nabla^2)^{\frac{y+1}{2}-1}(\nabla \cdot \boldsymbol{u}). & \\ \quad\quad Inside\ the\ lossy\ medium & \end{cases} \quad (85)$$

The acoustic pressure outside the lossy medium is modeled with original pressure equation, Eq. (76), as the linearized Euler equation with $f_p = 0$. The convection terms are neglected assuming the background flow speed is low. The pressure inside the lossy medium is modeled with Treeby and Cox's equation as $f_p = \rho_o c_0^2 \nabla \cdot \boldsymbol{u} - \rho_1 c_1^2 \nabla \cdot \boldsymbol{u} + \tau c_1^2 (-\nabla^2)^{\frac{y}{2}} p +$

$\eta \rho_1 c_1^2 (-\nabla^2)^{\frac{\gamma+1}{2}-1}(\nabla \cdot \boldsymbol{u})$. This is constructed so that when substituting f_p back to Eq. (74), the lossy medium model equation, Eq. (79), is resumed. Therefore, by switching the fictitious force term, the same computational solver can be used simultaneously for both materials. Moreover, with this method, a Cartesian grid mesh, regardless of the complicated object boundaries in the simulation domain, can be used to solve for the acoustic field.

To absorb numerical reflections by computational domain boundaries, the perfectly-match-layer (PML) boundary [92, 120] methods are used on the outside boundaries of the domain. The PML boundary condition has been successfully implemented and verified in our previous work [2, 25, 116] for the FDTD simulation.

5.3 Numerical simulation and results discussion

5.3.1 Ultrasound propagation in the lossy medium and water

Our first simulation is for acoustic propagation in the lossy medium only. A simulation for ultrasound propagation in water is also conducted as a reference. The size of the computational domain is 0.06m × 0.06m. A uniform Cartesian-type mesh with the grid size of $\triangle x = \triangle z = 2.5 \times 10^{-5}$m ensures at least 20 grid points are used per wavelength for ultrasound frequencies up to 1.5MHz. The speeds of sound of water and the lossy medium are set to 1500m/s and 2000 m/s, respectively. The density of water and lossy medium are set to 1000kg/m^3 and 1500kg/m^3. The Courant-Friedrichs-Lewy (CFL) number is chosen to be 0.3 to satisfy a stable computation. It should be noted that if we reorganize Eq. (79) by moving the convection term to the left hand side, the left hand side is still in the form of Euler equation. The two fractional Laplacian terms on the right hand side of equation are calculated as the summation of a series, which is not part of the finite difference scheme. Therefore, the original stability criteria of the scheme in Zheng and Li (2008) should still apply.

The plane wave is set along the left boundary as:

$$p(t) = \cos(2\pi f_0 t) \left[1 - \cos(2\pi f_1 t)\right] \tag{86}$$

where f_0 is the center frequency chosen as $f_0 = 1.3$ MHz, and f_1 is 0.2 MHz that dominates the plane wave bandwidth. Only one period (based on f_1) of the signal is used in the simulation. The top and bottom boundary conditions are set to be symmetric. The right boundary is rigid. To prevent the influence of reflection waves from the right boundary, we ended the simulation at 30μs, before the waves reach the right boundary so that no reflections occur. The indices, $e(j), w(j), n(i),$ and $s(i)$ indicate the grid points on the left, right, top and bottom boundaries of the computational domain, respectively. Four receivers are placed along the centerline of $z = 0.03$m, at $x = 0.005$m, 0.015m, 0.025m, and 0.035m to record the acoustic pressure histories in these locations. It should also be noted that we used this 1D problem to perform 2D simulation, for the purpose to verify the implementation of PMLs in the z-direction for preparing for the following IB method study. It is evident that the implementation of PMLs was successful. More details on the PML implementation can be found in [121].

Figure 33 shows acoustic pressure contours at simulation time $t = 22.5$μs. The plane wave in lossy medium travels further than that in water at this moment. However, the pressure magnitude in water is much higher at this moment, which can also be observed from receiver pressure histories in Figure 34. The phase shift in Figure 34 between solid and dashed lines can be explained by the speed of sound difference in the two media. Pressure histories of the four receiver locations in water show almost the same magnitude, while the pressure magnitude is gradually decreasing along the wave propagation direction in the lossy medium. The phenomenon agrees with the definition of lossy medium that the acoustic energy is absorbed with the distance travelled in the medium.
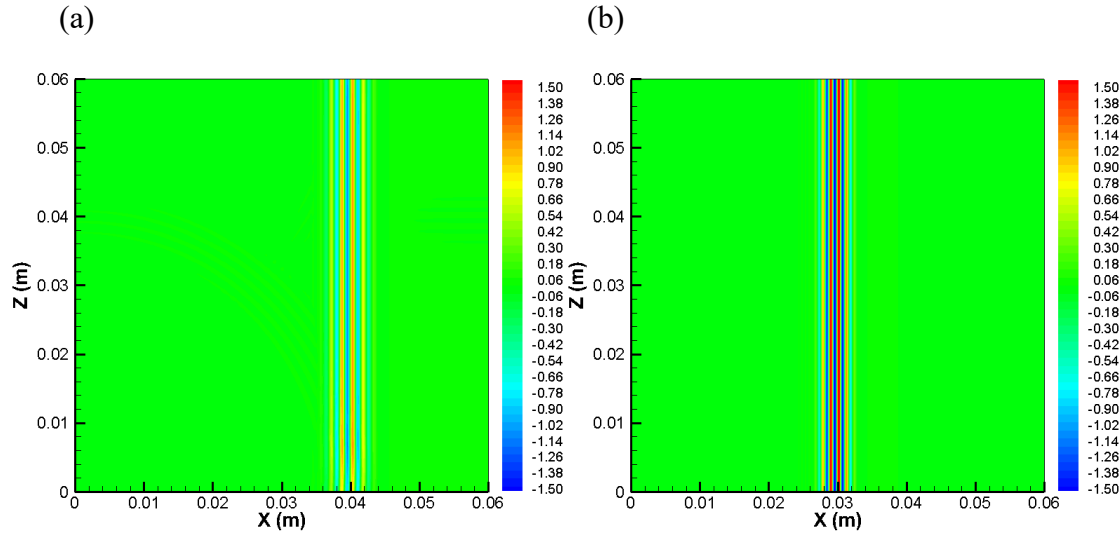
Figure 33. Pressure contours of plane wave propagation at $t = 22.5$ μs in (a) the lossy medium, (b) water
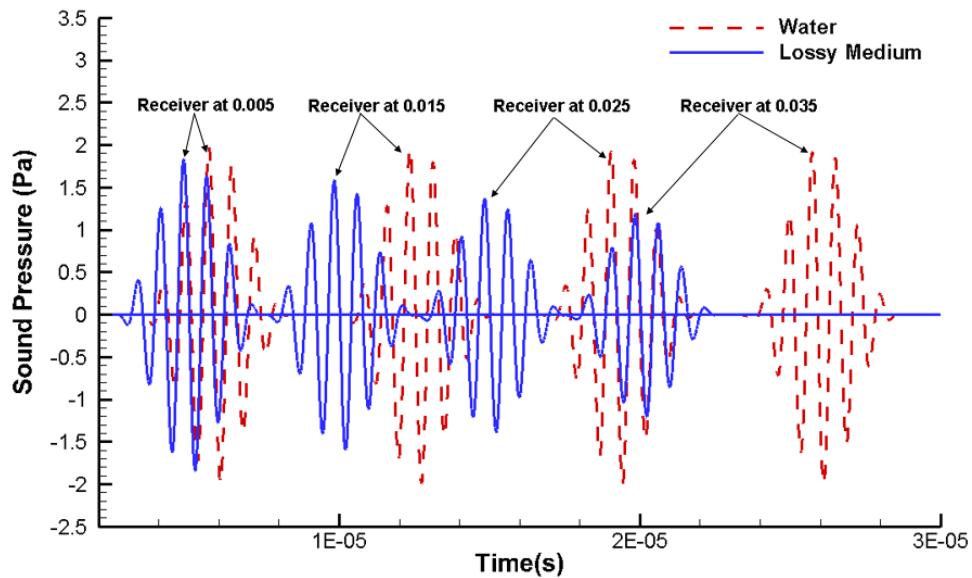
Figure 34. Four receiver readings in two simulations, solid line: lossy medium simulation, dash line: water simulation.

5.3.2 Comparison with the analytical solution

To quantitatively verify the simulation results, a comparison with the frequency-domain power attenuation law is conducted. The analytical solution of attenuation in the lossy medium is described in Eq. (1). To obtain the attenuation from the time-domain numerical calculation, the pressure histories recorded in Section III.A are used. After the Fourier transform, the power

spectrum density (PSD) can be used to calculate the sound attenuation (SA) in the frequency domain as:

$$SA = -20 \log_{10} \frac{PSD_{lossy}}{PSD_{water}}. \tag{87}$$

By averaging the sound attenuation over the wave propagation distance d, the normalized sound attenuation α from numerical simulation is calculated as

$$\alpha_n = \frac{SA}{100 \cdot d}, \tag{88}$$

It should be noted that the unit of α in Eq. (72) is Np/m. A unit conversion from Np to dB is necessary to compare with the SA obtained from Eq. (87). The comparison of sound attenuation values between the numerical solutions and the analytical solutions for different power law exponents, y, are plotted in Figure 35. All simulation results show perfect agreements with the analytical solutions.
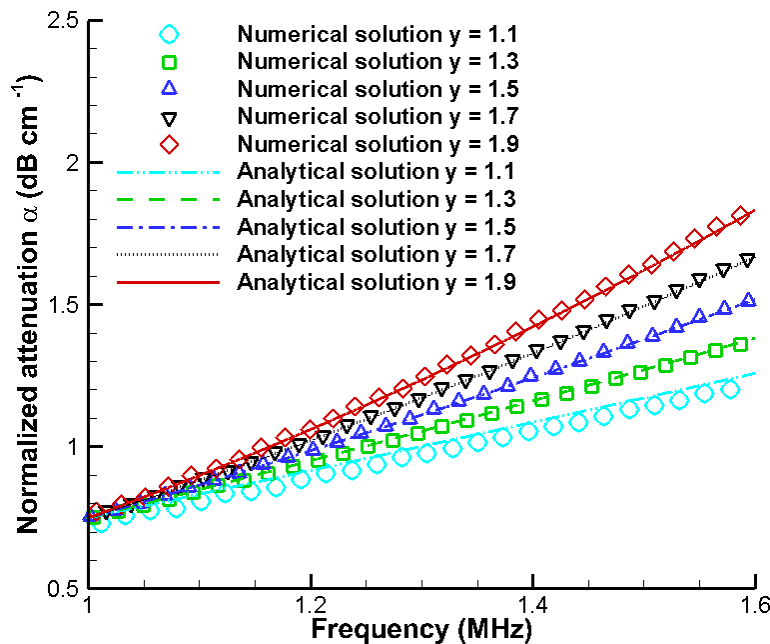
Figure 35. Simulated attenuation curves (symbols) compared with analytical solutions (lines) when $\alpha_0 = 2.9858 \times 10^{-10}$ dB$\cdot$ Hz$^{-y}\cdot$m^{-1}(equivalent to $\alpha_0 = 0.75$ dB$\cdot$MHz$^{-y}\cdot$cm^{-1}) with different power law exponents

5.3.3 Simulation of ultrasound propagation in a complicated geometry

The successful verification of the FCD in the lossy medium simulation enables further implementation for simulating wave propagation in complicated geometries. A piece of ring-shaped lossy medium, which is intended to represent a bone-type biological material is placed in the middle of the computation domain, with the inner diameter of 0.05m and outer diameter of 0.015m. The ultrasound source is placed on the left boundary from the height of 0.025m to 0.035m to represent an ultrasound transducer. The total simulation time is 38μs, which allows the incident ultrasound waves to fully pass the ring-shaped lossy medium.
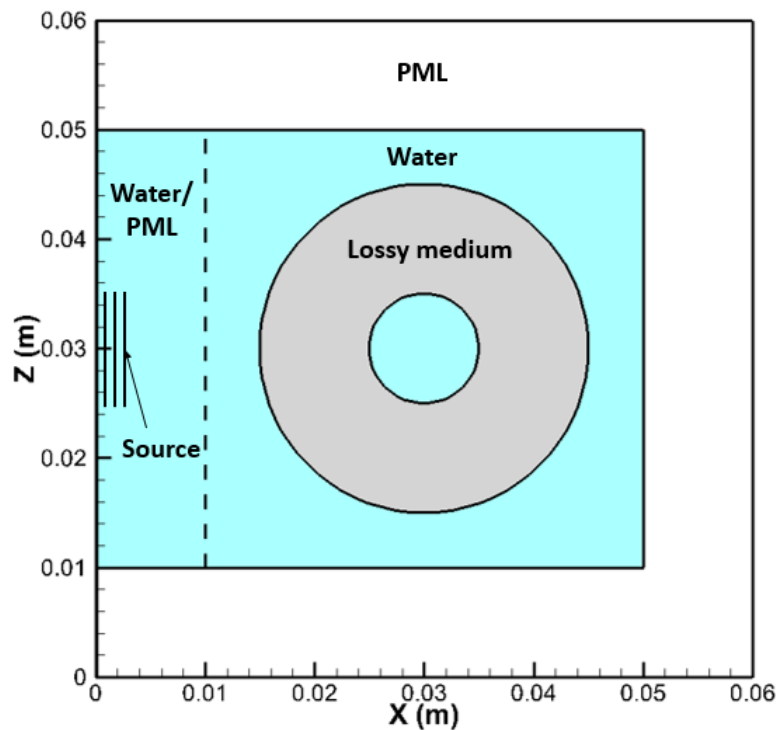
Figure 36. Numerical simulation setup for a ring-shaped complex geometry, with the blue area representing water, the grey area in the middle representing the lossy material, and the white area representing the PML boundaries. The plane wave source is located on the left boundary from z = 0.025m to 0.035m.

The detailed simulation setup is shown in Figure 36. The areas in blue, grey, and white indicate water, lossy medium, and PML respectively. The simulation domain is surrounded by PMLs with a thickness of 0.01m to eliminate reflection waves from the computational boundaries. The dashed line on the left is to indicate that the area on the left side of the line will be switched into PML once the wave fully passed through. The medium interfaces, represented by the two concentric circles in the domain, are not aligned with the Cartesian grid mesh. Therefore, the immersed-boundary method is used to accommodate the cut-through Cartesian grid mesh between the interfaces of water and the lossy medium. The closest node points are used as the boundary points in the case of cut-through.

Figure 37 presents acoustic pressure contours recorded at four different time moments. Reflection waves can always be found at the interface, which are formed due to the material difference of the two media and the geometrical shapes of the interfaces. For example, when waves propagate from the lossy medium to water in Figure 37(b) and from water to lossy medium in Figure 37(c), the two plots clearly capture the backward reflection waves. When the waves leave the lossy medium in Figure 37(d), they are much weaker than the incident waves in Figure 37(a), which shows the combined effects of wave reflection and dispassion due to the lossy medium.

To illustrate the capability of the simulation, a multiple-source simulation is conducted. The same type of plane waves are specified on top, bottom, left and right boundaries. Pressure contours at different simulation moments can be found in Figure 38. The wave patterns are more complicated due to interactions of multiple incoming waves with the ring-shaped lossy medium. Comparing Figure 37(c) with Figure 38(d), which are at the same moment, the effect of multiple incident sources can be observed clearly.
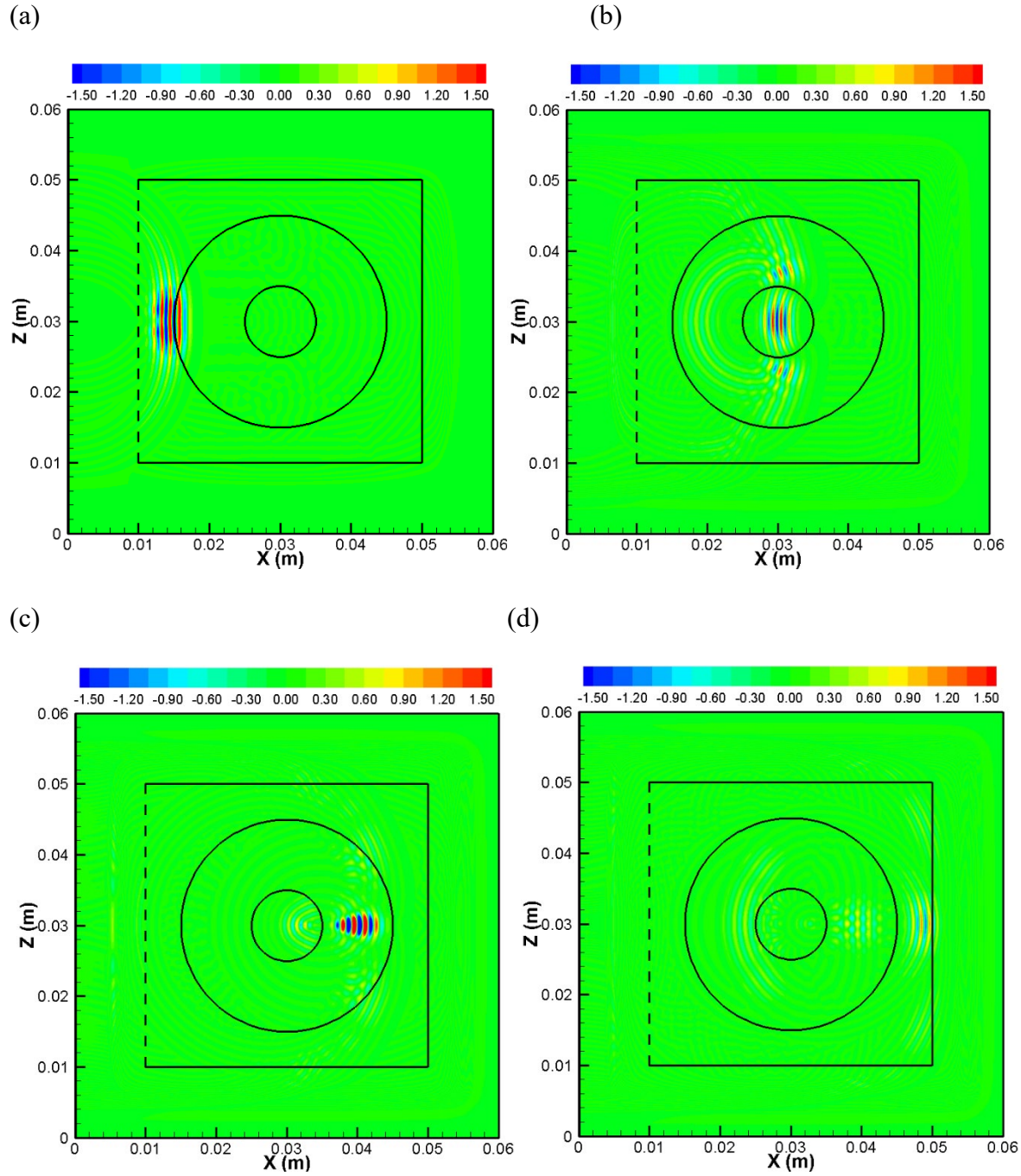
Figure 37. Pressure contours of single-source ultrasound propagation at different moments: (a) t = 12.5μs (b) t = 20μs (c) t = 27.5μs (d) t = 32.5μs
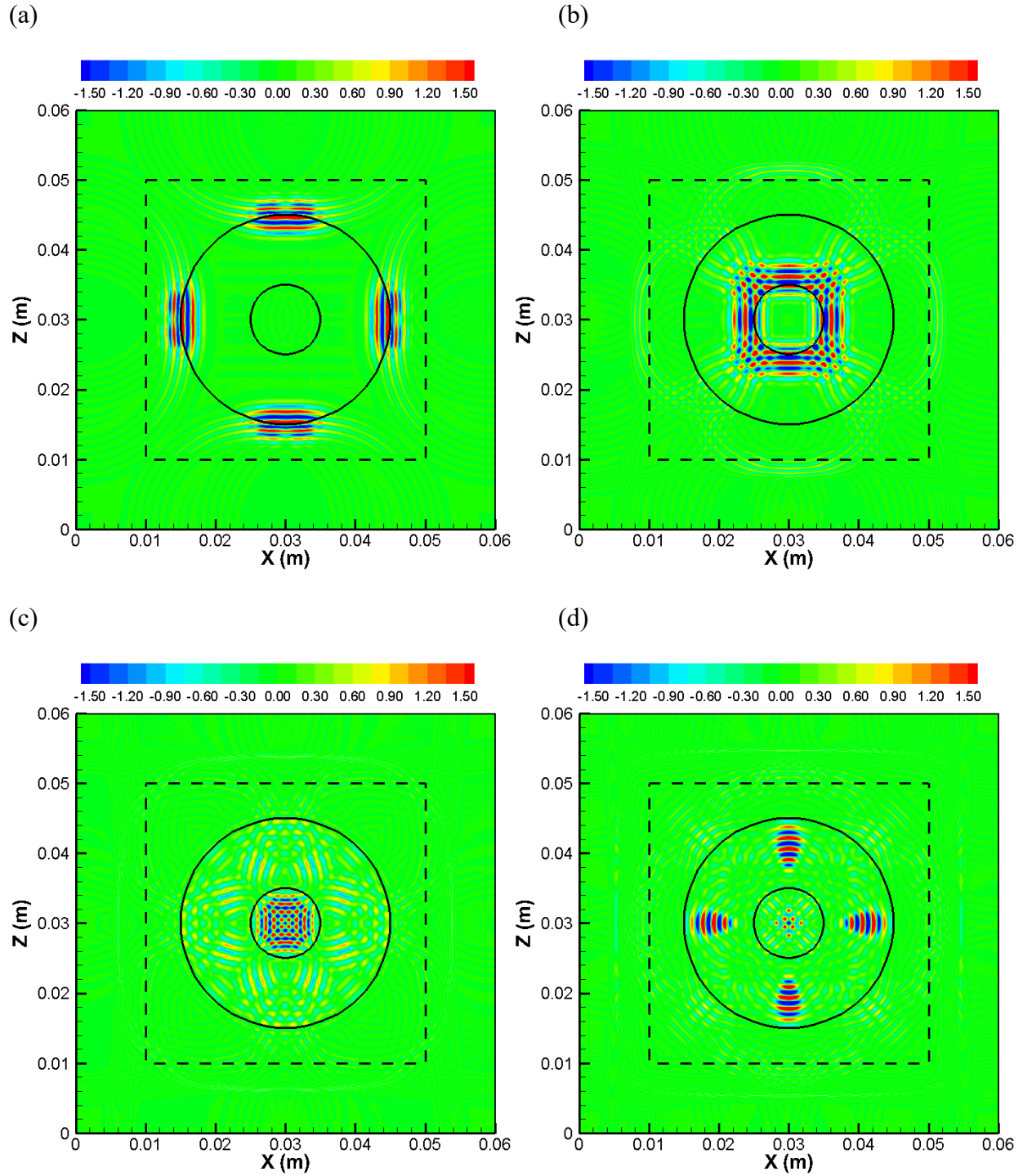
Figure 38. Pressure contours of multiple-source ultrasound propagation at different moments: (a) t = 12.5μs (b) t = 17.5μs (c) t = 22.5μs (d) t = 27.5μs

5.4 Summary

When sinusoidal waves propagate into a lossy medium, they experience dissipation caused by viscosity, heat conductivity, and relaxation process. Therefore, incident acoustic waves are attenuated by those processes, which results in a power-law attenuation in the frequency domain. This phenomenon can be modeled and numerically simulated with the FDTD method. When solving for fractional Laplacian derivatives in the lossy medium acoustic propagation equations, the FCD method is employed [117, 119]. The procedure, which is based on a relatively simple algorithm does not require large memory involve integral transform. The implementation of the FCD combining with the IB method maintains the second-order spatial accuracy.

The numerical simulation results show a gradually reducing pressure level along the wave propagation direction in the lossy medium and agree with the analytical solution of a power attenuation law. The implementation of the immersed-boundary method enables ultrasound propagation around irregular geometries to be simulated with a simple structured Cartesian mesh. Moreover, this method can be used to solve multi-media, multi-source problems. Since the mesh is already designed to resolve very high frequency signals (over 1MHz) for ultrasound propagation problems, the density of the mesh usually enables accurate interpolation near the boundary of the medium geometry unless there are extremely small local features. For very small local geometrical features, we can increase the local mesh resolution to increase the accuracy of the immersed-boundary method. This capability for handling complex geometries with multiple material interfaces overcomes the limitation of the previous work in the area of lossy medium simulation. Furthermore, with the same approach, the method can be readily extended to simulate 3D problems.

Chapter 6.   Vortex Scattering Effects on Acoustic Wave Propagation

6.1 Introduction

The traditional method for studying scattering effect is via direct numerical simulation (DNS). The method solves vortex induced flow field and the acoustic field caused by that. Therefore, it is very expensive and not practical in 3D big domain study. We will directly employ the vortex's flow field solution as background and solve the acoustic field with linearized Euler equations (LEE). In our simulation, we consider the cases in which the wavelength of the incident sound is a few times longer than the characteristic length scale of the vortex to align with the Born approximation. For high-speed vortex flow, the velocity and its gradients are large, and numerical simulation without employing special numerical treatment for the convection terms can often suffer from numerical errors in the regions around the high-speed vortices. We address the problem by using a high order WENO scheme [80-89] to solve the convection-dominant background flow in the time-domain numerical simulation. This scheme not only achieves higher-order accuracy near the high gradient velocity regions, but also maintains a stable and non-oscillatory solution. On the other hand, to save the computational effort for the high-order scheme, the WENO scheme does not need to be applied to the entire computational domain, but only to the regions with high velocity. In this paper, a plane incident wave at a frequency of 85Hz is used to study the scattering effects through vortices.

We study the cases of single stationary vortex with zero or finite circulation first, and verify our linearized simulation with existing literature results from DNS [63]. Then a stationary/moving vortex pair is investigated and also verified with an analytical solution. For 3D vortex flow, we present the study of scattering by an HSV. Finally, we conclude with scaling laws of acoustic scattering by 2D and 3D vortices.

6.2 Numerical method

6.2.1 Governing equations

The linearized Euler equations of acoustic propagation in an idea gas are:

$$\frac{\partial \boldsymbol{u}}{\partial t} + (\boldsymbol{u_{av}} \cdot \nabla)\boldsymbol{u} + (\boldsymbol{u} \cdot \nabla)\boldsymbol{u_{av}} = -\alpha_{av}\nabla p + \alpha\nabla p_{av}, \tag{89}$$

$$\frac{\partial p}{\partial t} + (\boldsymbol{u_{av}} \cdot \nabla)p + (\boldsymbol{u} \cdot \nabla)p_{av} = -\gamma p\nabla \cdot \boldsymbol{u_{av}} - \gamma p_{av}(\nabla \cdot \boldsymbol{u}), \tag{90}$$

Here $u_{av}, p_{av}, \alpha_{av}$ are the time-averaged velocity, pressure, and specific volume, respectively; u, p, α are their acoustic fluctuations. A fifth order WENO scheme is applied in the test region[88, 89]; a second-order finite difference scheme [25] is applied for region close to the boundary.

6.2.2 High Order Upwind Scheme

Due to their ability to accurately calculate the high gradient of velocity and achieve a stable and non-oscillatory numerical scheme, high-order upwind schemes have been widely used to discretize the convection terms of the variables in the direction of their propagation of information in a flow field [88, 89]. To illustrate the implementation of the high-order upwind scheme for the convection terms in the current simulation, we take the one-dimensional convection term as an example:

$$a\frac{\partial u}{\partial t} = a^+u_x^- + a^-u_x^+, \tag{91}$$

where $a^+ = \max(a, 0)$ and $a^- = \min(a, 0)$.

The fifth-order WENO scheme for u_x^- and u_x^+ used in this study is given as:

$$u_x^\pm = w_1^\pm u_x^{1\pm} + w_2^\pm u_x^{2\pm} + w_3^\pm u_x^{3\pm}, \tag{92}$$

where $w_1^\pm, w_2^\pm$ and $w_3^\pm$ are the weight coefficients and can be found in [88]. In addition, $u_x^{1\pm}, u_x^{2\pm}$ and $u_x^{3\pm}$ are three ENO3 stencils defined as:

$$u_x^{1\pm} = \frac{q_1^\pm}{3} - \frac{7q_2^\pm}{6} + \frac{11q_3^\pm}{6}, \tag{93}$$

$$u_x^{2\pm} = -\frac{q_2^\pm}{6} + \frac{5q_3^\pm}{6} + \frac{q_4^\pm}{2}, \tag{94}$$

$$u_x^{3\pm} = \frac{q_3^\pm}{3} + \frac{5q_4^\pm}{6} - \frac{q_5^\pm}{6}, \tag{95}$$

where

$$q_1^- = \frac{u_{i-2,j} - u_{i-3,j}}{\Delta x}, \qquad q_2^- = \frac{u_{i-1,j} - u_{i-2,j}}{\Delta x}, \qquad q_3^- = \frac{u_{i,j} - u_{i-1,j}}{\Delta x},$$

$$q_4^- = \frac{u_{i+1,j} - u_{i,j}}{\Delta x}, \qquad q_5^- = \frac{u_{i+2,j} - u_{i+1,j}}{\Delta x} \tag{96}$$

and

$$q_1^+ = \frac{u_{i+3,j} - u_{i+2,j}}{\Delta x}, \qquad q_2^+ = \frac{u_{i+2,j} - u_{i+1,j}}{\Delta x}, \qquad q_3^+ = \frac{u_{i+1,j} - u_{i,j}}{\Delta x},$$

$$q_4^+ = \frac{u_{i,j} - u_{i-1,j}}{\Delta x}, \qquad q_5^+ = \frac{u_{i-1,j} - u_{i-2,j}}{\Delta x}, \tag{97}$$

In this study, the high-order upwind scheme is applied to the regions around the vortices, and the numerical scheme in [25] is used for solving convection in the remaining region. More details about WENO scheme can be found in [88]. It should be noted that the background velocity field generated by the vortices is assumed to be steady.

6.2.3 Simulation setup

Figure 39 shows a schematic diagram of the configuration in both 2D and 3D simulations. A harmonic continuous plane wave is specified on the left boundary $(y = 0)$. The acoustic waves propagate to the right, interact with the vortex in the middle, and then are dampened in the perfectly matched layers (PML) [92, 120, 122] on the right. To prevent reflection waves, we put PMLs all around test section except the left side.

The incident sinusoidal wave on the left boundary is in the form of $p = sin(\omega_0\, t)$, here the angular frequency $\omega_0 = 2\pi f_0$. When we set the incoming wave frequency f_0 to be 85 Hz and the speed of sound c_0 to be 340 m/s, and vortex core size to be 1 meter, the wavelength λ of 4m is a few times larger than the size of the vortex core, L, selected to be 1, which means the Born approximation is used.

The size of the 2D computation domain is 110m in the y-direction and 160m in the z-direction. The grid size of both Δy and Δz is $0.05m$, the time step is $2.0 \times 10^{-6}s$, and the total simulation time is $0.31s$. The center of the vortex or the vortex pair is located at $(20, 80)m$. Circular-shape receiver arrays centered by vortex center are place at far filed, the distance from each receiver to the center of the array is r.

Figure 39(c) gives the 3D simulation setup. The 3D computational domain is a 19m square box, with the uniform mesh size $\Delta x = 0.02m$. A sinusoid plane wave with $f = 170Hz$ on the left side of the domain $(y = 0m)$ is specified as the incident wave. The PML thick is 1m at all the boundary surfaces except the left side, which is incident wave surface. The HSV with the radius size $L = $ 1m is located at (0, 8.5, 0). Receiver locations centered at the vortex center with radii equals to 2, 4, 6, 8m in the x-y plane $(z = 0m)$ is used to calculate the far-field scattering effects. The simulation time is 0.15s, which allows the plane wave to completely pass the vortex and all the receivers.

(a)

(b)

(c)
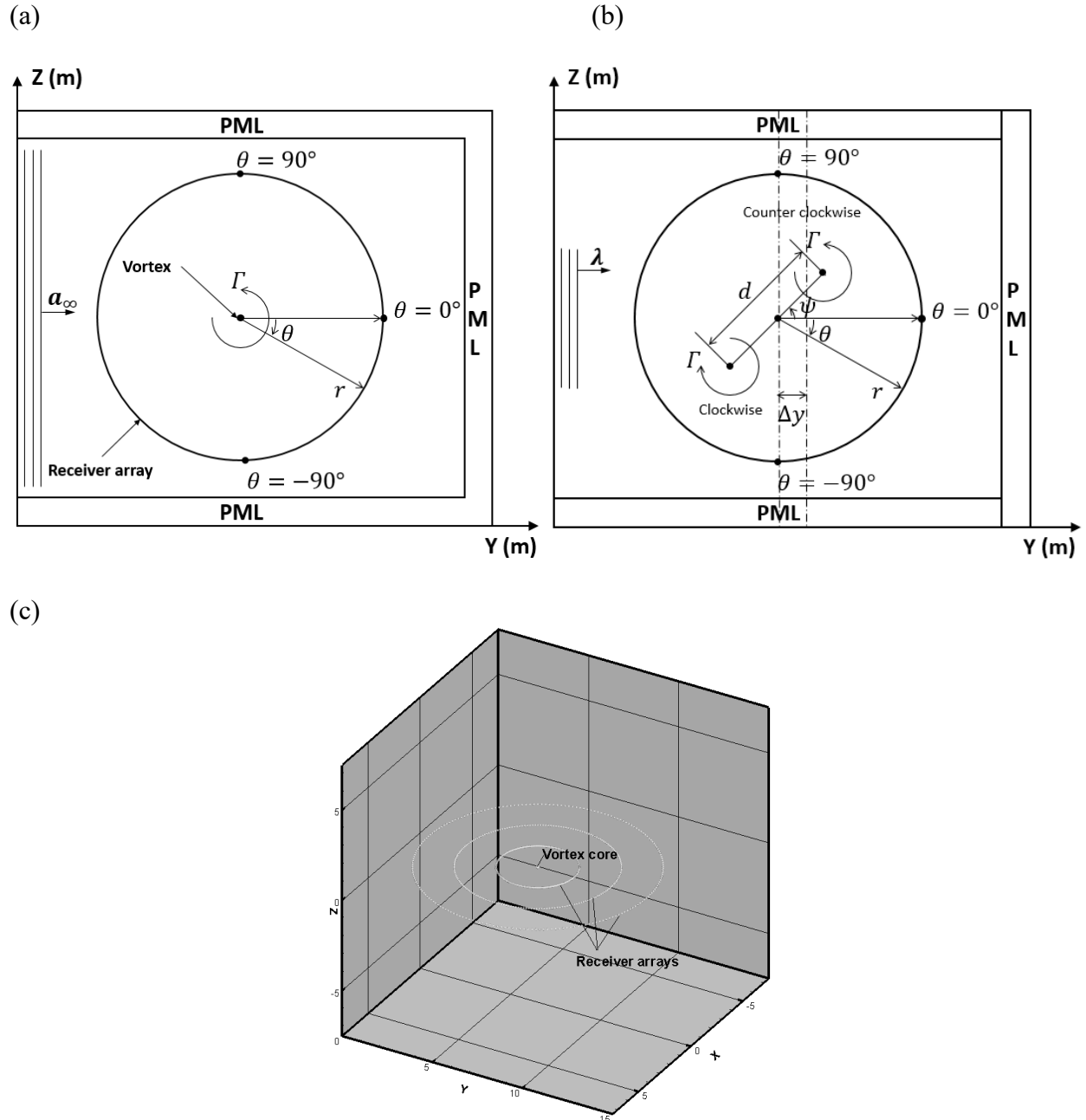
Figure 39. Schematic diagram of (a) a 2D single vortex, (b) a 2D vortex pair, and (c) a 3D HSV.

To study the vortex influence on the acoustic field, a free space simulation (without vortex) is also carried out. Then, the scattering pressure can be calculated as:

$$p_s = p_2 - p_1 \tag{98}$$

where p_s is the scattering pressure, p_1 is the free space pressure, and p_2 is the pressure of the domain with vortex.

6.3 Scaling law in different vortex configurations

6.3.1 Single vortex with finite circulation

For a finite circulation single vortex, the velocity is given by [63]:

$$v_\theta = \frac{\Gamma}{2\pi r}\left(1 - exp\left(-\frac{\alpha r^2}{L^2}\right)\right) \tag{99}$$

where Γ, L and r are the circulation of the vortex, the radius of the vortex core, and the distance

away from the vortex center, respectively; α is a constant selected as 1.256431, so that the

maximum velocity occurs at $r/L = 1$. The definition of the Mach number for a single vortex is:

$$M = \beta\,\frac{\Gamma}{2\pi L c_0} \tag{100}$$

where β is a numerical constant related to the specific distribution of tangential velocity in the

core of the vortex and is 0.7153322.

In order to compare with the literature data, four simulation cases are considered for

sound propagation over a single vortex with the Mach number to be 0.0625, 0.125, 0.25 and 0.5.

The scattering pressure contours at time 0.31s for the four cases are shown in Figure 40 (a)-(d). It

can be observed that the pressure pattern is more symmetric in the lower Mach number cases

about the line of $z = 80$m and most of the scattering effect is in the region between -30° to 30°.

As the Mach number increases, the scattering effect becomes stronger at both the up and down

streams of the vortex. These refractive effects are obviously caused by the background vortex

flow field.
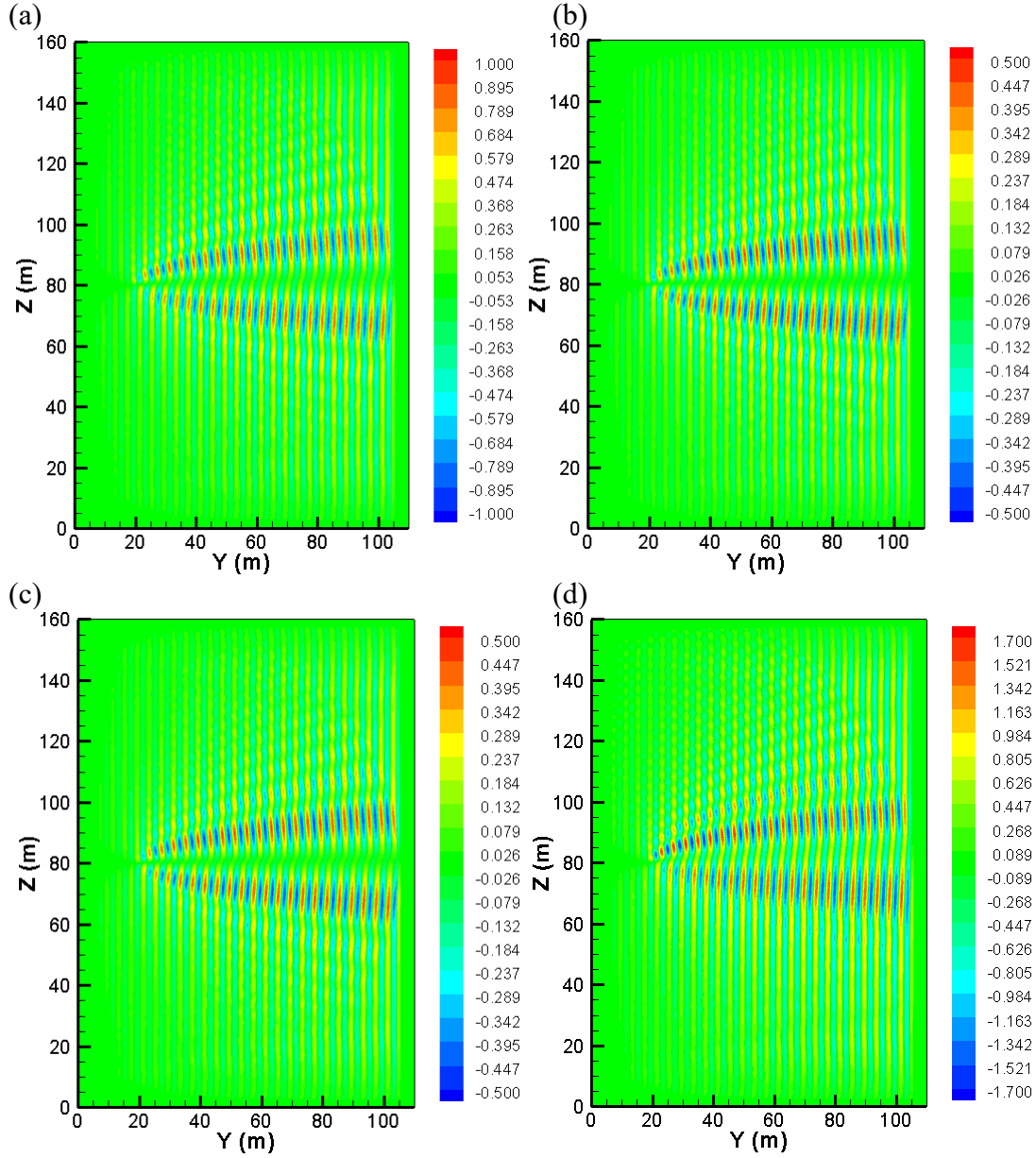
Figure 40. Finite-circulation single vortex pressure fluctuation contours at time 0.31s with different Mach numbers: (a) 0.0625; (b) 0.125; (c) 0.25; (d) 0.5.

The root-mean square sound pressure of the scattering wave, p_{rms} is used to describe the scattering effect of the vortex, which is defined as:

$$p_{rms} = \sqrt{\frac{\int p_s^2 dt}{T}} \qquad (101)$$

The root-mean-square pressure is normalized with the incident wave pressure magnitude (p_{rms}/p_I, p_I=1 is the amplitude of the incident wave), and the results are shown in Figure 41(a)-

(d), along with the DNS simulation results by Colonius et al. (1994). Our numerical results agree

well with the DNS data, except at some points in the case of M=0.5. In spite of these points, the

overall agreement is still very good even at this high Mach number. It is also noticed that the

scattering pressure variation versus angle at the range between 0 and180 degrees is more drastic

than that between -180 and 0 degrees, when the Mach number of the vortex increases, which is

also found in the scattering pressure contours in Figure 40.
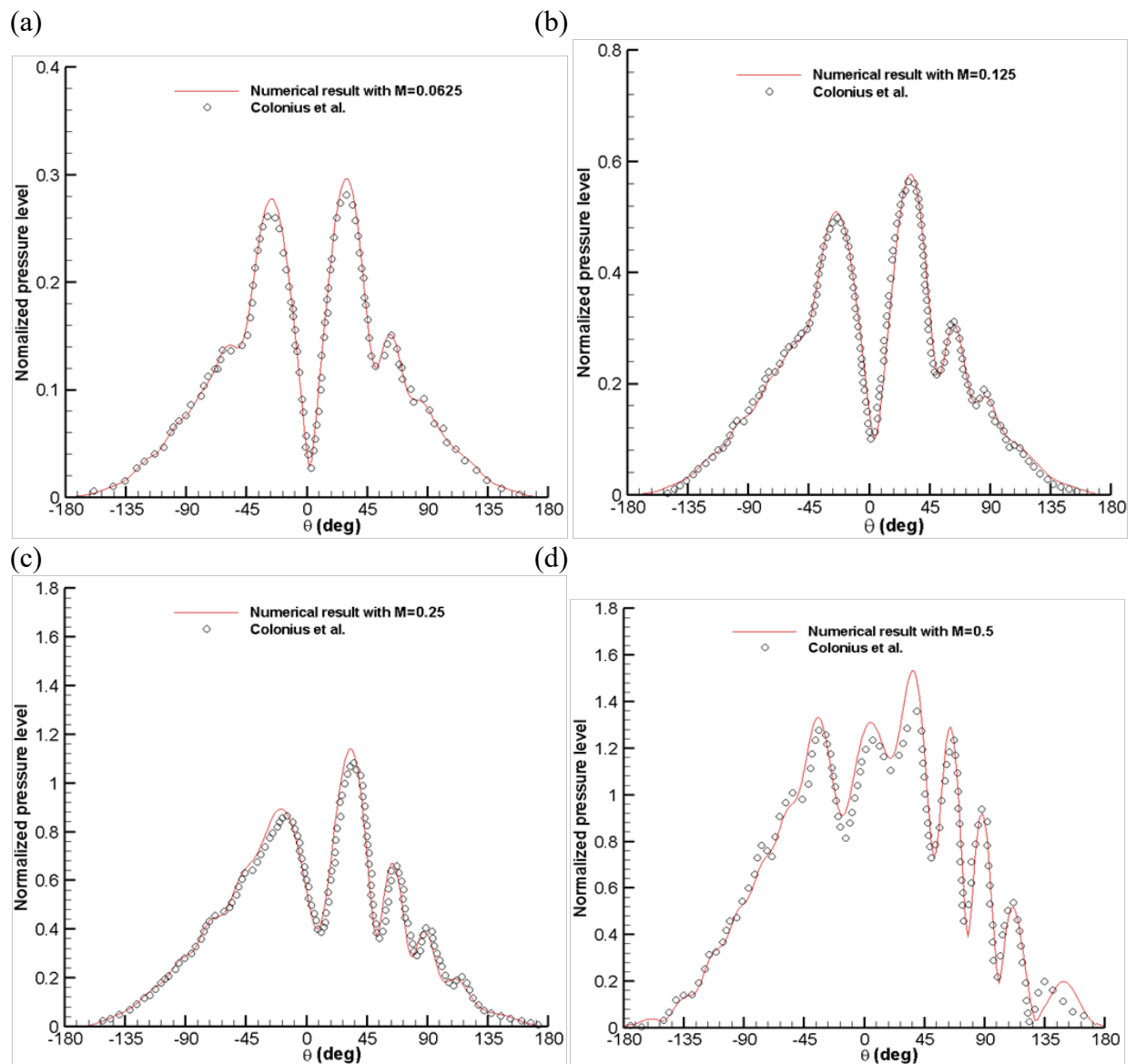
Figure 41. Normalized pressure level with different Mach numbers comparing with Colonius et al. (a) 0.0625 (b) 0.125 (c) 0.25 (d) 0.5.

To illustrate the accuracy of the WENO scheme, we change the grid size from 0.05m to 0.2m. Cases of Mach number 0.25 and 0.5 are tested, and the results are presented in Figure 42. For the case of Mach number 0.25 in Figure 42 (a), it is found that the results from both the second-order and WENO schemes are very close to the fine grid results. However, for the case of the larger Mach number of 0.5 in Figure 42 (b), the curve of the second-order scheme deviates a lot from that of the fine grid case, while the result of the WENO scheme still agrees well with the result of the fine grid. This is an evidence that the WENO scheme maintains very good accuracy with the vortex dominant flow in the background even at a very high Mach number.

(a)   (b)
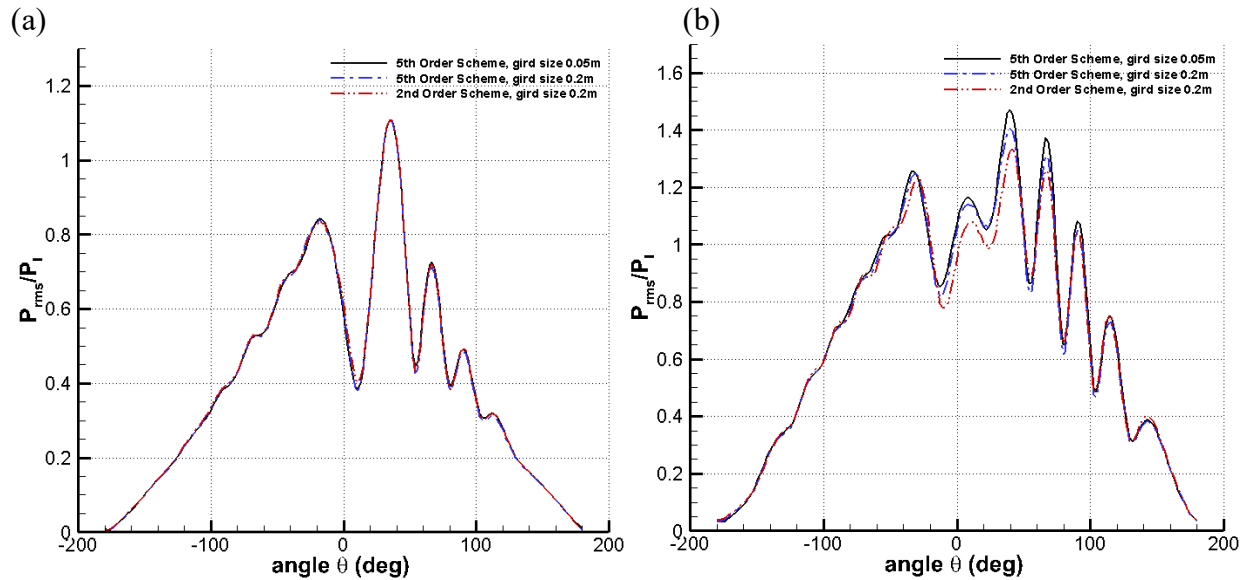
Figure 42.Normalized pressure level with different schemes at different Mach number (a) 0.25 (b) 0.5

According to the low-frequency theories in [60], the root-mean-square sound pressure p_{rms} in the far filed should scale as:

$$p_{rms} \sim p_I \varepsilon (\lambda/r)^{1/2} \qquad (102)$$

where,

$$\varepsilon = \Gamma/(a_\infty \lambda) \qquad (103)$$

The root-mean-square sound pressure scaled by the right-hand side of Eq. (102) is given in Figure 43(a) for each different Mach number. When the ratio of r/λ is kept a constant of 2.5 and the Mach number decreases, the peak scattering of normalized p_{rms} appears to scale with ε until M=0.25 ($\varepsilon = 0.55$). Once the Mach number increases to 0.5, the scattering peaks that occur at the lower Math numbers are no longer significant, because of the high Mach number effect.

On the other hand, when we hold ε as a constant 0.14 ($M = 0.0625$), the normalized p_{rms} are plotted for various values of r/λ in Figure 43 (b). The peak scattering appears not scale with $(r/\lambda)^{\frac{1}{2}}$. This is due to the refraction effect of the slowly decaying vortex flow field [65], which is at the rate of $1/r$, as indicated in Eq. (99) The results again agree with the single vortex scattering effect in the DNS by [63].

(a)   (b)
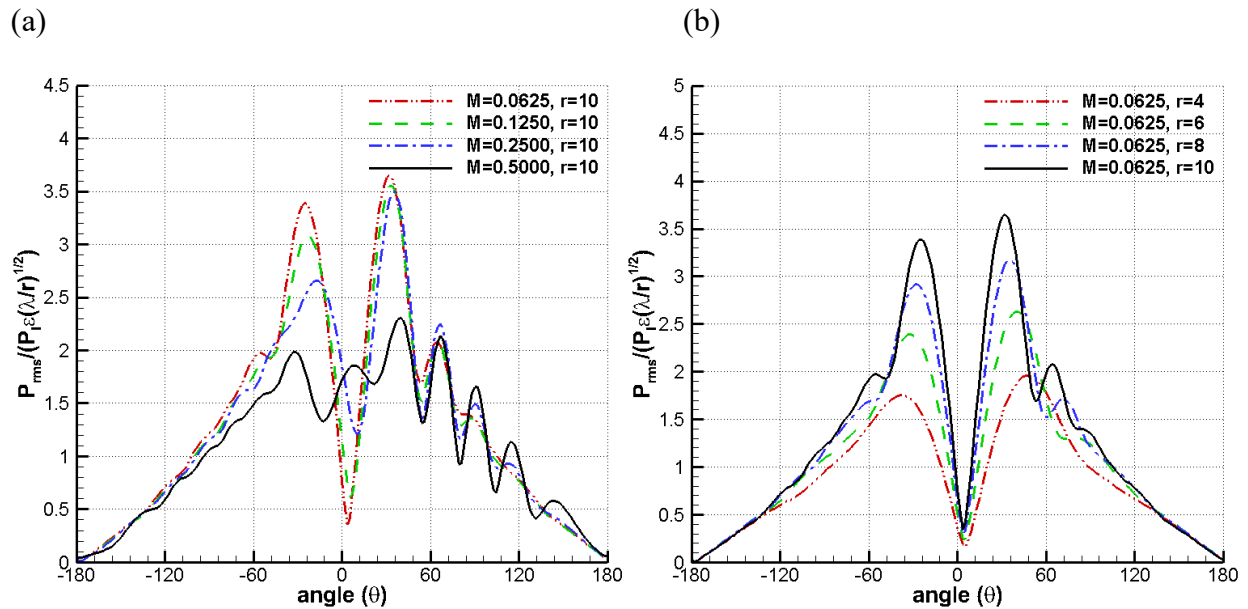
Figure 43. Normalized P_{rms} when (a) receiver distance $r/\lambda = 2.5$, *with varying Mach number* (b) Mach number M = 0.0625 ($\varepsilon = 0.14$), *with varying receiver distance*

6.3.2 Single vortex with zero circulation

With the above slow-decaying single vortex case, it is of interest to study a zero-circulation vortex flow field for fast-decaying refraction effect from the mean flow field. According to [63], the velocity of a zero-circulation vortex in polar coordinate can be expressed as:

$$v_\theta = M \cdot a_\infty \cdot \frac{r}{L} \exp\left[\frac{1}{2}(1 - r^2)\right] \tag{104}$$

In this case, the velocity decays exponentially, much faster than the previous finite circulation vortex expressed in Eq. (99). With the same simulation setup, the resultant scattering pressure contours are given in Figure 44. Similar to the finite-circulation single vortex, in the lower Mach-number cases, Figure 44 (a)-(c), the scattering pattern appears to be symmetric about $z = 80m$, but the scattering area is bigger, between $-45°$ to $45°$. The higher Mach number cases in Figure 44 start to show asymmetry, which is the same as the previous finite- circulation single vortex case. The difference is, comparing with Figure 40, we see fast-decaying far-field refraction effect in Figure 44.

(a)

(b)

(c)

(d)
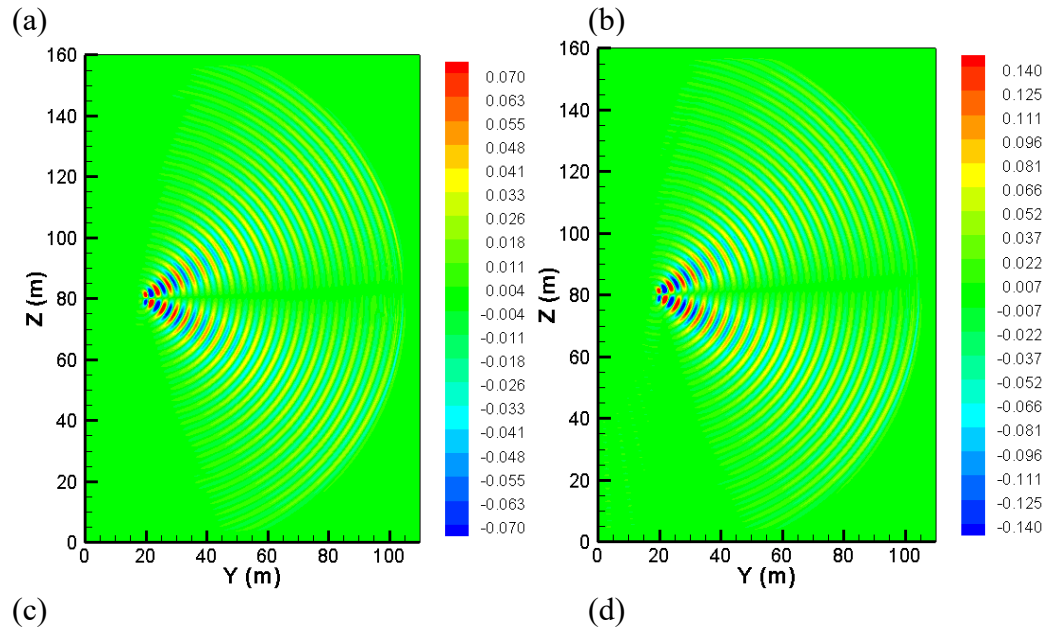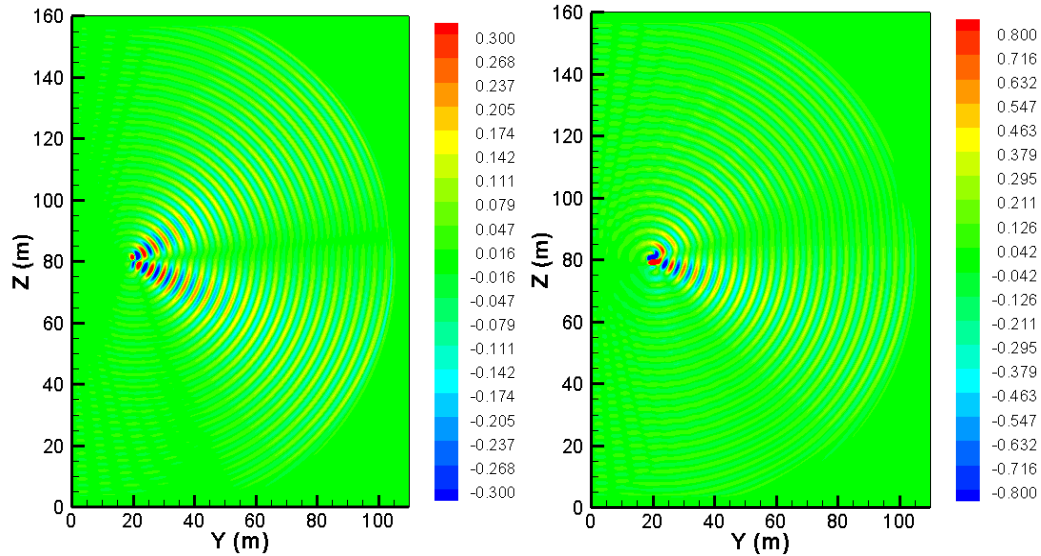
Figure 44. Zero-circulation single vortex scattering pressure contours at time 0.31s at different Mach numbers: (a) 0.0625; (b) 0.125; (c) 0.25; (d) 0.5.

Figure 45 gives the comparison with the DNS results by Clonius et al. (1994) of normalized scattering pressure (p_{rms}/p_I) at $M = 0.125$ and the receiver at $r/\lambda = 2$, showing the our linearized simulation matches the DNS results very well in the zero-circulation single vortex case.
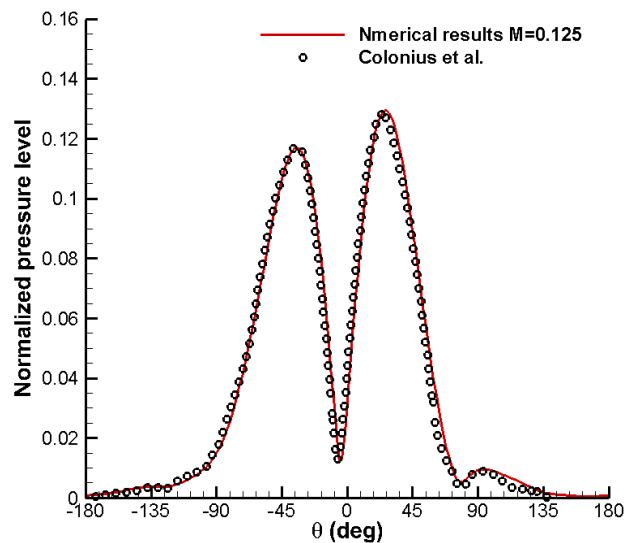
Figure 45. Normalized pressure level with different Mach numbers comparing with Colonius et al. M = 0.125, $r/\lambda = 2$

In Figure 45, we normalize the root-mean-square pressure with RHS of (100), and plot

a) $r/\lambda = 2.5$, with varying ε (different Mach numbers); and b) $\varepsilon = 0.14$ (Mach number 0.0625),

with varying r/λ. In both Figure 46(a) and (b), the scaled p_{rms} curves collapse at lower Mach numbers and far-field, particularly near the peaks. This gives the evidence that the scaling law appears to hold for peak scattering at low Mach number in the far field, which is also consistent with the low-frequency theories in [60].

(a)   (b)
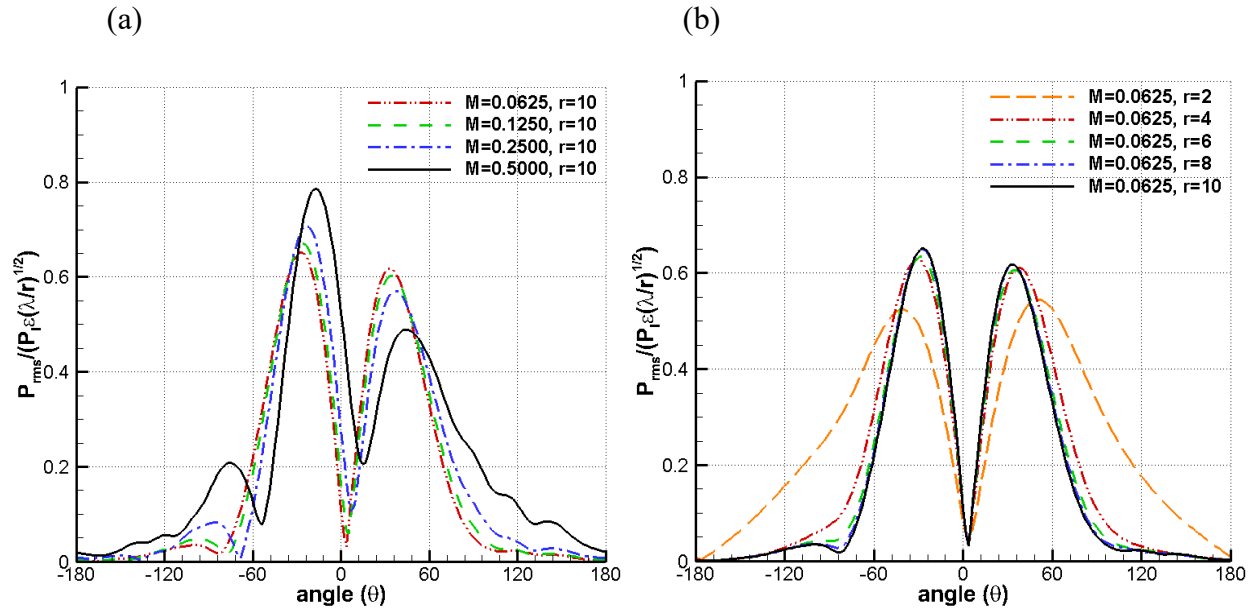
Figure 46. Normalized P_{rms} when (a) receiver distance r/λ=2.5, (b) Mach number M = 0.0625 (ε=0.14).

6.3.3 Stationary vortex pair

The total circulation of a vortex pair is zero. However, due to a different flow field from a single vortex with zero circulation, the acoustic scattering effect can be different. To represent the vortex pair, two counter-rotating single finite-circulation vortices as expressed in Eq. (99) is used. The distance, d, shown in Figure 39 (b), is the space between the two vortex centers. The distance between the receiver and the center of the vortex pair, r, starts from 50m. Different orientations of vortex pair are represented as different angles ψ in Figure 39 (b), and the coordinates of the two vortex centers in a vortex pair with ψ =90° are (20, 79) and (20, 81),

respectively. Because the purpose of this study is to investigate the scaling laws of the vortex

scattering effect, we focus on the vortex pair aligned with the incident wave only, i.e., ψ =90º,

although we simulated vortex pairs with different orientation angles.

With ψ =90º, scattering pressure contours are given in Figure 47. Because the far-filed

velocity decays at $1/r^2$, the far-field scattering effect is in between the finite- circulation vortex

whose velocity decays at $1/r$, and the zero-circulation vortex whose velocity decays

exponentially with the distance. Therefore, we observe insignificant refraction effects from the

mean flow at the far field in Figure 47.
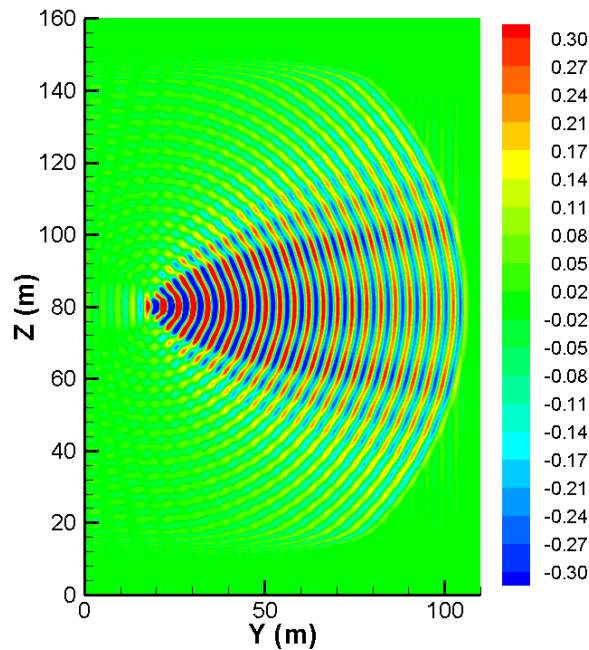
Figure 47. Scattering pressure contours for the stationary vortex pair cases at time 0.31s with Mach number 0.25 for
ψ =90°

The normalized pressure levels for $\psi = 90^o$ are given in Figure 48. It is seen that the

main peak is located at $\theta = 0°$. Different from the single vortex cases, the curve of normalized

pressure level is symmetric with respect to $\theta = 0°$ in the case of vortex pair at $\psi = 90°$. This is

because the flow field is symmetric in this case.
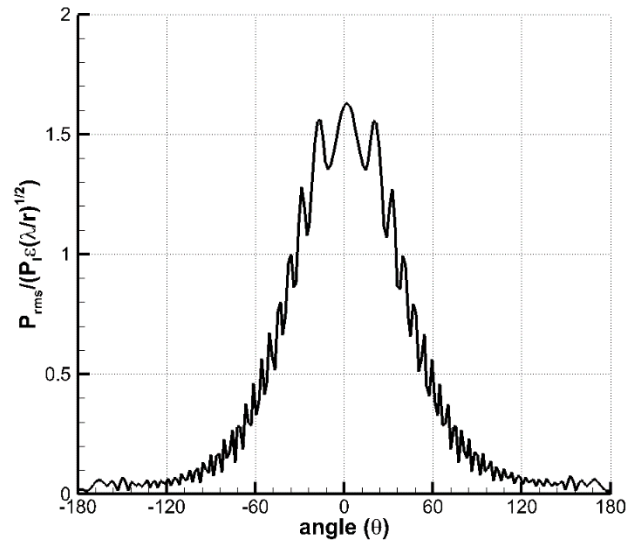
Figure 48. Normalized pressure levels at t=0.31s, r=10m and M=0.25 with $\psi = 90°$

To study the scaling law of the scattering effect, we plot the normalized p_{rms} in Figure 49. At the same receiver location ($r/\lambda = 2.5$), the low Mach number cases tend to scale with ε, but this does not apply for the high Mach number cases in Figure 49(a). On the other hand, when Mach number is set to be 0.0625, i.e. ε is a constant of 0.14, by changing the receiver distance r, the curves appear to scale with $(\lambda/r)^{\frac{1}{2}}$ in Figure 49(b). Therefore, the scattering effect of a stationary vortex pair agrees with the low-frequency theory when the Mach number is low.
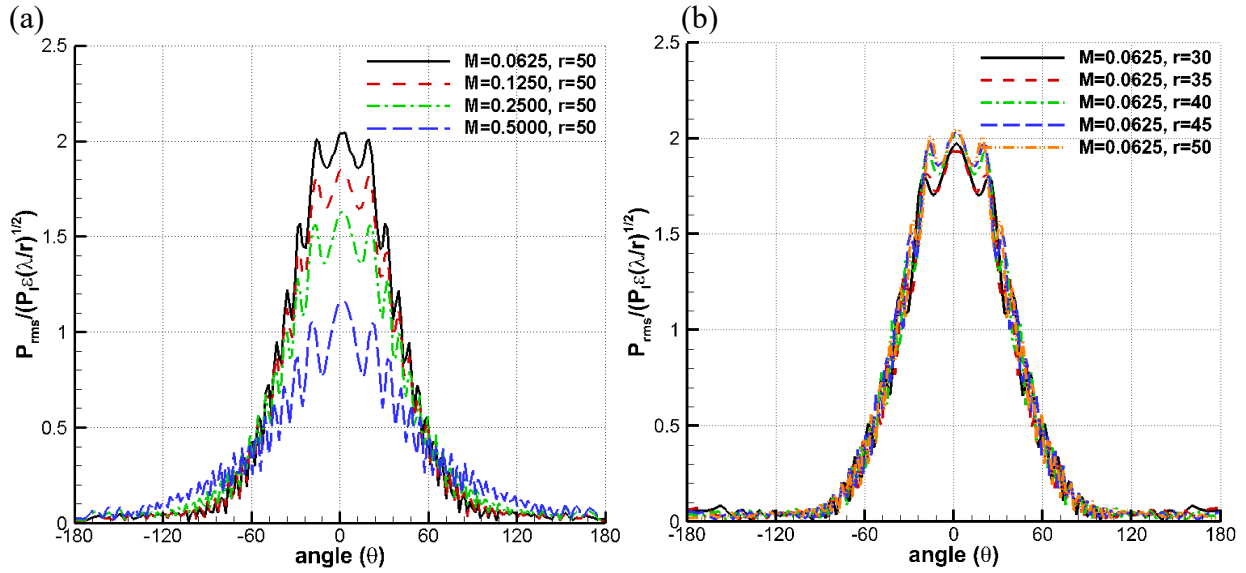
Figure 49. Normalized P_{rms} when (a) receiver distance is r/λ=2.5 at different Mach numbers of 0.0625, 0.125, 0.25, and 0.5, (b) Mach number M = 0.0625 (ε=0.14) at different receiver locations r/λ = 7.5, 8.75, 10, 11.25, and 12.5

Since the vortex pair spacing, d, is another variable of a vortex pair, we verify the

scattering effect with a larger d/L value, d/L=4, and plot the normalized p_{rms} in Figure 50 for

various far-field locations, r/λ, at the same Mach number 0.0625 ($\varepsilon = 0.14$). Figure 50 shows

that p_{rms} scales well with the distance at $1/(r/\lambda)^{1/2}$.
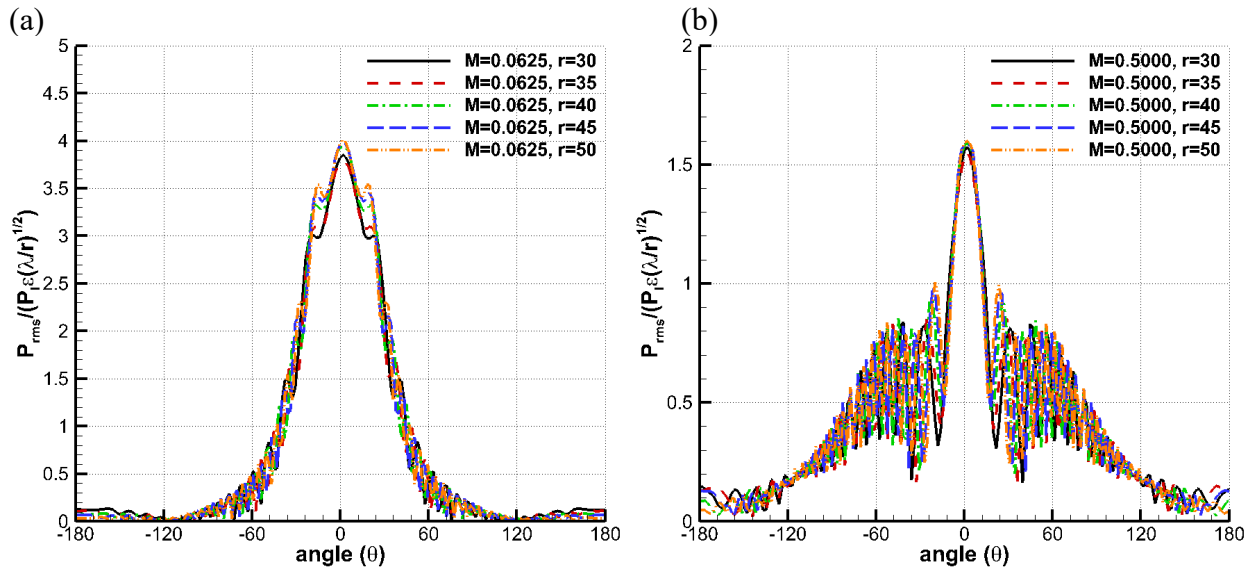
Figure 50. Normalized P_{rms} with different r/λ at d/L=4 and M=0.0625

6.3.4 Moving vortex pair

When scattering phenomenon occurs, it will lead to a spatial and spectral redistribution of acoustic energy. Once convection of the vortex is considered the distribution of acoustic energy is of interest to study. Clair and Gabard conducted investigations of a single vortex convected in a uniformed mean flow [69, 70]. They let a vortex move perpendicular to the direction of source wave propagation. The 'haystacking' spectral pattern in frequency domain was able to be observed from their simulations. Our study here will force on the spatial distribution of a vortex pair and convection influence to the Mach number and distance scaling laws.

When a vortex pair moves at the self-induced translational velocity V, the velocity can be found as:

$$V = \Gamma/2\pi d \tag{105}$$

The direction of the vortex pair motion is the same as the plane wave propagation when $\psi = 90º$. Vortex motion can possibly influence the far field velocity and scattering effects. For the moving vortex pair case, we keep all the vortex pair parameters the same as the stationary vortex simulation. To get a better far field results, we shift the vortex pair center and the receiver circle center to $(60, 65)$, and the far-field receiver location is changed to $r = 50m$, in order to ensure that the moving vortex pair is contained inside the receiver circle during the simulation. We initialized the simulation with the stationary vortex pair until the plane waves passed all the receivers. After the vortex pair starts to move, we let it move along the plane wave propagation direction with its self-induced velocity for $5m$. The simulation is conducted with $\psi = 90°$, $d/L = 2$ and M = 0.0625, 0.125, 0.25 and 0.5.

Pressure contours of acoustic scattering when the vortex pair starts to move and after it moves for 5m are given in Figure 51 for the lowest and highest Mach numbers. The higher Mach

number case has stronger sound scattering effects. According to Eq. (105), the moving vortex pair with a higher Mach number has a higher moving velocity.
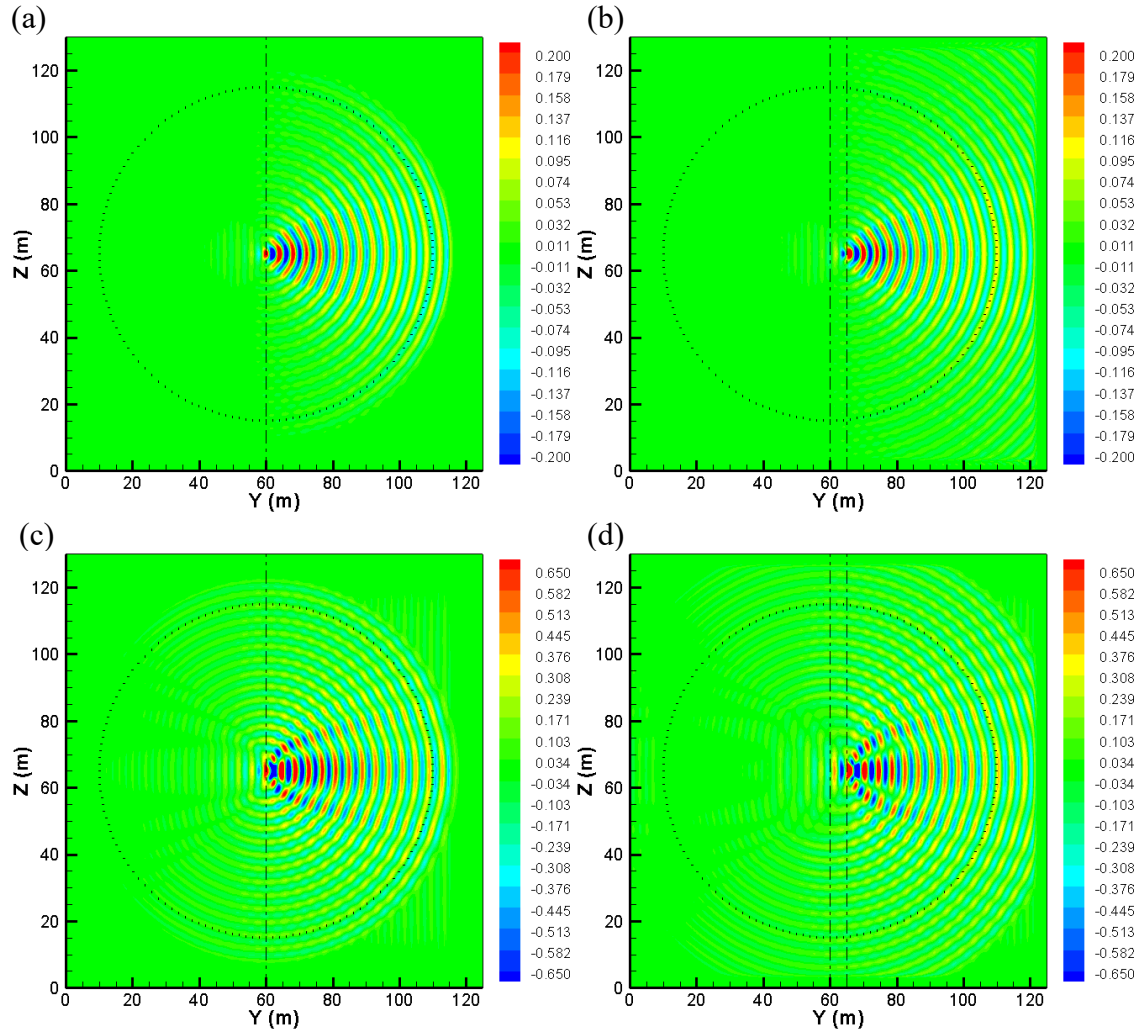
Figure 51.Scattering pressure contours for the vortex pair at the initial position (a) M = 0.0625, (c) M = 0.5; and after moving 5m: (b) M = 0.0625, (d) M = 0.5

To verify our simulation results, the simulated acoustic pressure with $\psi = 90°$ is compared with the analytical solution in [123]. For the analytical solution, the acoustic potential and pressure of the incident plane wave is given by:

$$\phi_I = p_I \exp[i(k_0 y - \omega_0 t)] \tag{106}$$

where k_0 is the wave number defined as $2\pi/\lambda$. The scattered pressure at location (y, z) is given as:

$$p_s = \exp\left(\frac{3i}{4}\pi\right) 2\rho\omega_0 p_I M d\sqrt{2\pi k_0}\; \sin\left[k_0 d\left(\frac{z}{\sqrt{\left(y - \frac{\Gamma}{4\pi d}t\right)^2 + z^2}} - \sin\psi\right)\right]$$

$$\times \frac{\left[z\cos\psi - \left(y - \frac{\Gamma}{4\pi d}t\right)\sin\psi\right]\left[\left(y - \frac{\Gamma}{4\pi d}t\right)\cos\psi + z\sin\psi\right]}{\left[\left(y - \frac{\Gamma}{4\pi d}t\right)^2 + z^2\right]^{3/4}\left[\left(y - \frac{\Gamma}{4\pi d}t\right)\cos\psi + z\sin\psi - \sqrt{\left(y - \frac{\Gamma}{4\pi d}t\right)^2 + z^2}\right]} \quad (107)$$

$$\times \exp\left[i(1 - M\cos\psi)\left(k_0\sqrt{\left(y - \frac{\Gamma}{4\pi d}t\right)^2 + z^2} - \omega_0 t\right)\right]$$

The analytical solution presented in [123] is only applicable for low Mach number steady motion of the vortex pair. After the vortex pair moves 5m ($t = 0.33s$) with at the case of $M = 0.0625$, the simulated scattering acoustic pressure is compared with the analytical solution in Eq. (107) given in Figure 52. We can see that the numerical results have a very good agreement with the analytical solution.
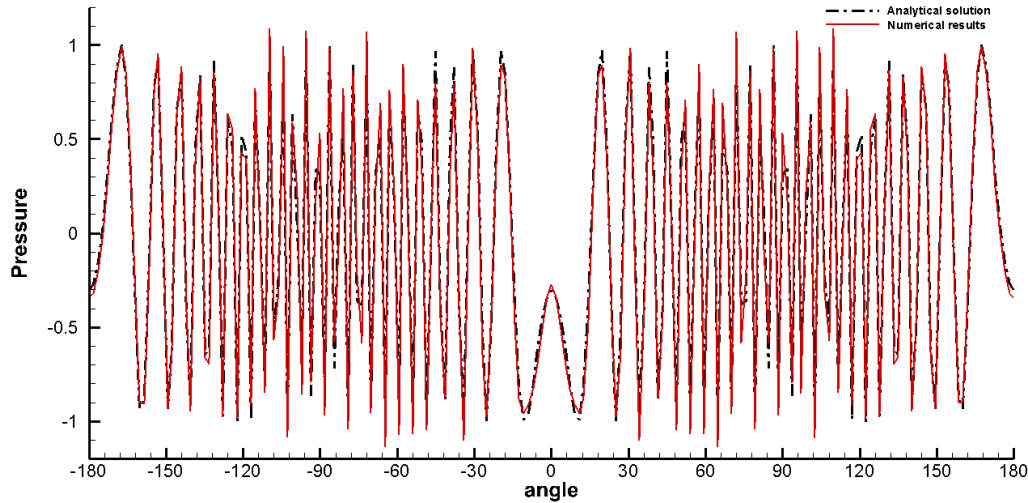
Figure 52. Scattering pressure of moving vortex pair when M=0.0625 in comparison with analytical solutions when vortex moved for 5m (t=0.33s)

Figure 53 gives the normalized pressure level of the moving vortex pair cases in comparison with the stationary vortex pair cases. When the Mach number is lower, the two curves are very close due to the low self-induced velocity. As the Mach number increases, the

two curves gradually become apart from each other, especially at the forward scattering direction

($\theta = 0°$). We can also find that the scattering effect at the forward scattering direction is

gradually reduced with the Mach number increasing. Therefore, the motion of the vortex pair

does influence the scattering pressures.

(a)   (b)
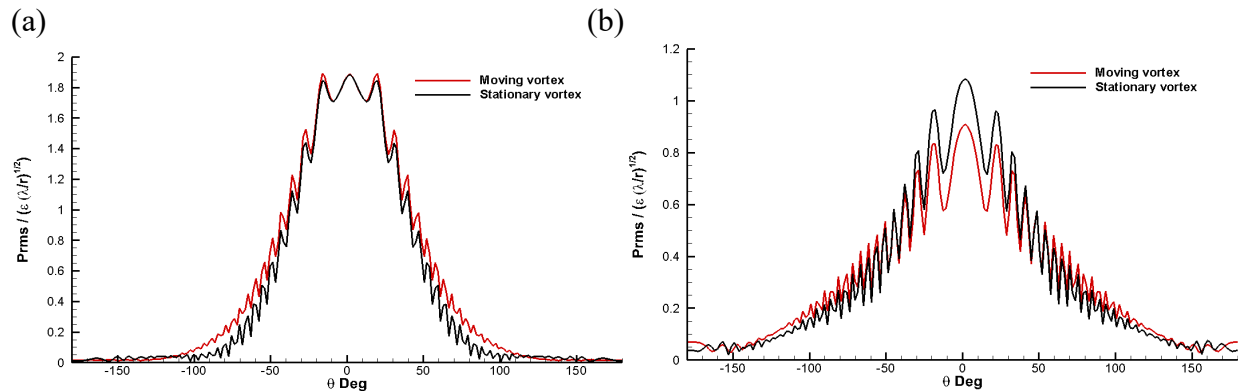
Figure 53. Normalized scattered pressure levels of a moving vortex pair in comparison with those of a stationary vortex pair at r/lamda12.5: (a) M=0.0625; (b) M=0.5.

To study the influence of the vortex motion on the scaling law, we plot the normalized

p_{rms} profiles in Figure 54. The normalized p_{rms} curves show that the curves still scale well with

the receiver distance r/λ in both low and high Mach number conditions.

(a)   (b)
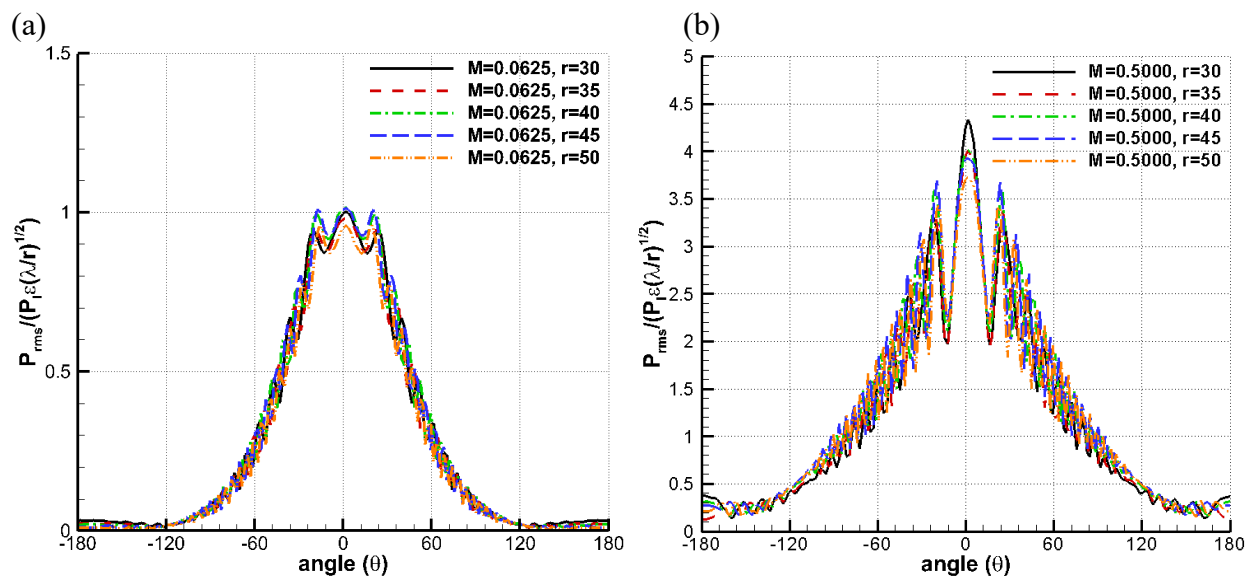
Figure 54. Normalized $\boldsymbol{P_{rms}}$ after vortex pair moves 5m at a) M=0.0625, b) M=0.5

6.3.5 3D Hill's spherical vortex (HSV)

When we extend our study to three-dimensional vortices, Hill's spherical vortex (HSV) is a good example due to its simple axisymmetric analytical solution. Consider a HSV moving in a medium that is at rest at infinity, its stream function can be found[64]:

$$
\psi_0(r, \theta) =
\begin{cases}
-\dfrac{1}{4} U \left(5 - 3\dfrac{r^2}{L^2} \right) r^2 \sin^2 \theta & (r < L) \\[2ex]
-\dfrac{1}{2} U \left(\dfrac{L^3}{r^3} \right) r^2 \sin^2 \theta & (r > L)
\end{cases}
\tag{108}
$$

Here r is the distance to the vortex center, θ is the polar angle. It is necessary to transform Eq. (108) into the Cartesian coordinates for numerical computation, and the resultant velocity field is:

$$
\begin{cases}
U_{av} = -\dfrac{3}{2} U \dfrac{yx}{L^2} \\[2ex]
V_{av} = -\dfrac{5}{2} U + 3U \dfrac{x^2 + z^2}{L^2} + \dfrac{3}{2} U \dfrac{y^2}{L^2} \\[2ex]
W_{av} = -\dfrac{3}{2} U \dfrac{yz}{L^2}
\end{cases}
(r < L),
\qquad
\begin{cases}
U_{av} = -\dfrac{3}{2} U \dfrac{L^3 yx}{(x^2 + y^2 + z^2)^{\frac{5}{2}}} \\[2ex]
V_{av} = -U \dfrac{L^3}{(x^2 + y^2 + z^2)^{\frac{3}{2}}} + \dfrac{3}{2} U \dfrac{L^3(x^2 + z^2)}{(x^2 + y^2 + z^2)^{\frac{5}{2}}} \\[2ex]
W_{av} = -\dfrac{3}{2} U \dfrac{L^3 yz}{(x^2 + y^2 + z^2)^{\frac{5}{2}}}
\end{cases}
(r > L)
\tag{109}
$$

This velocity field obviously shows a decay rate of $1/r^3$.

Figure 55 shows vorticity contours and streamlines of a HSV with Mach number equal to 0.25 and L=1.
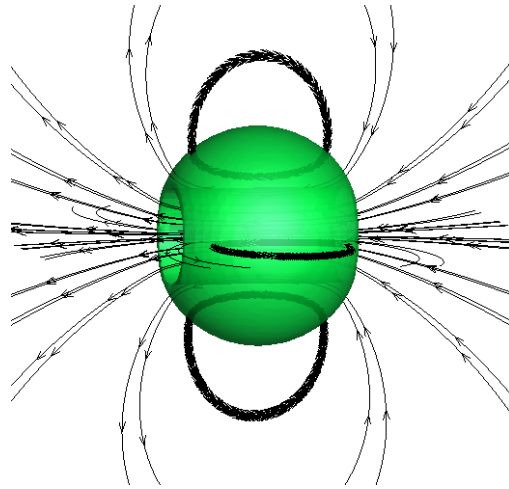
Figure 55. Vorticity magnitude isosurface and streamlines of a HSV with M=0.25, L=1

Scattering pressure contours are given in Figure 56, with M = 0.25. The scattering

pressure pattern in the x-y and y-z planes are the same because of the axisymmetric vortex flow.

The fast scattering pressure decay in the far-field also shows, because of $1/r^3$ decay of the

induced velocity due to the HSV in the far field.
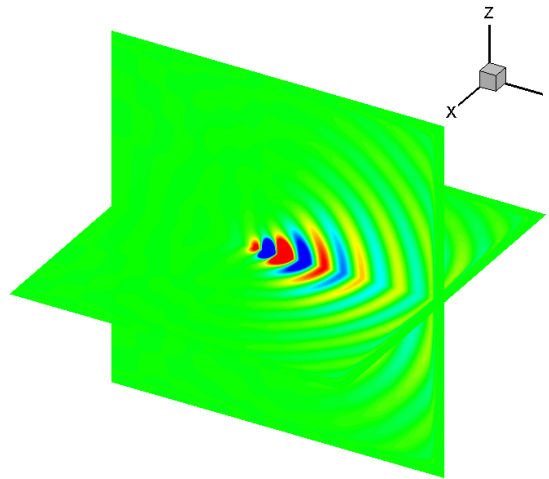
Figure 56. 3D scattering pressure field sections for M=0.25

Normalized P_{rms} scaled with L/r is given in Figure 57. At a fixed Mach number of 0.25,

the peaks of three curves scale very well in Figure 57(a), which confirms that P_{rms} scales with

(λ/r) in 3D versus $(\lambda/r)^{1/2}$ in 2D. The results also mean the acoustic scattering decay is much

faster in 3D than in 2D, which follows the sound pressure - distance relation in 3D and agrees

with the study in [64]. At a fixed receiver distance (λ/r), the three curves of scaled P_{rms} at three different Mach numbers do not scale well at the high Mach number, similar to the 2D cases.

(a)   (b)
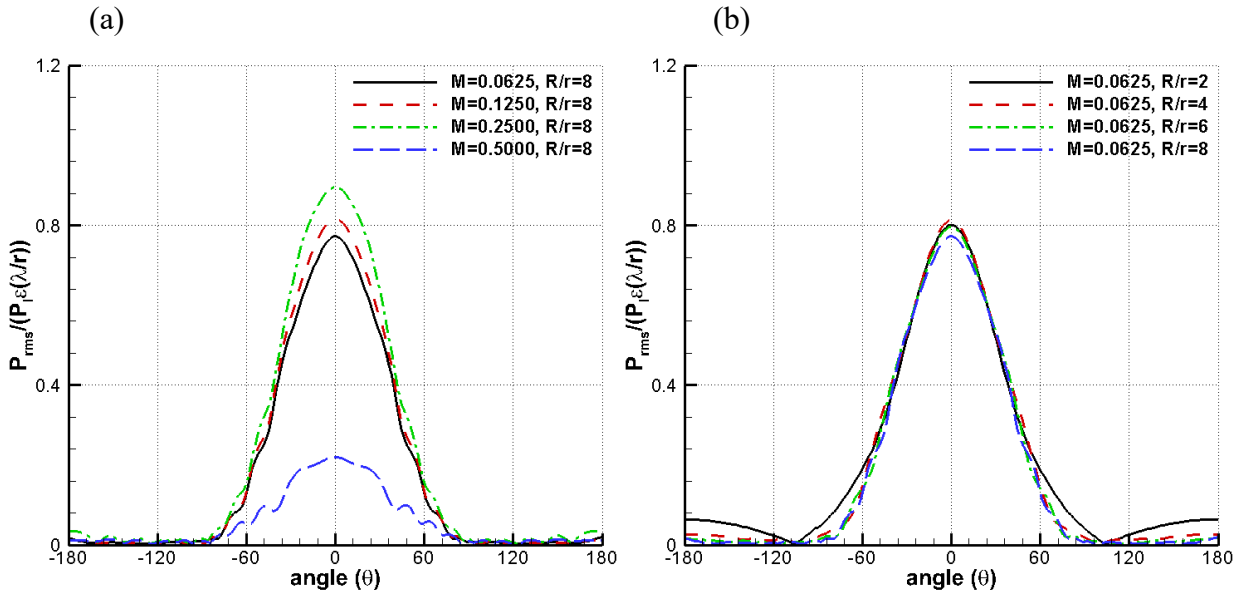
Figure 57.Normalized $\boldsymbol{P_{rms}}$ at constant a) M =0.25, b) r/λ =1.6

6.4 Summary

Propagation of plane waves through vortices in both 2D and 3D is studied. To accommodate the high convective velocity resulting from the background vortex flow, a fifth-order WENO scheme implemented for the time-domain LEE is applied. The results of the single vortex, both with finite circulation and zero circulation, have a good agreement with the full compressible Navier-Stokes simulation in the literature. The results show that, for a single vortex with finite circulation, the scaling law of vortex scattering decay with distance at the rate of $1/r^{\frac{1}{2}}$ is not valid, because of the slow decay of the vortex flow velocity field at the rate of $1/r$ that cannot be considered a compact scattering source. On the other hand, the scaling law of proportionality to the vortex Mach number is only valid for small Mach number vortex flow. However, the zero-circulation vortex is a compact scattering source and the scaling law with the distance follows

the decay rate of $(\lambda/r)^{\frac{1}{2}}$ very well in the far field. In the cases of both stationary and moving vortex pairs, the scaling laws of distance and Mach number seem to apply under the low Mach number flow condition. This is because the vortex velocity field of the vortex pairs decays faster than a single finite circulation vortex, at the rate of $1/r^2$. Similar results are also found in the 3D HSV scattering study. The scaling distance effect in 3D changes from $(\lambda/r)^{1/2}$ to (λ/r), and the velocity decay rate for the HSV is $1/r^3$ The decay rates at the far field vortex flow of $1/r^2$ for a 2D scattering source and of $1/r^3$ for a 3D scattering source are both considered compact sources, and therefore the acoustic scaling laws of far-field distance and the Mach number are valid. This means, the scaling law for distance is applicable for compact scattering sources, and the scaling law for Mach number proportionality is valid for both compact and non-compact scattering sources at low Mach numbers.

Chapter 7.   Conclusion

The conclusions for each section have been summarized previously. In this chapter, the

overall achievement of this dissertation is illustrated in Figure 58.
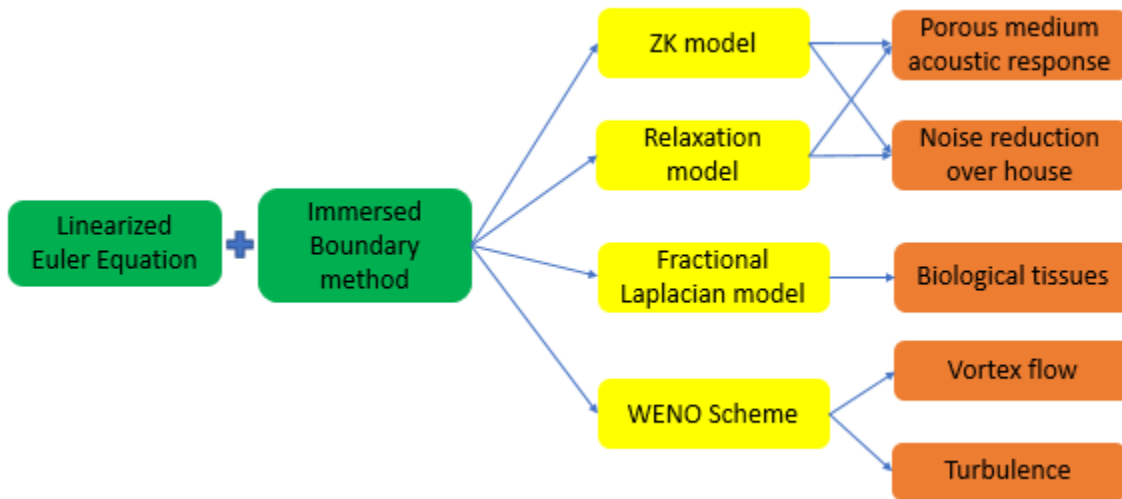
Figure 58 Summary of the dissertation

The FDTD simulation along with the IB method has been performed in coupling with

other numerical models and techniques. The following conclusions are reached:

- The ZK model predictions compare well with the ANSI model results under the condition

  of high flow resistivity. When the ground roughness is introduced, the ANSI model

  predictions are unable to capture the frequency shift due to the ground height variation.

- The frequency-dependent porous material models, e.g. the TDBC and WRX models, are

  implemented by solving the convolution operation with recursive algorithms such as

  PCRC/PLRC. The simulation results match the analytical results and show better

  predictions than those from the frequency-independent porous material model (ZK

  model) under the low flow-resistivity condition in the high-frequency range.

- The simulation results of the original WRX model present mismatch with physical measurements due to the modeled relaxation function. A new approach has been proposed which utilizes the measurement results to construct a relaxation function that fits the measured material. The new relaxation function improves the prediction of the original frequency-dependent porous-medium model significantly.

- A fitting method has been used to represent the material properties of the exterior wall, interior wall, and glass window of a building. The approach simplifies the vibration effects of the wall/glass materials with a simple porous material layer. By matching the simulated indoor-outdoor noise reduction with the measurement results, the material properties of the porous-medium layer can be found. With the identified material properties, a combination of frequency-dependent and frequency-independent material models coupled with the immersed-boundary method are used to simulate the noise reduction of a house near a noise source.

- A fractional Laplacian model is used to simulation the frequency-domain power attenuation law of a biological lossy tissue. The fractional Laplacian terms are solved with the FCD method. The procedure does not require large memory nor need to use integral transform, which is a relatively simple algorithm. The implementation of the FCD method along with the IB method can resolve complicate geometries with a simple structured Cartesian mesh and still maintain a second-order spatial accuracy.

- Sound propagation over vortices is also investigated. The scattering of plane sound waves by 2D and 3D vortices is studied by solving the finite-difference time-domain linearized Euler equations. Different from the DNS, the existing vortex flow field is employed as a background flow. The simulation results of single finite-circulation vortex and zero-

circulation vortex reach a good agreement with the literature results. When applying the same method to a vortex pair, the distance scaling effect and Mach-number scaling effect can be clearly observed. After extending the study to a 3D HSV, the distance scaling effect is still clear.

The following topics are listed for suggested future work:

- Implement a higher-order scheme with low dissipation and dispersion to increase the accuracy as well as to reduce the computational cost.

- Apply the auxiliary differential equation method (ADE) in 3D convolution calculation to increase the accuracy and save memory.

- Extend the current solver from Linearized Euler Equation (LEE) to Linearized Navier-Stokes Equation (LNS) for indoor and near field study.

- Investigate the possibility of implementing the Biot theory to simulate a flexible frame porous medium.

- Investigate the possibility of including nonlinear effects in lossy media.

References

1.   Norton, K.A., *The propagation of radio waves over the surface of the earth and in the upper atmosphere.* Proceedings of the Institute of Radio Engineers, 1937. **25**(9): p. 1203-1236.

2.   Ke, G. and Z.Q.C. Zheng, *Sound propagation around arrays of rigid and porous cylinders in free space and near a ground boundary.* Journal of Sound and Vibration, 2016. **370**: p. 43-53.

3.   Kafesaki, M. and E.N. Economou, *Multiple-scattering theory for three-dimensional periodic acoustic composites.* Physical Review B, 1999. **60**(17): p. 11993-12001.

4.   Huang, Z.-G. and Z.-Y. Chen, *Acoustic Waves in Two-Dimensional Phononic Crystals With Reticular Geometric Structures.* Journal of Vibration and Acoustics, 2011. **133**(3): p. 031011-031011-6.

5.   Kushwaha, M.S., et al., *Acoustic Band-Structure of Periodic Elastic Composites.* Physical Review Letters, 1993. **71**(13): p. 2022-2025.

6.   Kushwaha, M.S. and B. Djafari-Rouhani, *Giant sonic stop bands in two-dimensional periodic system of fluids.* Journal of Applied Physics, 1998. **84**(9): p. 4677-4683.

7.   Romero-García, V., L.M. Garcia-Raffi, and J.V. Sánchez-Pérez, *Evanescent waves and deaf bands in sonic crystals.* AIP Advances, 2011. **1**(4): p. 041601-041601-9.

8.   Huang, Y., C.L. Zhang, and W.Q. Chen, *Elastic Wave Band Structures and Defect States in a Periodically Corrugated Piezoelectric Plate.* Journal of Applied Mechanics, 2014. **81**(8): p. 081005-081005-6.

9.   Jensen, F.B., *Computational ocean acoustics*. 2nd ed. Modern acoustics and signal processing. 2011, New York: Springer. xviii, 794 p.

10.   DiNapoli, F.R. and R.L. Deavenport, *Numerical Models of Underwater Acoustic Propagation*, in *Ocean Acoustics*, J.A. DeSanto, Editor. 1979, Springer Berlin Heidelberg: Berlin, Heidelberg. p. 79-157.

11.   Raspet, R., et al., *A Fast-Field Program for Sound-Propagation in a Layered Atmosphere above an Impedance Ground.* Journal of the Acoustical Society of America, 1985. **77**(2): p. 345-352.

12.   Lee, S.W., et al., *Impedance Formulation of the Fast Field Program for Acoustic-Wave Propagation in the Atmosphere.* Journal of the Acoustical Society of America, 1986. **79**(3): p. 628-634.

13.   Tappert, F.D., *The parabolic approximation method*, in *Wave Propagation and Underwater Acoustics*, J.B. Keller and J.S. Papadakis, Editors. 1977, Springer Berlin Heidelberg: Berlin, Heidelberg. p. 224-287.

14.   Lee, D., A.D. Pierce, and E.C. Shang, *Parabolic equation development in the twentieth century.* Journal of Computational Acoustics, 2000. **8**(4): p. 527-637.

15.   Gilbert, K.E. and M.J. White, *Application of the Parabolic Equation to Sound-Propagation in a Refracting Atmosphere.* Journal of the Acoustical Society of America, 1989. **85**(2): p. 630-637.

16.   Krynkin, A., et al., *Acoustic insertion loss due to two dimensional periodic arrays of circular cylinders parallel to a nearby surface.* The Journal of the Acoustical Society of America, 2011. **130**(6): p. 3736-3745.

17.   Van der Aa, B. and J. Forssén, *Upward refraction of sound propagating outdoors by a graded index sonic crystal noise barrier.* Applied acoustics, 2013. **74**(1): p. 89-101.

18.   Crombie, D. and D. Hothersall, *The performance of multiple noise barriers.* Journal of sound and vibration, 1994. **176**(4): p. 459-473.

19.   Yu, X., et al., *On the sound insulation of acoustic metasurface using a sub-structuring approach.* Journal of Sound and Vibration, 2017. **401**: p. 190-203.

20.   Nouh, M., O. Aldraihem, and A. Baz, *Vibration Characteristics of Metamaterial Beams With Periodic Local Resonances.* Journal of Vibration and Acoustics, 2014. **136**(6): p. 061012-061012-12.

21.   Johnson, W.M. and K.A. Cunefare, *Structural Acoustic Optimization of a Composite Cylindrical Shell Using FEM/BEM.* Journal of Vibration and Acoustics, 2002. **124**(3): p. 410-413.

22.   Ke, G. and Z.C. Zheng, *Time-Domain Simulation of Long-Range Sound Propagation in an Atmosphere with Temperature Gradient*, in *51st AIAA Aerospace Sciences Meeting including the New Horizons Forum and Aerospace Exposition*. 2013, American Institute of Aeronautics and Astronautics.

23.   Chan, C.T., Q.L. Yu, and K.M. Ho, *Order-N spectral method for electromagnetic waves.* Physical Review B, 1995. **51**(23): p. 16635-16642.

24.   Tanaka, Y., Y. Tomoyasu, and S. Tamura, *Band structure of acoustic waves in phononic lattices: Two-dimensional composites with large acoustic mismatch.* Physical Review B, 2000. **62**(11): p. 7387-7392.

25.   Zheng, Z.C. and W. Li, *Numerical stabilities and boundary conditions in time-domain Eulerian simulations of acoustic wave propagations with and without background flow.* Applied Mathematics and Computation, 2008. **202**(1): p. 146-161.

26.   Ke, G. and Z.C. Zheng. *Time-domain simulation of long-range sound propagation in an atmosphere with temperature gradient.* in *51st AIAA Aerospace Sciences Meeting including the New Horizons Forum and Aerospace Exposition, Grapevine, Texas*. 2013.

27.   Biot, M.A., *Theory of Propagation of Elastic Waves in a Fluid-Saturated Porous Solid .1. Low-Frequency Range.* Journal of the Acoustical Society of America, 1956. **28**(2): p. 168-178.

28.   Biot, M.A., *Theory of Propagation of Elastic Waves in a Fluid-Saturated Porous Solid .2. Higher Frequency Range.* Journal of the Acoustical Society of America, 1956. **28**(2): p. 179-191.

29.   Allard, J.F. and N. Atalla, *Propagation of sound in porous media : modelling sound absorbing materials.* 2nd ed. 2009, Hoboken, N.J.: Wiley. xiv, 358 p.

30.   Bolton, J.S., N.M. Shiau, and Y.J. Kang, *SOUND TRANSMISSION THROUGH MULTI-PANEL STRUCTURES LINED WITH ELASTIC POROUS MATERIALS.* Journal of Sound and Vibration, 1996. **191**(3): p. 317-347.

31.   Rossing, T.D., *Springer handbook of acoustics*. 2nd ed. 2014, Dordrecht: Springer. xxvi, 1286 pages.

32.   Attenborough, K., *Acoustical characteristics of porous materials.* Physics Reports, 1982. **82**(3): p. 179-227.

33.   Blanc, E., G. Chiavassa, and B. Lombard, *Biot-JKD model: Simulation of 1D transient poroelastic waves with fractional derivatives.* Journal of Computational Physics, 2013. **237**: p. 1-20.

34.   Blanc, E., G. Chiavassa, and B. Lombard, *A time-domain numerical modeling of two-dimensional wave propagation in porous media with frequency-dependent dynamic permeability.* Journal of the Acoustical Society of America, 2013. **134**(6): p. 4610-4623.

35.   Deckers, E., et al., *A Wave Based Method for the efficient solution of the 2D poroelastic Biot equations.* Computer Methods in Applied Mechanics and Engineering, 2012. **201**: p. 245-262.

36.   Horlin, N.E. and P. Goransson, *Weak, anisotropic symmetric formulations of Biot's equations for vibro-acoustic modelling of porous elastic materials.* International Journal for Numerical Methods in Engineering, 2010. **84**(12): p. 1519-1540.

37.   Chekkal, I., et al., *Vibro-Acoustic Properties of Auxetic Open Cell Foam: Model and Experimental Results.* Acta Acustica United with Acustica, 2010. **96**(2): p. 266-274.

38.   Liu, H., et al., *Wave propagation in sandwich panels with a poroelastic core.* Journal of the Acoustical Society of America, 2014. **135**(5): p. 2683-2693.

39.   Delany, M.E. and E.N. Bazley, *Acoustical properties of fibrous absorbent materials.* Applied Acoustics, 1970. **3**(2): p. 105-116.

40.   Miki, Y., *Acoustical properties of porous materials-Modifications of Delany-Bazley models.* Journal of the Acoustical Society of Japan (E), 1990. **11**(1): p. 19-24.

41.   Attenborough, K., *Acoustical Impedance Models for Outdoor Ground Surfaces.* Journal of Sound and Vibration, 1985. **99**(4): p. 521-544.

42.   Attenborough, K., *Ground Parameter Information for Propagation Modeling.* Journal of the Acoustical Society of America, 1992. **92**(1): p. 418-427.

43.   Ostashev, V.E., et al., *Pade approximation in time-domain boundary conditions of porous surfaces.* Journal of the Acoustical Society of America, 2007. **122**(1): p. 107-112.

44.   Salomons, E.M., R. Blumrich, and D. Heimann, *Eulerian time-domain model for sound propagation over a finite-impedance ground surface. Comparison with frequency-domain models.* Acta Acustica United with Acustica, 2002. **88**(4): p. 483-492.

45.   Zwikker, C. and C.W. Kosten, *Sound absorbing materials.* 1949, New York,: Elsevier Pub. Co. ix, 174 p.

46.   Ke, G. and Z.C. Zheng, *Sound propagation around arrays of rigid and porous cylinders in free space and near a ground boundary.* Journal of Sound and Vibration, 2016. **370**: p. 43-53.

47.   Wilson, D.K., et al., *Time-domain calculations of sound interactions with outdoor ground surfaces.* Applied Acoustics, 2007. **68**(2): p. 173-200.

48.   Wilson, D.K., *Relaxation-Matched Modeling of Propagation through Porous-Media, Including Fractal Pore Structure.* Journal of the Acoustical Society of America, 1993. **94**(2): p. 1136-1145.

49.   Wilson, D.K., V.E. Ostashev, and S.L. Collier, *Time-domain equations for sound propagation in rigid-frame porous media (L).* Journal of the Acoustical Society of America, 2004. **116**(4): p. 1889-1892.

50.   Szabo, T.L., *Time-Domain Wave-Equations for Lossy Media Obeying a Frequency Power-Law.* Journal of the Acoustical Society of America, 1994. **96**(1): p. 491-500.

51.   Blackstock, D.T., *Generalized Burgers-Equation for Plane-Waves.* Journal of the Acoustical Society of America, 1985. **77**(6): p. 2050-2053.

52.   Chen, W. and S. Holm, *Modified Szabo's wave equation models for lossy media obeying frequency power law.* Journal of the Acoustical Society of America, 2003. **114**(5): p. 2570-2574.

53.   Liebler, M., et al., *Full wave modeling of therapeutic ultrasound: Efficient time-domain implementation of the frequency power-law attenuation.* Journal of the Acoustical Society of America, 2004. **116**(5): p. 2742-2750.

54. Kelly, J.F., R.J. McGough, and M.M. Meerschaert, *Analytical time-domain Green's functions for power-law media.* Journal of the Acoustical Society of America, 2008. **124**(5): p. 2861-2872.

55. Chen, W. and S. Holm, *Fractional Laplacian time-space models for linear and nonlinear lossy media exhibiting arbitrary frequency power-law dependency.* Journal of the Acoustical Society of America, 2004. **115**(4): p. 1424-1430.

56. Wismer, M.G., *Finite element analysis of broadband acoustic pulses through inhomogenous media with power law attenuation.* Journal of the Acoustical Society of America, 2006. **120**(6): p. 3493-3502.

57. Lighthill, M.J., *On the Energy Scattered from the Interaction of Turbulence with Sound or Shock Waves.* Proceedings of the Cambridge Philosophical Society, 1953. **49**(3): p. 531-551.

58. Kraichnan, R.H., *The Scattering of Sound in a Turbulent Medium.* Journal of the Acoustical Society of America, 1953. **25**(6): p. 1096-1104.

59. Howe, M.S., *Contributions to Theory of Aerodynamic Sound, with Application to Excess Jet Noise and Theory of Flute.* Journal of Fluid Mechanics, 1975. **71**(Oct28): p. 625-673.

60. Oshea, S., *Sound Scattering by a Potential Vortex.* Journal of Sound and Vibration, 1975. **43**(1): p. 109-116.

61. Candel, S.M., *Acoustic Transmission and Reflection by a Shear Discontinuity Separating Hot and Cold Regions.* Journal of Sound and Vibration, 1972. **24**(1): p. 87-&.

62. Ferziger, J.H., *Low-Frequency Acoustic Scattering from a Trailing Vortex.* Journal of the Acoustical Society of America, 1974. **56**(6): p. 1705-1707.

63. Colonius, T., S.K. Lele, and P. Moin, *The Scattering of Sound-Waves by a Vortex - Numerical Simulations and Analytical Solutions.* Journal of Fluid Mechanics, 1994. **260**: p. 271-298.

64. Hattori, Y. and S.G.L. Smith, *Axisymmetric acoustic scattering by vortices.* Journal of Fluid Mechanics, 2002. **473**: p. 275-294.

65. Candel, S.M., *Numerical-Solution of Wave Scattering Problems in the Parabolic Approximation.* Journal of Fluid Mechanics, 1979. **90**(Feb): p. 465-507.

66. Ford, R. and S.G.L. Smith, *Scattering of acoustic waves by a vortex.* Journal of Fluid Mechanics, 1999. **386**: p. 305-328.

67. Smith, S.G.L. and R. Ford, *Three-dimensional acoustic scattering by vortical flows. I. General theory.* Physics of Fluids, 2001. **13**(10): p. 2876-2889.

68. Cheinet, S., et al., *Unified modeling of turbulence effects on sound propagation.* Journal of the Acoustical Society of America, 2012. **132**(4): p. 2198-2209.

69. Clair, V. and G. Gabard, *Numerical assessment of the scattering of acoustic waves by turbulent structures*, in *21st AIAA/CEAS Aeroacoustics Conference*. 2015, American Institute of Aeronautics and Astronautics: Dallas,TX.

70. Clair, V. and G. Gabard, *Spectral broadening of acoustic waves by convected vortices.* Journal of Fluid Mechanics, 2018. **841**: p. 50-80.

71. Sullivan, D.M., *Frequency-dependent FDTD methods using Z transforms.* IEEE Transactions on Antennas and Propagation, 1992. **40**(10): p. 1223-1230.

72. Luebbers, R.J. and F. Hunsberger, *Fdtd for Nth-Order Dispersive Media.* Ieee Transactions on Antennas and Propagation, 1992. **40**(11): p. 1297-1301.

73. Kelley, D.F. and R.J. Luebbers, *Piecewise linear recursive convolution for dispersive media using FDTD.* IEEE Transactions on Antennas and Propagation, 1996. **44**(6): p. 792-797.

74. Abdijalilov, K. and H. Grebel, *Z-transform theory and FDTD stability.* IEEE Transactions on Antennas and Propagation, 2004. **52**(11): p. 2950-2954.

75. Joseph, R.M., S.C. Hagness, and A. Taflove, *Direct time integration of Maxwell's equations in linear dispersive media with absorption for scattering and propagation of femtosecond electromagnetic pulses.* Optics Letters, 1991. **16**(18): p. 1412-1414.

76. Morse, P.M. and K.U. Ingard, *Theoretical acoustics.* International series in pure and applied physics. 1968, New York,: McGraw-Hill. xix, 927 p.

77. Sparrow, V.W. and R. Raspet, *A Numerical-Method for General Finite-Amplitude Wave-Propagation in 2 Dimensions and Its Application to Spark Pulses.* Journal of the Acoustical Society of America, 1991. **90**(5): p. 2683-2691.

78. Norton, G.V. and J.C. Novarini, *Including dispersion and attenuation directly in the time domain for wave propagation in isotropic media.* Journal of the Acoustical Society of America, 2003. **113**(6): p. 3024-3031.

79. Treeby, B.E. and B.T. Cox, *Modeling power law absorption and dispersion for acoustic propagation using the fractional Laplacian.* Journal of the Acoustical Society of America, 2010. **127**(5): p. 2741-2748.

80. Harten, A., et al., *Uniformly High-Order Accurate Essentially Nonoscillatory Schemes .3.* Journal of Computational Physics, 1987. **71**(2): p. 231-303.

81. Shu, C.W., et al., *High-Order Eno Schemes Applied to 2-Dimensional and 3-Dimensional Compressible Flow.* Applied Numerical Mathematics, 1992. **9**(1): p. 45-71.

82. Liu, X.D., S. Osher, and T. Chan, *Weighted Essentially Nonoscillatory Schemes.* Journal of Computational Physics, 1994. **115**(1): p. 200-212.

83. Walsteijn, F.H., *Robust Numerical-Methods for 2d Turbulence.* Journal of Computational Physics, 1994. **114**(1): p. 129-145.

84. Jiang, G.S. and C.W. Shu, *Efficient implementation of weighted ENO schemes.* Journal of Computational Physics, 1996. **126**(1): p. 202-228.

85. Erlebacher, G., M.Y. Hussaini, and C.W. Shu, *Interaction of a shock with a longitudinal vortex.* Journal of Fluid Mechanics, 1997. **337**: p. 129-153.

86. Jiang, G.S. and D.P. Peng, *Weighted ENO schemes for Hamilton-Jacobi equations.* Siam Journal on Scientific Computing, 2000. **21**(6): p. 2126-2143.

87. Berthelsen, P.A. and O.M. Faltinsen, *A local directional ghost cell approach for incompressible viscous flow problems with irregular boundaries.* Journal of Computational Physics, 2008. **227**(9): p. 4354-4397.

88. Xu, Y., Z.C. Zheng, and D.K. Wilson, *Simulation of Turbulent Wind Noise Reduction by Porous Windscreens Using High-Order Schemes.* Journal of Computational Acoustics, 2010. **18**(4): p. 321-334.

89. Xu, Y., Z.C. Zheng, and D.K. Wilson, *A computational study of the effect of windscreen shape and flow resistivity on turbulent wind noise reduction.* Journal of the Acoustical Society of America, 2011. **129**(4): p. 1740-1747.

90. ANSI/ASA, *American national standard method for determining the acoustic impedance of ground surfaces.* 2010.

91. Attenborough, K., I. Bashir, and S. Taherzadeh, *Outdoor ground impedance models.* Journal of the Acoustical Society of America, 2011. **129**(5): p. 2806-2819.

92.   Hu, F.Q., *A Perfectly Matched Layer absorbing boundary condition for linearized Euler equations with a non-uniform mean flow.* Journal of Computational Physics, 2005. **208**(2): p. 469-492.

93.   Bashir, I., S. Taherzadeh, and K. Attenborough, *Diffraction assisted rough ground effect: Models and data.* Journal of the Acoustical Society of America, 2013. **133**(3): p. 1281-1292.

94.   Lagarias, J.C., et al., *Convergence properties of the Nelder-Mead simplex method in low dimensions.* Siam Journal on Optimization, 1998. **9**(1): p. 112-147.

95.   Dragna, D., P. Pineau, and P. Blanc-Benon, *A generalized recursive convolution method for time-domain propagation in porous media.* Journal of the Acoustical Society of America, 2015. **138**(2): p. 1030-1042.

96.   Alberts, W.C.K. and K.J. Sanchez, *Deduction of the acoustic impedance of the ground via a simulated three-dimensional microphone array.* Journal of the Acoustical Society of America, 2013. **134**(5): p. El471-El476.

97.   Gustavsen, B. and A. Semlyen, *Rational approximation of frequency domain responses by vector fitting.* Ieee Transactions on Power Delivery, 1999. **14**(3): p. 1052-1061.

98.   Gustavsen, B., *Improving the pole relocating properties of vector fitting.* Ieee Transactions on Power Delivery, 2006. **21**(3): p. 1587-1592.

99.   Deschrijver, D., et al., *Macromodeling of multiport systems using a fast implementation of the vector fitting method.* Ieee Microwave and Wireless Components Letters, 2008. **18**(6): p. 383-385.

100.   Johnson, D.L., J. Koplik, and R. Dashen, *Theory of Dynamic Permeability and Tortuosity in Fluid-Saturated Porous-Media.* Journal of Fluid Mechanics, 1987. **176**: p. 379-402.

101.   Turo, D. and O. Umnova, *Time Domain Modelling of Sound Propagation in Porous Media and the Role of Shape Factors.* Acta Acustica United with Acustica, 2010. **96**(2): p. 225-238.

102.   Remillieux, M.C., S.M. Pasareanu, and U.P. Svensson, *Numerical modeling of the exterior-to-interior transmission of impulsive sound through three-dimensional, thin-walled elastic structures.* Journal of Sound and Vibration, 2013. **332**(25): p. 6725-6742.

103.   Arjunan, A., et al., *Finite element acoustic analysis of a steel stud based double-leaf wall.* Building and Environment, 2013. **67**: p. 202-210.

104.   Arjunan, A., et al., *Development of a 3D finite element acoustic model to predict the sound reduction index of stud based double-leaf walls.* Journal of Sound and Vibration, 2014. **333**(23): p. 6140-6155.

105.   Lovholt, F., et al., *Simulating low frequency sound transmission through walls and windows by a two-way coupled fluid structure interaction model.* Journal of Sound and Vibration, 2017. **396**: p. 203-216.

106.   Arjunan, A., et al., *A Computationally-Efficient Numerical Model to Characterize the Noise Behavior of Metal-Framed Walls.* Metals, 2015. **5**(3): p. 1414-1431.

107.   Pellicier, A. and N. Trompette, *A review of analytical methods, based on the wave approach, to compute partitions transmission loss.* Applied Acoustics, 2007. **68**(10): p. 1192-1212.

108.   Sgard, F.C., N. Atalla, and C.K. Amedin, *Vibro-acoustic behavior of a cavity backed by a plate coated with a meso-heterogeneous porous material.* Acta Acustica United with Acustica, 2007. **93**(1): p. 106-114.

109. Chazot, J.D. and J.L. Guyader, *Transmission loss of double panels filled with porogranular materials.* Journal of the Acoustical Society of America, 2009. **126**(6): p. 3040-3048.

110. Thomas, A., et al., *Aircraft Sound Transmission in Homes Categorized by Typical Construction Type.*

111. Duryea, A.P., et al., *Acoustic Bubble Removal to Enhance SWL Efficacy at High Shock Rate: An In Vitro Study.* Journal of Endourology, 2014. **28**(1): p. 90-95.

112. Maxwell, A.D., et al., *Fragmentation of Urinary Calculi In Vitro by Burst Wave Lithotripsy.* Journal of Urology, 2015. **193**(1): p. 338-344.

113. Hill, C.R. and G.R. ter Haar, *High intensity focused ultrasound—potential for cancer treatment.* British Journal of Radiology, 1995. **68**(816): p. 1296-1303.

114. Konofagou, E.E., *Optimization of the Ultrasound-Induced Blood-Brain Barrier Opening.* Theranostics, 2012. **2**(12): p. 1223-1237.

115. Wu, S.Y., et al., *Effects of the microbubble shell physicochemical properties on ultrasound-mediated drug delivery to the brain.* Journal of Controlled Release, 2015. **212**: p. 30-40.

116. Ke, G. and Z.C. Zheng, *Simulation of sound propagation over porous barriers of arbitrary shapes.* Journal of the Acoustical Society of America, 2015. **137**(1): p. 303-309.

117. Liu, F., et al., *A semi-alternating direction method for a 2-D fractional FitzHugh–Nagumo monodomain model on an approximate irregular domain.* Journal of Computational Physics, 2015. **293**: p. 252-263.

118. Yang, Q., F. Liu, and I. Turner, *Numerical methods for fractional partial differential equations with Riesz space fractional derivatives.* Applied Mathematical Modelling, 2010. **34**(1): p. 200-218.

119. Qin, S.L., et al., *Modelling anomalous diffusion using fractional Bloch-Torrey equations on approximate irregular domains.* Computers & Mathematics with Applications, 2018. **75**(1): p. 7-21.

120. Hu, F.Q., *On absorbing boundary conditions for linearized Euler equations by a perfectly matched layer.* Journal of Computational Physics, 1996. **129**(1): p. 201-219.

121. Zhang, J., G. Ke, and Z.C. Zheng, *Time-Domain Simulation of Ultrasound Propagation With Fractional Laplacian.* 2016(50671): p. V013T01A005.

122. Berenger, J.P., *A Perfectly Matched Layer for the Absorption of Electromagnetic-Waves.* Journal of Computational Physics, 1994. **114**(2): p. 185-200.

123. Tanaka, K. and S. Ishii, *Scattering of a Plane Sound-Wave by a Vortex Pair.* Journal of the Physical Society of Japan, 1982. **51**(6): p. 1992-1999.

124. Celik, C. and M. Duman, *Crank-Nicolson method for the fractional diffusion equation with the Riesz fractional derivative.* Journal of Computational Physics, 2012. **231**(4): p. 1743-1750.

Appendix

Numerical scheme Order of accuracy validation for Lossy media simulation

While a second-order accurate scheme is used in the simulation for both time and space

[25], the approximation of boundary treatments used in the FCD and IB methods can possibly

introduce additional errors in spatial discretization. Therefore, it is necessary to re-evaluate the

order of spatial accuracy after implementation of the IB and FCD.

Three cases are tested, with the water only simulation as a baseline. The lossy-medium

only simulation is conducted to investigate the accuracy of the FCD method. Then, the

simulation with the ring-shaped lossy medium is used to investigate the accuracy of the

implementation of the IB method combining with the FCD method. Four levels of grid sizes are

used in each simulation case, namely, coarse, medium, fine and finest. The grid size h of each

level is 5×10^{-5}m, 2.5×10^{-5}m, 1.25×10^{-5}m, and 0.625×10^{-5}m, respectively. A very

small time-step, $\Delta t = 1.25 \times 10^{-9}$s, is used to ensure the stability of the simulation. The

simulation results at the moment of $t = 7.5$μs, which is when the wave front fully passes the

center of the domain, are used. All the nodal point pressure values along the centerline $z =$

0.015m are used to calculate the L_2-norm of the acoustic pressure. The L_2-norm error is

calculated as:

$$L_2 = \sqrt{\frac{\sum_{i=1}^{IMAX}\left(p_i - p_{ref_i}\right)^2}{IMAX}} \tag{A1}$$

Since the exact solution is not available, the finest grid solution at $h = 0.625 \times 10^{-5}$m is used

as the reference.

Table 3 gives the L_2-norm errors of the different grid resolutions in the three cases. The

observed order is computed using $P = \log(L_{2h}/L_{2_{0.5h}})/\log 2$. The L_2-norm curve of each case is

also given in Figure 59. It can be found that the slope of the L_2-norm curve of the water-only case is over 2. For the lossy-medium only case, even the FCD is a second-order method [117, 119, 124], the order of the scheme is below 2. For the case with the ring-shaped lossy material, the order of the simulation accuracy is back to above 2, but slightly lower than the water-only case.

Table 3 L_2-norm pressure errors and observed orders of accuracy for water-only, lossy medium only and ring-shaped lossy medium cases

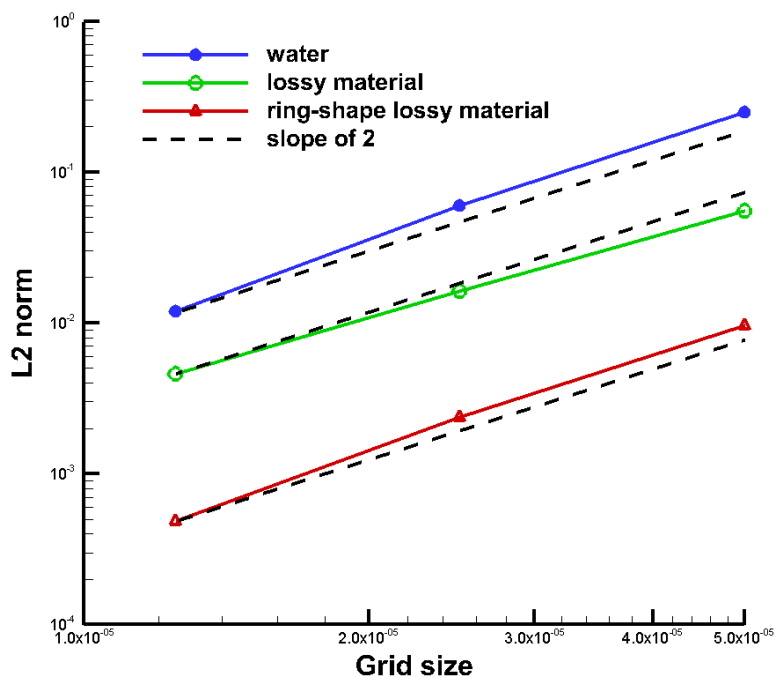| Simulation material	L_2-norm at grid size (m) 5×10^{-5}	L_2-norm at grid size (m) 2.5×10^{-5}	L_2-norm at grid size (m) 1.25×10^{-5}	L_2-norm at grid size (m) 0.625×10^{-5}	Observed order (P)
Water only	2.4760E-01	5.9700E-02	1.1900E-02		2.19
lossy medium only (y=1.9)	5.5500E-02	1.6300E-02	4.6000E-03		1.79
ring-shaped lossy medium	9.5852E-03	2.3772E-03	4.8398E-04		2.15

Figure 59. The L_2-norms of the three cases verse the grid size in comparison with a line of slope 2 (dash)